INVESTIGATION OF PHYSICAL PROCESSES IN DIGITAL X-RAY TOMOSYNTHESIS IMAGING OF THE BREAST

A Thesis
Presented to
The Academic Faculty

By

Ioannis Sechopoulos

In Partial Fulfillment
Of the Requirements for the Degree
Doctor of Philosophy in Bioengineering

Georgia Institute of Technology
May 2007

INVESTIGATION OF PHYSICAL PROCESSES IN DIGITAL X-RAY TOMOSYNTHESIS IMAGING OF THE BREAST

Approved by:

Dr. Andrew Karellas, Advisor
Department of Radiology
Emory University
Department of Biomedical Engineering
Georgia Institute of Technology

Dr. John N. Oshinski
Department of Radiology
Emory University
Department of Biomedical Engineering
Georgia Institute of Technology

Dr. Xiaoping P. Hu
Department of Biomedical Engineering
Georgia Institute of Technology
Emory University

Dr. Carl J. D'Orsi
Department of Radiology
Emory University

Dr. Ernest V. Garcia
Department of Radiology
Emory University
Department of Biomedical Engineering
Georgia Institute of Technology

Date Approved: March 14th, 2007

To the loving memory of my father

ACKNOWLEDGEMENTS

I owe a great level of gratitude to many people who are responsible for my arriving to this stage in my life. I would like to begin by expressing my appreciation to Dr. Andrew Karellas who has supported me again and again, always looking out for my well-being, and whose confidence in my abilities have inspired me to push myself more than I thought possible. His incredible talent as a scientist, as well as his never-ending guidance, encouragement and generosity are an inspiration for what I want to accomplish in my career and in my life. Thank you for everything.

I would also like to thank Dr. Carl D'Orsi for his constant support for my work, his ever-present willingness to be of assistance, and his belief in me. His vast knowledge is only overshadowed by his kindness and his vision. I am very thankful to Dr. Ernest Garcia, Dr. Xiaoping Hu, and Dr. John Oshinski for their advice, cooperation, and flexibility. Their assistance ever since I entered Georgia Tech has been invaluable.

I also wish to thank my friend Dr. Sankar Suryanarayanan, who made me feel welcome from the first day we met. I thank him for his support during the last three years not only in my research but also outside of the lab. I also thank Dr. Srinivasan Vedantham for his help and advice in my research efforts. I owe special thanks to Ms. Linda Burr who always made sure I had what I needed to conduct my research and took care of the administrative work, and to Mr. Chris Ruffin, an invaluable resource at Georgia Tech.

I would like to thank the members of the Geant4 collaboration, and especially Mr. Joseph Perl and Dr. Makoto Asai for creating a very powerful research tool and for being extremely cooperative with me during the course of this work. I also wish to recognize the cooperation of Mr. Steve Pittard and Mr. Keven Haynes of the Emory High

Performance Compute Cluster, whose help with the cluster made this process a lot smoother.

I would like to thank my brother and sister and their families for their love and encouragement, and my wife's family for their ever-present support and kindness. There are no words to express my gratitude and admiration for my parents, whose wisdom, strength and sacrifice have made me the person I am today. All my successes are thanks to their love and guidance.

Finally, I want to thank my wife, Carina. Because of her love, support, encouragement, understanding and friendship my life has changed forever. The possibility of sharing every moment of my life with her is the greatest gift I have ever received.

This study was supported in part by the National Institutes of Health (NIH) grants RO1-EB002123 and RO1-EB004015 from the National Institute of Biomedical Imaging and Bioengineering (NIBIB), respectively. Portions of this work were also supported by an infrastructure grant from the Georgia Cancer Coalition (GCC). The contents are solely the responsibility of the author and do not necessarily represent the official views of the NIBIB, NIH or GCC.

TABLE OF CONTENTS

LIST OF TABLES

LIST OF FIGURES

LIST OF ABBREVIATIONS

α	Tomosynthesis projection angle from detector surface
a_{pix}	Pixel pitch
AVW	Artifact vertical width
β	Tomosynthesis projection angle from center of rotation
BS	Bone surface
CC	Cranio-caudal
CND	Chest wall to nipple distance
CNR	Contrast-to-noise ratio
COM	Center of mass
COR	Center of rotation
COV	Coefficient of variation
CT	Computed tomography
DBCT	Dedicated breast computed tomography
DCOR	Distance from the center of rotation
DFM	Deviation from the mean
D_g	Glandular dose
D_gN	Normalized glandular dose
D_gN_0	Normalized glandular dose for 0 degree projection
DQE	Detective quantum efficiency
DU	Digital unit
E(x,y)	Projection from estimated volume
ε_{g_2}	Poisson excess
f_{pix}	Fill factor

FWHM	Full-width at half-maximum
G	Glandular fraction
$\bar{g}_1$	Quantum efficiency of scintillator
$\bar{g}_2$	Quantum gain of scintillator
$\bar{g}_4$	Quantum efficiency of detector
h	Distance from source to COR
HBA	Homogeneous bone approximation
HVL	Half-value layer
I(x,y)	DU Image
ICRP	International Commission on Radiological Protection
ICRU	International Commission on Radiation Units and Measurements
IID	Iso-center to imager distance
III(u,v)	NPS aliasing
kVp	Peak kilovoltage
l	Distance from detector to COR
l_{vp}	Length travelled in voxel v by ray that reaches pixel p
MEAC	Mass-energy absorption coefficient
μ_{RGD}	Mean RGD
μ_B	Mean background
μ_S	Mean signal
μ_V	Linear attenuation coefficient of voxel v
MLEM	Maximum likelihood expectation maximization
MLO	Medio-lateral oblique
MTF	Modulation transfer function
N	Number of x-rays exiting from breast

N_0	Number of x-rays incident on breast
N_α	Number of projections in set
NIST	National Institute of Standards and Technology
NPS	Noise power spectrum
ORNL	Oak Ridge National Laboratory
PMMA	Polymethyl-methacrylate
PSF	Point spread function
q_0	Mean fluence exiting the breast
QE	Quantum efficiency
QF	Quality factor
R_α	Ray trace for projection angle alpha
R'_α	Equivalent ray trace for projection angle alpha
RBM	Red bone marrow
RGD	Relative glandular dose
RNG	Random number generator
ROD	Relative organ dose
ROI	Region of interest
S_{add}	Additive electronic noise
SID	Source-to-imager distance
σ_B	Standard deviation of background
SPR	Scatter-to-primary ratio
T	Compressed breast thickness
T_3	Scintillator MTF
T_{3o}	Obliqueness MTF
T_5	Detector MTF

t_f	Transmission factor of support and cover plates
X(x,y)	Exposure Image
X_{CR}	Exposure at central ray on support plate
Y_p	Acquired projection

SUMMARY

Early detection is one of the most important factors in the survival of patients diagnosed with breast cancer. For this reason the development of improved screening mammography methods is one of primary importance. One problem that is present in standard planar mammography, which is not solved with the introduction of digital mammography, is the possible masking of lesions by normal breast tissue because of the inherent collapse of three-dimensional anatomy into a two-dimensional image. Digital tomosynthesis imaging has the potential to avoid this effect by incorporating into the acquired image information on the vertical position of the features present in the breast. Previous studies have shown that at an approximately equivalent dose, the contrast-detail trends of several tomosynthesis methods are better than those of planar mammography. By optimizing the image acquisition parameters and the tomosynthesis reconstruction algorithm, it is believed that a tomosynthesis imaging system can be developed that provides more information on the presence of lesions while maintaining or reducing the dose to the patient.

Before this imaging methodology can be translated to routine clinical use, a series of issues and concerns related to tomosynthesis imaging must be addressed. This work investigates the relevant physical processes to improve our understanding and enable the introduction of this tomographic imaging method to the realm of clinical breast imaging. The processes investigated in this work included the dosimetry involved in tomosynthesis imaging, x-ray scatter in the projection images, imaging system performance, and acquisition geometry.

A comprehensive understanding of the glandular dose to the breast during tomosynthesis imaging, as well as the dose distribution to most of the radiosensitive

tissues in the body from planar mammography, tomosynthesis and dedicated breast computed tomography was gained. The analysis of the behavior of x-ray scatter in tomosynthesis yielded an in-depth characterization of the variation of this effect in the projection images. Finally, the theoretical modeling of a tomosynthesis imaging system, combined with the other results of this work was used to find the geometrical parameters that maximize the quality of the tomosynthesis reconstruction.

CHAPTER 1

INTRODUCTION

Background

Breast cancer is today the most diagnosed type of cancer in women, excluding skin cancer. In 2007, in the United States alone, over 178,000 new cases of breast cancer will be diagnosed, and over 40,000 women will die from this disease, making it the second leading cause of death from cancer among women (American Cancer Society 2007). The introduction of screening mammography has been responsible for up to a 40% reduction in breast cancer mortality (Humphrey et al 2002). However, standard (planar) mammography is not without limitations. The sensitivity of first mammography previously reported ranges from 71% to 96%, but it may be significantly less in dense breasts (Kerlikowske et al 1996; Rosenberg et al 1996; Kolb et al 1998; Rosenberg et al 1998; Humphrey et al 2002; Kolb et al 2002). In addition, the specificity of a single mammographic examination has been reported to be approximately 80% to 85%, but, over a ten year period, approximately one quarter of the women that undergo screening mammography will have at least one false positive examination (Elmore et al 1998). Major factors for these false positives include breast density and superposition of normal glandular tissue (Tabar et al 1995; Rosenberg et al 1996); the latter alone may be responsible for about 25% of all mammography recalls (Kopans 2002). The introduction of digital acquisition has helped improve breast imaging by doing away with screen-film's limited dynamic range and narrow range of linear response among other issues. However, digital mammography is still limited in that it acquires a two dimensional projection of a three dimensional object, collapsing all the volumetric information onto one plane. To overcome this limitation, extensive research is in progress to introduce

new imaging techniques which present at least some depth information to the radiologist. Tomosynthesis (Kolitsi et al 1992; Niklason et al 1997; Dobbins et al 2003) and dedicated breast computed tomography (Boone et al 2001; Chen et al 2002; Ning et al 2002; Gong et al 2006) are being investigated as alternatives to planar mammography that solve the issue of tissue superposition.

Digital Tomosynthesis Imaging of the Breast

Digital tomosynthesis is a technique that enables tomographic imaging by acquiring a limited number of projections from a narrow angular range, and combining these projections to reconstruct a quasi-three dimensional image. To accomplish this, the x-ray tube is rotated around the static compressed breast and a series of images are acquired, one at each x-ray tube position (Figure 1.1). During the projection acquisitions, the detector can either be static, or rotate to maintain its top surface normal to the x-ray tube (Ren et al 2005; Eberhard et al 2006). The series of images acquired, denoted the tomosynthesis projection set, is then inputted into a tomosynthesis reconstruction program which uses the different location in the projections of the same tissues to compute their vertical position, thereby reconstructing the three dimensional volume.

Digital tomosynthesis of the breast was demonstrated by Niklason et al (Niklason et al 1997) in 1997, and since then several studies have been published on the subject. Suryanarayanan et al (Suryanarayanan et al 2000; Suryanarayanan et al 2001) compared several tomosynthesis reconstruction methods to planar mammography and found significantly better threshold contrast-detail characteristics in tomosynthesis phantom images. Wu et al and Joseph et al implemented several different reconstruction methods (Wu et al 2004a; Joseph et al 2006) and compared their performance. All these

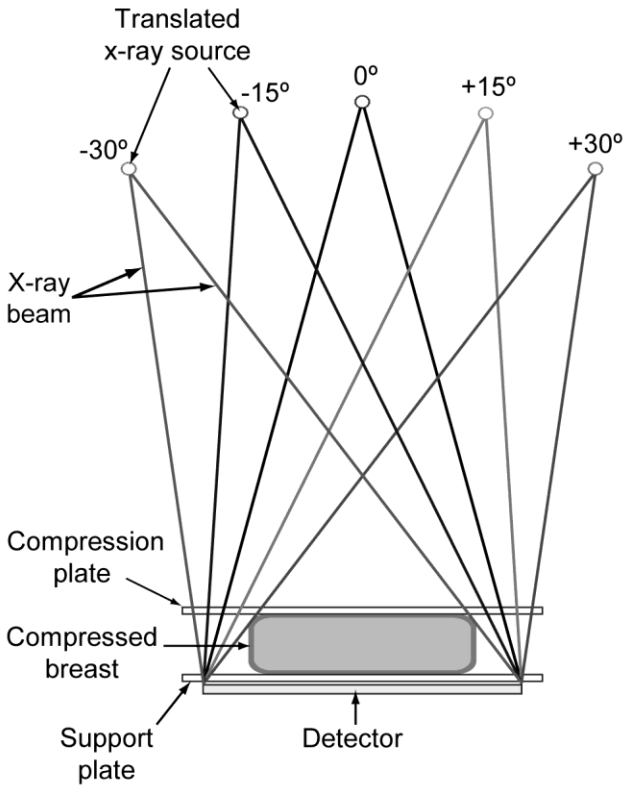

Figure 1.1 Diagram of a tomosynthesis acquisition depicting the moving x-ray source and the stationary detector.

studies report that digital tomosynthesis has the ability to suppress the masking effect of superimposed structures.

Motivation and Organization

Given the promising results found in the previous studies that focused on the development of tomosynthesis, which point to the feasibility of clinical use of tomosynthesis of the breast, it has become imperative to investigate a series of issues that need to be addressed to introduce tomosynthesis imaging of the breast into routine clinical practice. These issues include dosimetry, physical processes that affect image quality, and image acquisition optimization, among others. It is the intent of this work to address these issues, and therefore accelerate the establishment of this new

tomographic breast imaging method as one more tool for the early detection of breast cancer.

Dosimetry is the foremost concern in all radiographic imaging applications. A successful radiographic acquisition method can not involve the exposure of a high or an unknown amount of radiation dose to any tissue or body part of the patient. This is especially true if the application is to be used for the screening of asymptomatic patients, as is the goal of tomosynthesis imaging of the breast. Therefore, a comprehensive characterization of the dose involved in tomosynthesis imaging is required. This characterization involves the study of the radiation dose to the imaged breast, as well as that to the rest of the body tissues due to scattered x-rays. In radiographic breast imaging, the concern is the effect of radiation dose in the glandular tissue, where breast cancer normally develops (Wu et al 1991). Therefore, the metric used is the glandular dose, a measure of the dose deposited in the glandular tissue portion of the breast during image acquisition. In Chapter 2 the glandular dose to the imaged breast during a tomosynthesis imaging study is characterized, including its variation with a wide range of different breast sizes, compositions and x-ray spectra. This study provides the data necessary to set the limiting factors to consider when designing new tomosynthesis imaging protocols. In Chapter 3 the radiation dose to the tissues of the rest of the body from planar mammography and tomosynthesis of the breast is studied. Although dosimetry in planar mammography has been extensively investigated, the resulting dose to the other tissues has been the result of only one limited previously published study (Hatziioannou et al 2000). The whole body dosimetry study published here includes most of the radiosensitive organs and tissues of the body, and also investigates the dose to the fetus from planar mammography and tomosynthesis imaging, an important concern that has not been addressed before. To compare the whole body dosimetry resultant from tomosynthesis imaging with that of the other tomographic breast imaging

method currently being investigated, dedicated breast computed tomography (DBCT), the same analysis was performed for the latter. This study is of particular interest due to the need in DBCT of using higher energy x-ray spectra compared to that used in planar mammography and tomosynthesis. The effect of using these higher energy spectra on the whole body dose for DBCT imaging is investigated in Chapter 4.

Given the imaging limitations imposed by dosimetry, emphasis must be placed on the maximization of image quality within those limits. For this, a clear understanding of the effect that different relevant parameters have on image quality must first be understood, and then these parameters must be adjusted to obtain the images that result in the highest possible detection and characterization of lesions. Three different parameters that affect image quality are investigated in this work; the inclusion of x-ray scatter in the projection images, detector response, and acquisition geometry.

Scattered x-rays introduce a low frequency signal in the projection images that does not contribute to the image information and lowers the image contrast and resolution. The inclusion of this signal in tomographic imaging, where the acquired images are used for reconstruction, results in a further penalty in the form of reconstruction artifacts. To avoid this, the x-ray scatter phenomenon must be either reduced in the projection images or taken into account in the reconstruction model. For these approaches to be successful, a comprehensive characterization of the x-ray scatter included in the tomosynthesis projections is required. This characterization is performed in Chapter 5, where the scatter point spread functions and scatter-to-primary ratio maps resultant from different acquisition conditions are computed and analyzed. This information is later used both for the simulation of realistic tomosynthesis acquisitions and for inclusion in the implementation of an iterative reconstruction method. In addition, these results could be used for the development of pre-reconstruction processing of the projection images.

Due to the need to limit the glandular dose to the imaged breast from a tomosynthesis acquisition to levels similar to those used in planar mammography, the exposure available per projection is reduced substantially. This reduction in exposure may force a current clinical mammographic system to function in suboptimal conditions during tomosynthesis acquisitions. This could lead to the loss of image quality due to effects introduced by limitations of the imaging system, such as dominance of the additive electronic noise on the noise characteristics of the images. This possible behavior is analyzed in Chapter 6, where the imaging system's response to different acquisition conditions is characterized. This is achieved using a mathematical model that describes the signal and noise transfer characteristics of each stage in the imaging chain involved in the acquisition of a projection. This data is also used later in the simulation of tomosynthesis projection images, which, to be of value, must include the limitations imposed on real images by the imaging system.

The optimization of the acquisition geometry in tomosynthesis imaging is of utmost importance to maximize both the vertical resolution and the in-plane image quality. Due to the severe incompleteness of the tomographic information in tomosynthesis, the vertical resolution and suppression of reconstruction artifacts is highly dependent on the use of an appropriate acquisition geometry. To achieve this optimization, a balance must be found between angular range, number of projections, and available exposure per projection. To gain insight into this balance, in Chapter 7 a study is described in which the simulation of a realistic tomosynthesis imaging system was implemented and used to compare the image quality of reconstructions performed from projection sets obtained using different acquisition geometries. This involved the use of all the previous results reported in this work and the implementation of an iterative reconstruction algorithm that takes into account the presence of x-ray scatter in the projection images.

Approach

The present work is based on the design, implementation, and use of a series of advanced computational frameworks to perform comprehensive simulations of radiographic breast imaging. These simulations, based on well established theoretical tools, were used to recreate the conditions present during either planar mammographic imaging, tomosynthesis imaging of the breast, or dedicated breast computed tomography depending on the study being performed.

The computational tools developed based on the theory of Monte Carlo simulation (Hammersley et al 1964), were implemented using the Geant4 toolkit (Agostinelli et al 2003; Allison et al 2006). Geant4 is a set of C++ libraries which provide the functionality necessary to perform Monte Carlo based simulations of particle travel through matter. It is developed, supported and maintained by the Geant4 collaboration, a world-wide group of scientists and software engineers from various institutions. A brief description of the algorithm and the implementation of the Monte Carlo programs developed in this work can be found in Appendix A.

The modeling of the performance of the imaging system was based on a linear systems framework that is used to quantitatively derive the signal and noise transfer characteristics at each stage in the imaging chain (Metz et al 1979; Barrett et al 1981; Rabbani et al 1987; Rabbani et al 1989; Cunningham et al 1994; Cunningham 1998; Cunningham 2000; Cunningham et al 2001). This model results in the characterization of the performance of an imaging system using universally established metrics such as the modulation transfer function, noise power spectrum and detective quantum efficiency.

The remaining areas of the simulation of the tomosynthesis imaging system were modeled based on various theories, established practices and derived models, many of which are previous results of this same work.

CHAPTER 2

BREAST GLANDULAR DOSE IN TOMOSYNTHESIS IMAGING

Introduction

Glandular radiation dose to the imaged breast is the limiting factor when designing a new protocol in any x-ray based breast imaging application. The direct relation between x-ray exposure and image quality creates the necessity to fully understand the effect of the former on glandular dose to be able to design protocols which will yield enough information for the creation of a useful image while not exposing the patient to unnecessary radiation.

Current knowledge on radiation dose to the breast from digital tomosynthesis is limited, and any dose estimate must be made by using data computed for planar mammography. Although the radiation dose in planar mammography has been studied extensively (Dance 1990; Wu et al 1991; Wu et al 1994; Boone 1999; 2002), these studies characterize the breast as seen in a cranio-caudal (CC) view. Therefore, there is a need to evaluate the radiation dose to the breast glandular tissue during digital breast tomosynthesis examinations. For this, projection acquisitions centered about the medio-lateral oblique (MLO) view need to be considered (Wu et al 2004b), and the variation of glandular dose with projection angle must be characterized. This study's aim is to perform a comprehensive characterization of glandular dose to the breast tissue during a tomosynthesis study, taking into account the possible variations in breast size, composition, x-ray spectrum and mammographic view.

Methods

A C++ program, based on the Geant4 toolkit (Agostinelli et al 2003; Allison et al 2006) was developed to model image acquisition during a digital tomosynthesis exam of the breast. In the simulations, one million mono-energetic x-rays were emitted from the simulated x-ray point source towards the detector, and the energy deposited by any photon interaction that took place in the breast tissue was recorded and used to calculate the mono-energetic normalized glandular dose ($D_gN(E)$) as described by Boone (Boone 1999) with the suggestions by Wilkinson and Heggie (Wilkinson et al 2001). This was repeated for all the different possible combinations of the values used for breast size, thickness and glandular fraction. For each combination the energy was varied from 5.5 to 35.5 keV in 1 keV steps, and the tomosynthesis projection angle was varied from 0° to ±30° in 3° steps (due to the geometrical symmetry, only the positive angles were used in the CC view simulations). Three degree steps were used because it was deemed that this gave sufficient data to perform an adequate interpolation for other angles. This resulted in a total of 173,600 runs each of one million photons. The simulations were performed on a 64 node computer cluster, each node containing two AMD Opteron 2.2 GHz processors (Advanced Micro Devices, Inc., Sunnyvale, CA). The $D_gN(E)$ results for each geometry and angle with 1 keV resolution were computer-fit using commercially available software (TableCurve 2D, Systat Software Inc., Richmond, California) to obtain 0.5 keV resolution. The mono-energetic $D_gN(E)$ results were combined with different simulated spectra (Boone et al 1997) relevant to mammographic applications as described by Thacker (Thacker et al 2004) to obtain spectral D_gN coefficients. For this study the spectra used are listed in Table 2.1, along with their first half-value layers (HVL), specified in mm of Al, as would be measured experimentally (under the breast compression plate), and as used for the computations (before the

Table 2.1 X-ray spectra used in this study and their first half-value layer values.

Target	Filter	Tube Potential (kVp)	HVL above Compression Plate (mm Al)	HVL under Compression Plate (mm Al)
Mo	Mo	25	0.284	0.322
Mo	Mo	26	0.297	0.335
Mo	Mo	27	0.309	0.347
Mo	Rh	27	0.364	0.400
Mo	Rh	29	0.387	0.422
Rh	Rh	29	0.380	0.426
Rh	Rh	31	0.408	0.457
Rh	Rh	33	0.435	0.484
Rh	Rh	35	0.459	0.509

breast compression plate). This difference arises from the fact that the breast compression plate was included in the Monte Carlo simulations.

The acquisition system model included the full-field detector, detector cover, breast support plate, and breast compression plate. The compression plate was modeled as polycarbonate with a thickness of 2 mm, while the combination of the breast support plate and cover plate was equivalent to 3.3 mm of carbon fiber. The x-ray source was modeled as a point source located at the chest wall side edge of the detector, with its center of rotation (COR) located 4 cm above the detector surface. The source's distance from the COR was 62 cm. This results in a source-to-imager distance (SID) of 66 cm at a tomosynthesis angle of 0°. An air gap of 1.5 cm between the detector cover and the breast support plate was included. The tomosynthesis angle α was defined as measured at the detector surface, not at the COR. Given the tomosynthesis angle measured at the detector surface (α), the tomosynthesis angle measured from the COR (β) can be computed from:

$$\beta = \alpha + \arcsin\left(\frac{l \sin\alpha}{h}\right) \tag{2.1}$$

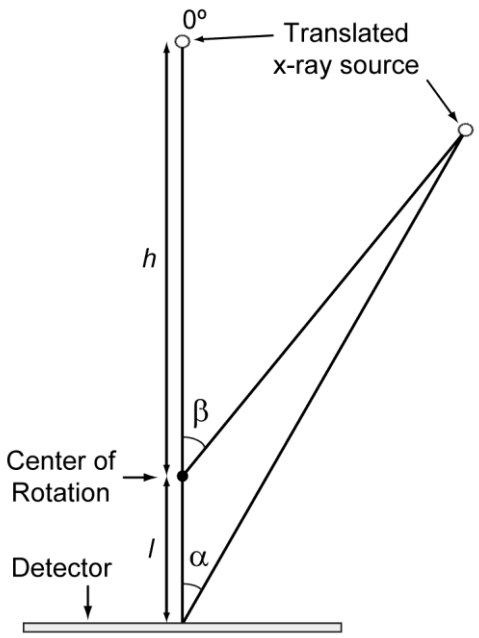

Figure 2.1 Diagram specifying the measurement location of the two projection angles related by Equation (2.1).

Where *l* is the distance from the detector surface to the COR (4 cm in this study), and *h* is the distance from the COR to the x-ray source (62 cm) (Figure 2.1).

The x-ray field from the source was collimated so that it was exactly congruent with the detector's active area. This involved modeling the collimation as variable with projection angle to maintain the x-ray field within the limits of the detector area at all angles. This variable collimation is necessary due to the fact that the detector remains stationary while the x-ray source rotates. The heel effect was included in the simulation, so the x-ray intensity was highest at the central ray, dropping to lower intensities away from it. To determine the correct x-ray intensity drop-off due to the heel effect and the inverse square distance relationship, the variation in exposure at different locations above the detector surface of a clinical digital mammography system (GE Senographe 2000D, GE Healthcare, Waukesha, WI) was measured using a calibrated dosimeter with a mammography ionization chamber (Radcal Corp., Monrovia, CA). Measurements were

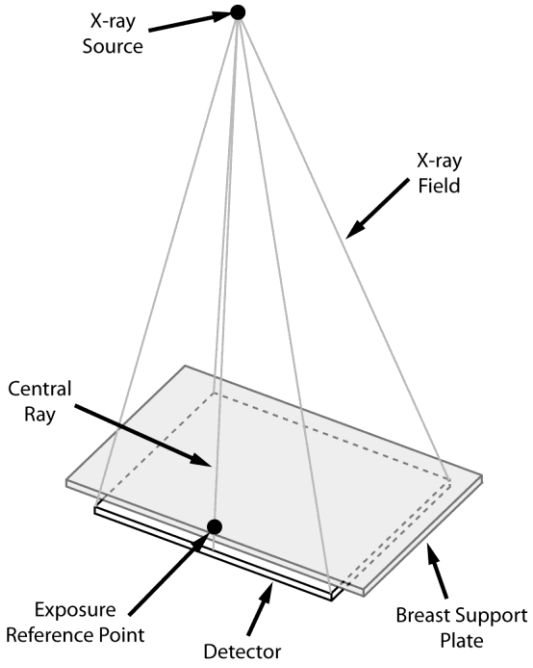

Figure 2.2 Diagram specifying the location to which the unit exposure in the normalized glandular dose values are referenced.

performed at 26 kVp and 30 kVp, and the results were imported into the Monte Carlo simulation.

In this study, the D_gN for the zero degree projection angle, D_gN_0, only is reported. For the non-zero projection angles, the value reported is the relative glandular dose coefficient ($RGD(\alpha)$), which describes the ratio of the glandular dose for that projection to the glandular dose for the zero degree projection while maintaining the kVp and mAs setting constant. The D_gN_0 is reported in units of dose to the breast per unit exposure at a specific point, in milliGray per Roentgen. This specific point is where the central ray meets the breast support plate, and the exposure is measured when no breast is present (Figure 2.2). This exposure reference point allows the clinician or medical physicist to have a pre-measured table of exposures at the reference point for the different imaging techniques (in terms of target and filter material and kVp setting) independently of the breast imaged. Although D_gN is typically reported as dose per unit entrance skin

exposure, for this study a different exposure reference point was introduced due to the inclusion of the heel effect and inverse square distance relationship in the simulation and the complexity of the breast shape in the MLO view, which make the entrance skin exposure difficult to measure. In contrast, the exposure at the intersection of the central ray and the breast support plate is easily measured and it is constant for the same x-ray beam quality (kVp and HVL) and mAs settings. The use of *RGD*(*α*) was chosen due to the difficulty of locating consistently on the detector surface the point of equal exposure while the x-ray tube is rotating.

For the reported data, the total glandular dose for a tomosynthesis study is given by:

$$D_g = X_{CR} \times D_g N_0 \times \sum_{\alpha=\alpha_{MIN}}^{\alpha_{MAX}} RGD(\alpha) = X_{CR} \times D_g N_0 \times N_\alpha \times \mu_{RGD} \qquad (2.2)$$

Where D_g is the total glandular dose, in mGy; X_{CR} is the exposure measured at the reference point with the x-ray tube at the zero degree projection position (Figure 2.2) for the kVp and mAs setting used in the study, in R; D_gN_0 is the normalized glandular dose for the zero degree projection (reported here), in mGy per R; *RGD(α)* is the relative glandular dose coefficient (reported here), which is unitless; N_α is the number of projections in the study; and μ_{RGD} is the mean *RGD* over all angles. The summation is performed over all the angles used in the tomosynthesis study (including the 0° angle, which by definition has a *RGD* of 1).

Simulation Geometry Details

Although it is possible that only projections centered about the MLO view will be used if tomosynthesis of the breast is performed routinely (Wu et al 2004b), the CC view was also studied.

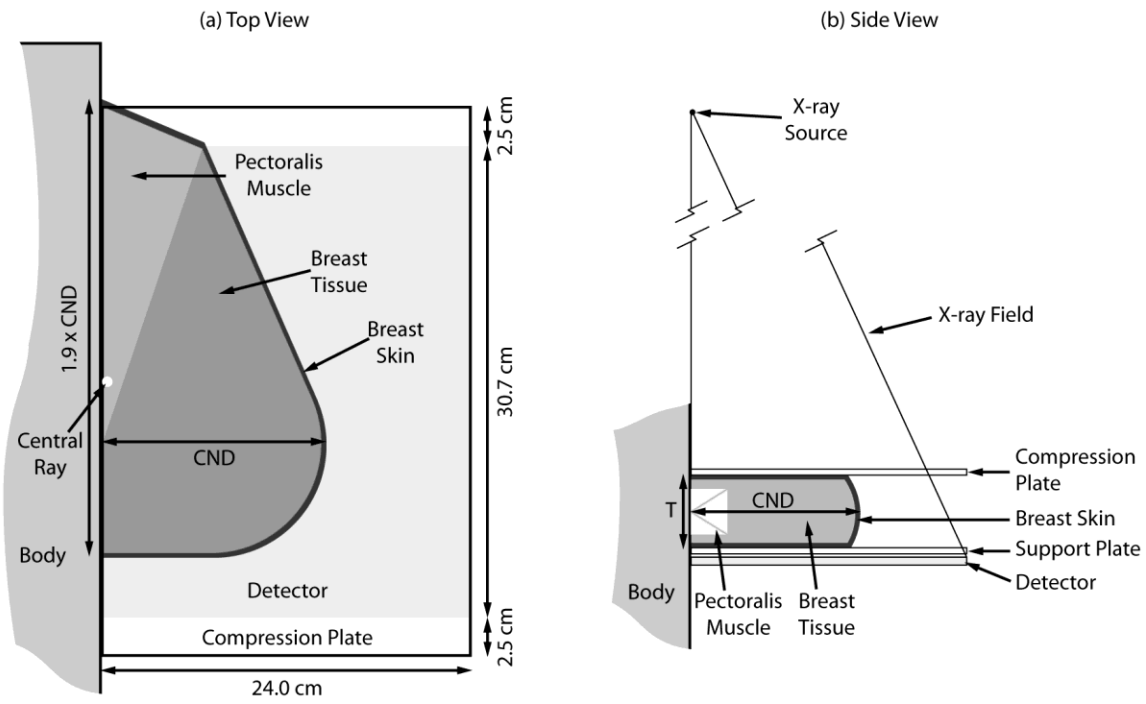

Figure 2.3 Diagram of the simulated MLO view. (a) Top view, (b) Side view. The pectoralis muscle's thickness decreases towards the caudal side.

The breast in MLO view was simulated as a complex solid which included a portion of the pectoralis muscle (Figure 2.3), since it is normally present in a clinical MLO view image. The superior portion of the pectoralis muscle and the breast tissue that is included in the image is located towards the top edge of the image for all breast sizes because in the MLO view the corner of the detector is positioned posterior to the patient's axilla (Hendrick et al 1999). This means that for small breasts, most of the tissue will be located off-center towards the superior side of the image.

The breast is varied using three parameters: chest wall to nipple distance (CND), compressed breast thickness (T), and glandular fraction (G). The CND was defined as the distance from the detector edge to the point in the breast skin farthest away from the body. With varying CND, the length of the breast along the chest wall and the size of the pectoralis were made to vary proportionally. In this study, the CND was varied from 7 cm to 19 cm, in steps of 3 cm, while the thicknesses used ranged from 2 to 8 cm, in 1 cm

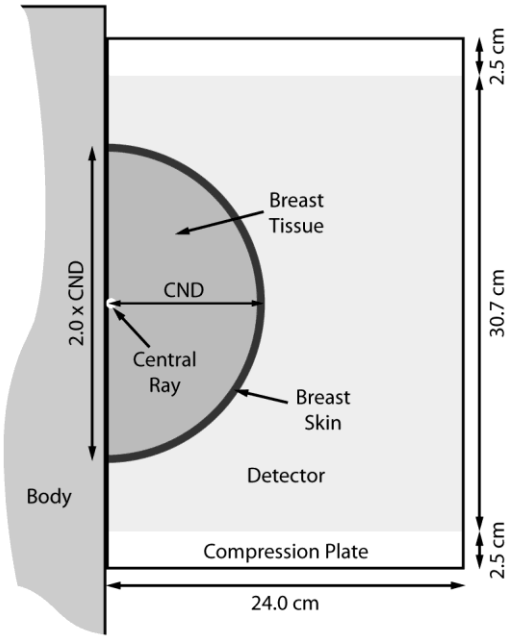

Figure 2.4 Diagram of the simulated CC view.

steps. The glandular fraction was defined as the weight fraction of the breast that consists of glandular tissue and was set to 1, 25, 50, 75, and 100%. The composition of the glandular and adipose tissues were defined as described by Hammerstein et al (Hammerstein et al 1979). The composition of the pectoralis was specified as that of skeletal muscle according to the International Commission on Radiation Units and Measurements (ICRU) Report 44 (International Commission on Radiation Units and Measurements 1989). For both views, the breast tissue was surrounded by a 4 mm layer of skin, and for backscatter purposes, the patient's body was included in the simulation, modeled as a large cuboid of water (75 x 34 x 17 cm).

The compressed breast in CC view was simulated as a semicircle with rounded edges, located at the centerline of the imager (Figure 2.4). The breast was defined using the same three parameters, CND, T and G. Since in this view the breast was modeled as a semicircle, the CND defines the radius of the semicircle. The values for thickness and glandular fraction used were the same as those for the MLO view, while the CND

was set so that the mass of the breast tissue coincided with that of the MLO view simulations' breast tissue mass, not including the pectoralis muscle. To match the breast mass, Geant4's function for calculation of the simulated breast tissue mass was used. Therefore, the CND values were: 6.2, 9.0, 11.6, 14.4, 17.0 cm.

Validation

To verify the photon attenuation coefficients used by Geant4 and the correct behavior of the simulation code, the program was modified so as to simulate x-rays traveling through breast tissue only, and the resulting attenuation coefficients were calculated. By activating and deactivating the different relevant physical interaction processes (photoelectric effect, Compton and Rayleigh scattering) in the Geant4 program, the linear attenuation coefficients of each process could be verified. These data were compared with the data reported by Hammerstein et al and the National Institute of Standards and Technology (NIST) (Hammerstein et al 1979; Berger et al 2005).

The simulation was also validated by comparing, under similar conditions, the values obtained for the 0° projection against those reported by Wu et al (Wu et al 1991; Wu et al 1994) and by Boone (Boone 2002).

Results

To verify that one million photon runs achieved enough statistical precision, the geometry in which the smallest number of photons would interact with the breast was repeated five times and the variation analyzed. The geometry used was that given by a CND of 7 cm and a thickness of 2 cm in the MLO view, and the coefficient of variation

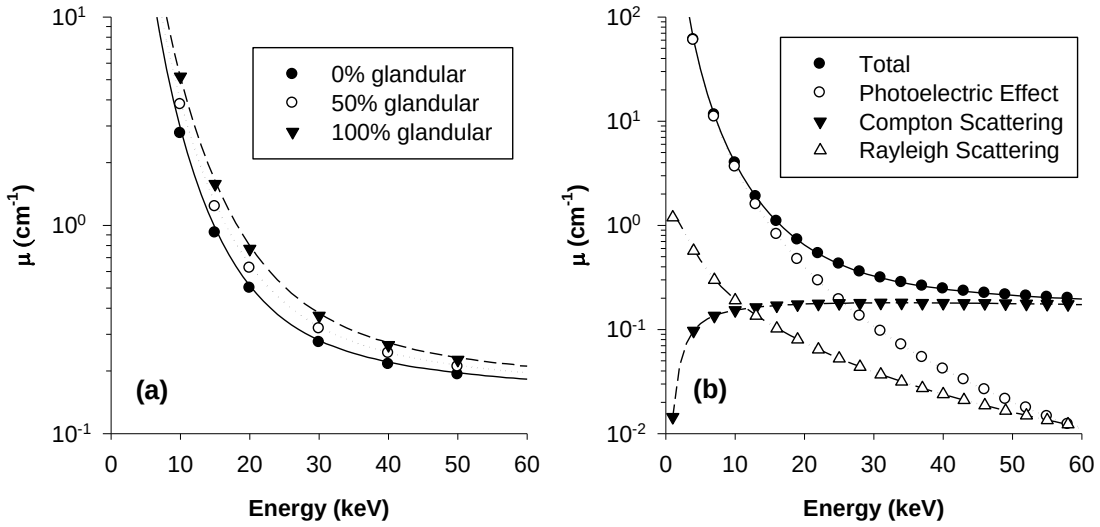

Figure 2.5 Comparison of the linear attenuation coefficients of (a) glandular tissue reported by Hammerstein et al (Hammerstein et al 1979) (symbols) and those resulting from the developed Geant4 program (lines), and (b) the three relevant physical interaction processes for the simulated breast tissue with 50% glandular fraction. The symbols are NIST's XCOM data (Berger et al 2005) and the lines show the data obtained from the developed Geant4 program.

(defined as the percentage ratio of standard deviation to the mean, $COV=100\sigma/\mu$) of the resulting D_gN values was found to be 0.47%.

Validation Results

Figure 2.5 shows the linear attenuation coefficients calculated from Geant4's simulations compared to those reported by Hammerstein et al (Hammerstein et al 1979) for breast tissue, and the decomposed linear attenuation coefficients compared to NIST's XCOM database (Berger et al 2005). In both cases excellent agreement was found. Figure 2.6 shows the D_gN values obtained from the Geant4 simulation compared to Wu et al's (Wu et al 1991) and Boone's data (Boone 2002) for matching geometries and compositions, respectively. In both cases good agreement was observed with excellent correlation ($r^2>0.998$ and $r^2>0.999$, respectively).

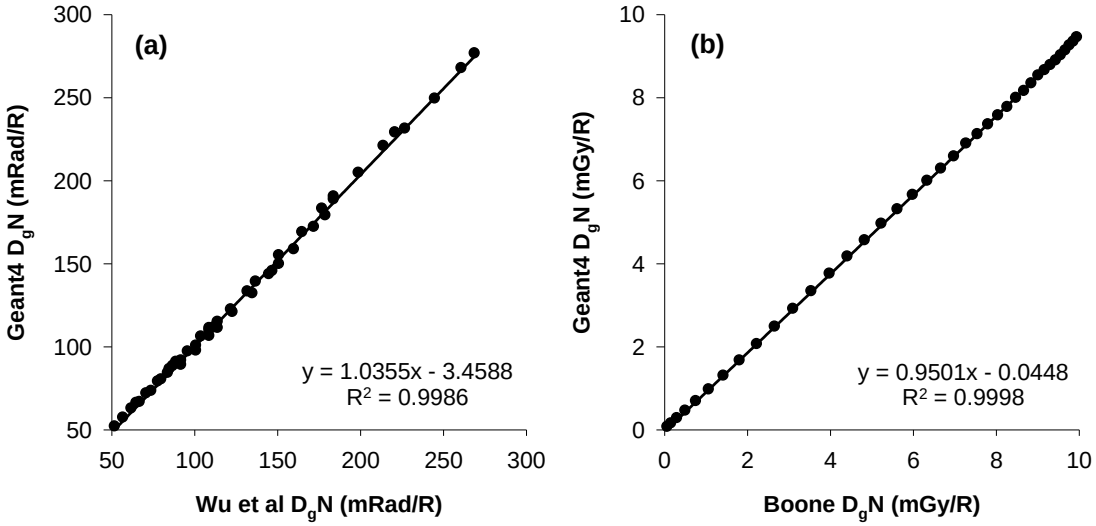

Figure 2.6 Comparison of D_gN values computed by the Geant4 program against those previously reported by (a) Wu et al (Wu et al 1991), and (b) Boone (Boone 2002). The lines represent the linear fit that result in the displayed equations.

Normalized Glandular Dose at Zero Degree Projection Angle

Table 2.2 shows the computed normalized glandular doses for the 0° projection angle, D_gN_0, as a function of compressed breast thickness, glandular fraction, and x-ray spectrum for the MLO and CC views. Although in this study D_gN_0 was computed for breasts with different chest wall to nipple distances, D_gN_0 was found to be very similar with varying CND, so the data reported here is the mean D_gN_0 for the 5 CND values simulated.

For the MLO view, the D_gN_0 for the CND=7 cm case is approximately 6-14% lower than the values reported in Table 2.2, while for breasts with CND of 10 cm or larger the reported D_gN_0 is accurate to within 6%. For the CC view, the maximum deviation from the mean D_gN_0 presented here is 3% for all breast sizes. For both views, as expected, increasing spectrum energy has a proportional effect on D_gN_0, while increasing thickness and glandular fraction show an inversely proportional relationship.

Table 2.2 Mean computed normalized glandular dose per unit exposure at the intersection of the central ray and the breast support plate (see Figure 2.2) for 0° projection angle, D_gN_0 (mGy/R).

Thickness (cm)	Spectrum (Target/Filter/kVp)	MLO View Glandularity (%)					CC View Glandularity (%)				
		1	25	50	75	100	1	25	50	75	100
2	Mo/Mo 25	2.33	2.19	2.05	1.92	1.80	2.59	2.43	2.28	2.13	2.00
	Mo/Mo 26	2.44	2.29	2.14	2.01	1.89	2.70	2.54	2.38	2.23	2.09
	Mo/Mo 27	2.53	2.38	2.23	2.10	1.97	2.81	2.64	2.48	2.33	2.18
	Mo/Rh 27	3.03	2.86	2.69	2.54	2.40	3.34	3.16	2.98	2.81	2.65
	Mo/Rh 29	3.19	3.02	2.85	2.69	2.54	3.52	3.34	3.15	2.97	2.81
	Rh/Rh 29	3.24	3.07	2.91	2.76	2.61	3.57	3.39	3.21	3.04	2.88
	Rh/Rh 31	3.45	3.28	3.11	2.95	2.80	3.79	3.61	3.42	3.25	3.09
	Rh/Rh 33	3.62	3.45	3.28	3.12	2.97	3.98	3.80	3.61	3.43	3.27
	Rh/Rh 35	3.78	3.60	3.43	3.26	3.11	4.15	3.96	3.77	3.59	3.42
3	Mo/Mo 25	1.81	1.65	1.50	1.37	1.25	2.01	1.83	1.66	1.51	1.38
	Mo/Mo 26	1.90	1.73	1.58	1.44	1.32	2.11	1.92	1.75	1.59	1.46
	Mo/Mo 27	1.99	1.81	1.65	1.51	1.38	2.20	2.01	1.83	1.67	1.53
	Mo/Rh 27	2.43	2.23	2.05	1.88	1.73	2.68	2.47	2.26	2.08	1.91
	Mo/Rh 29	2.58	2.37	2.18	2.01	1.85	2.85	2.62	2.41	2.22	2.04
	Rh/Rh 29	2.66	2.46	2.27	2.10	1.95	2.93	2.71	2.50	2.31	2.14
	Rh/Rh 31	2.85	2.65	2.45	2.27	2.11	3.14	2.91	2.70	2.50	2.32
	Rh/Rh 33	3.02	2.81	2.61	2.42	2.25	3.33	3.09	2.87	2.67	2.48
	Rh/Rh 35	3.17	2.95	2.74	2.55	2.38	3.49	3.24	3.02	2.81	2.62
4	Mo/Mo 25	1.45	1.29	1.16	1.04	0.93	1.61	1.44	1.28	1.15	1.03
	Mo/Mo 26	1.53	1.37	1.22	1.10	0.99	1.70	1.52	1.36	1.22	1.09
	Mo/Mo 27	1.60	1.43	1.28	1.15	1.04	1.78	1.59	1.42	1.28	1.15
	Mo/Rh 27	1.99	1.80	1.62	1.46	1.33	2.21	1.99	1.80	1.62	1.47
	Mo/Rh 29	2.12	1.92	1.73	1.57	1.42	2.36	2.13	1.92	1.74	1.58
	Rh/Rh 29	2.22	2.02	1.83	1.67	1.52	2.46	2.24	2.03	1.85	1.68
	Rh/Rh 31	2.40	2.19	1.99	1.82	1.66	2.66	2.42	2.20	2.01	1.84
	Rh/Rh 33	2.55	2.33	2.13	1.95	1.78	2.83	2.58	2.36	2.15	1.97
	Rh/Rh 35	2.69	2.46	2.25	2.06	1.89	2.98	2.73	2.49	2.28	2.09
5	Mo/Mo 25	1.20	1.06	0.94	0.83	0.74	1.33	1.17	1.03	0.92	0.82
	Mo/Mo 26	1.27	1.12	0.99	0.88	0.79	1.41	1.24	1.10	0.97	0.87
	Mo/Mo 27	1.34	1.18	1.04	0.93	0.83	1.48	1.31	1.15	1.02	0.91
	Mo/Rh 27	1.68	1.50	1.33	1.19	1.07	1.87	1.66	1.47	1.32	1.18
	Mo/Rh 29	1.80	1.60	1.43	1.28	1.15	2.00	1.78	1.58	1.42	1.27
	Rh/Rh 29	1.90	1.71	1.53	1.38	1.25	2.11	1.89	1.69	1.52	1.38
	Rh/Rh 31	2.06	1.86	1.67	1.51	1.37	2.29	2.06	1.85	1.67	1.51
	Rh/Rh 33	2.21	1.99	1.79	1.62	1.47	2.45	2.21	1.99	1.79	1.63
	Rh/Rh 35	2.33	2.11	1.90	1.72	1.57	2.59	2.34	2.11	1.91	1.73
6	Mo/Mo 25	1.03	0.90	0.79	0.69	0.62	1.13	0.99	0.86	0.76	0.67
	Mo/Mo 26	1.09	0.95	0.83	0.74	0.65	1.20	1.05	0.92	0.81	0.72
	Mo/Mo 27	1.14	1.00	0.88	0.78	0.69	1.26	1.10	0.96	0.85	0.76
	Mo/Rh 27	1.45	1.28	1.13	1.00	0.90	1.61	1.41	1.25	1.10	0.98
	Mo/Rh 29	1.56	1.37	1.21	1.08	0.97	1.73	1.52	1.34	1.19	1.06
	Rh/Rh 29	1.66	1.47	1.31	1.17	1.05	1.84	1.63	1.45	1.29	1.16
	Rh/Rh 31	1.81	1.61	1.43	1.29	1.16	2.00	1.78	1.59	1.42	1.28
	Rh/Rh 33	1.94	1.73	1.55	1.39	1.25	2.15	1.92	1.71	1.53	1.38
	Rh/Rh 35	2.05	1.84	1.64	1.48	1.34	2.28	2.03	1.82	1.63	1.47
7	Mo/Mo 25	0.90	0.78	0.68	0.60	0.53	0.98	0.85	0.74	0.65	0.57
	Mo/Mo 26	0.95	0.83	0.72	0.63	0.56	1.04	0.90	0.79	0.69	0.61
	Mo/Mo 27	1.00	0.87	0.76	0.67	0.59	1.10	0.95	0.83	0.73	0.64
	Mo/Rh 27	1.28	1.12	0.98	0.87	0.77	1.41	1.23	1.08	0.95	0.84
	Mo/Rh 29	1.37	1.20	1.06	0.94	0.83	1.52	1.33	1.16	1.03	0.91
	Rh/Rh 29	1.47	1.30	1.15	1.02	0.91	1.63	1.43	1.26	1.12	1.00
	Rh/Rh 31	1.61	1.42	1.26	1.12	1.01	1.78	1.57	1.39	1.24	1.11
	Rh/Rh 33	1.73	1.53	1.36	1.21	1.09	1.91	1.69	1.50	1.34	1.20
	Rh/Rh 35	1.83	1.63	1.45	1.30	1.16	2.03	1.80	1.60	1.43	1.28
8	Mo/Mo 25	0.79	0.69	0.60	0.52	0.46	0.87	0.75	0.65	0.57	0.50
	Mo/Mo 26	0.84	0.73	0.63	0.56	0.49	0.92	0.80	0.69	0.61	0.53
	Mo/Mo 27	0.89	0.77	0.67	0.59	0.52	0.97	0.84	0.73	0.64	0.56
	Mo/Rh 27	1.14	0.99	0.87	0.76	0.68	1.26	1.09	0.95	0.84	0.74
	Mo/Rh 29	1.22	1.07	0.93	0.83	0.73	1.35	1.18	1.03	0.90	0.80
	Rh/Rh 29	1.32	1.16	1.02	0.90	0.81	1.46	1.28	1.12	0.99	0.88
	Rh/Rh 31	1.44	1.27	1.12	0.99	0.89	1.60	1.40	1.24	1.10	0.98
	Rh/Rh 33	1.55	1.37	1.21	1.08	0.96	1.72	1.52	1.34	1.19	1.06
	Rh/Rh 35	1.65	1.46	1.29	1.15	1.03	1.83	1.62	1.43	1.27	1.14

Table 2.3 Sensitivity of the relative glandular dose, *RGD*(α), to the simulation parameters studied in this work.

View	Parameter Varied	Coefficient of Variation		Deviation from Mean	
		Mean	Maximum	Mean	Maximum
MLO	Glandularity	0.30%	1.42%	0.40%	1.87%
	X-ray Spectrum	0.75%	3.02%	1.01%	4.04%
	Thickness	2.86%	12.35%	4.38%	19.75%
	Chest-wall to Nipple Distance	10.26%	25.83%	14.49%	37.88%
CC	Glandularity	0.20%	0.84%	0.27%	1.10%
	X-ray Spectrum	0.60%	2.09%	0.82%	2.85%
	Thickness	1.00%	4.63%	1.64%	7.15%
	Chest-wall to Nipple Distance	0.89%	6.40%	1.30%	9.34%

Relative Glandular Dose Coefficients in MLO view

The *RGD* for all the geometries, glandular fractions and spectra used in this study were analyzed to find the effect each parameter has on *RGD*. For the MLO case, it was found that glandular fraction and spectrum have a weak effect on the values of *RGD*, while, as expected, CND and T, show a very important effect (example graphs are shown in Figure 2.7). To quantify the impact of each parameter on RGD, the variation of the latter when varying each one of the former while keeping all the other variables constant was computed using, as selected metrics, the *COV* and the percent deviation from the mean, defined as:

$$DFM = 100\frac{|RGD - \mu|}{\mu} \tag{2.3}$$

The results are shown in Table 2.3. The sensitivity of *RGD* to varying breast size and thickness shown by the variation metrics can be also seen in Figure 2.7(c) and Figure 2.7(d), which show that increasing breast size substantially changes the effect of projection angle on *RGD*, while increasing thickness increases the slope of *RGD* with tomosynthesis angle. Due to the position and geometry of the breast in the MLO view,

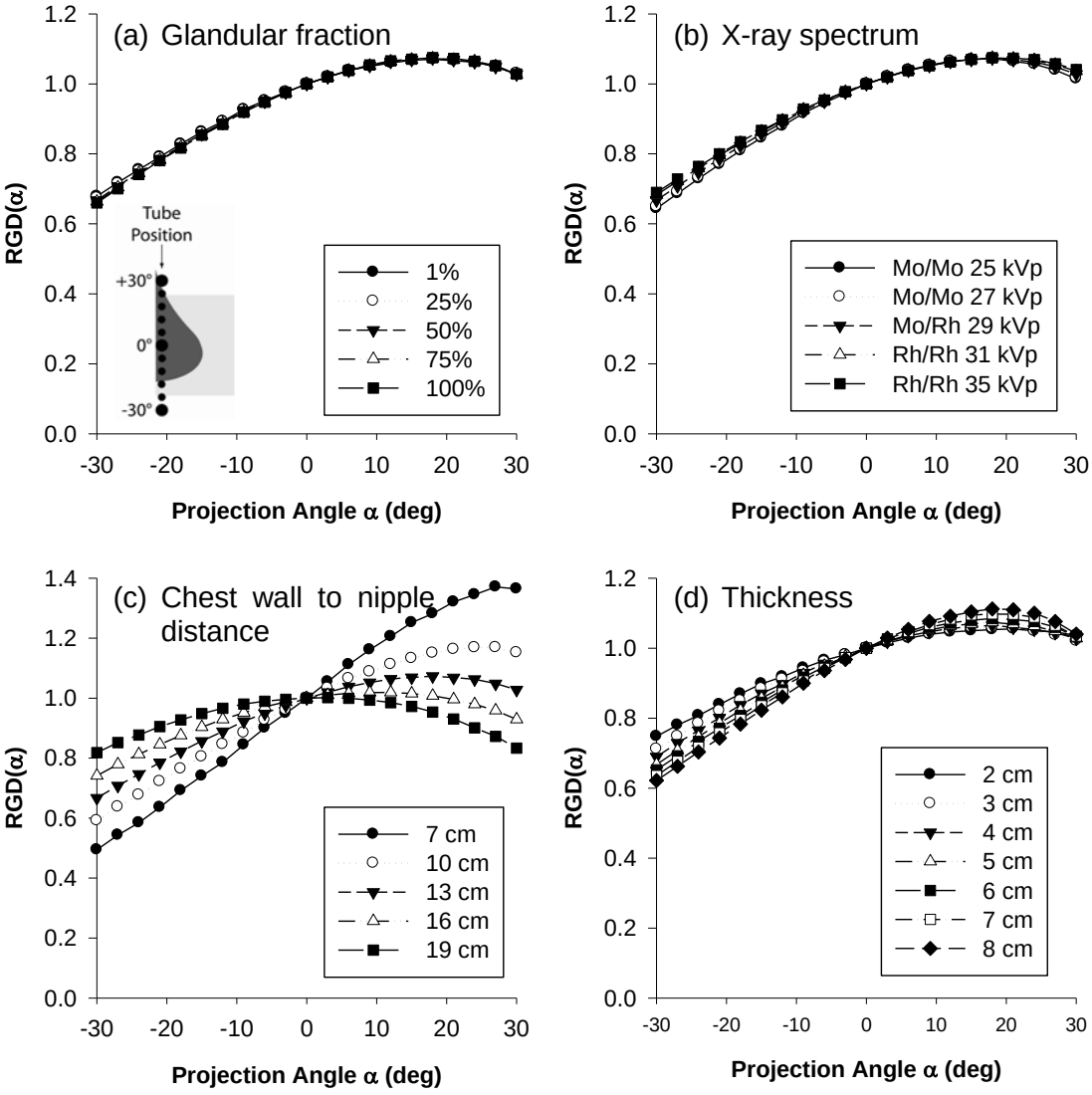

Figure 2.7 Sample graphs of *RGD* variation with varying (a) breast glandular fraction, (b) x-ray spectrum (only five spectra are included for visibility), (c) chest wall to nipple distance, (d) compressed breast thickness. All four graphs are for MLO view, CND = 13 cm, T = 5 cm, G = 50% and Mo/Rh 29 kVp x-ray spectrum, unless specified otherwise. Positive angle projections are defined as when the x-ray tube swings towards the cranial side of the patient. Note the different Y-axis scale in graph (c).

changes in breast size vary the relative location of most of the breast tissue on the detector. These displacements in breast tissue are what introduce the variations in the *RGD* distribution with projection angle observed in Figure 2.7(c).

The computed *RGD* was computer fit to functions of CND and angle, resulting in an equation for a surface for each thickness simulated. For simplicity, the *RGD* values were fit to the same equation for all T values, resulting in only different coefficients for each fit. The surface fits were performed using commercially available software (TableCurve 3D, Systat Software Inc., Richmond, California), and all seven fits resulted in an r^2>0.994. The equation for *RGD* for the MLO view is of the form:

$$RGD_{MLO} = \frac{a+c\alpha+e\delta+g\alpha^2+i\delta^2+k\alpha\delta}{1+b\alpha+d\delta+f\alpha^2+h\delta^2+j\alpha\delta} \qquad (2.4)$$

Where α is the tomosynthesis angle, in degrees; δ is the compressed breast chest wall to nipple distance, in cm; and *a* through *k* are the fit coefficients, given in Table 2.4.

Relative Glandular Dose Coefficients in CC view

A similar analysis was performed with the *RGD* data computed for the CC view (Figure 2.8). A weak dependence on glandular fraction and spectrum was found for *RGD*, while thickness and chest wall to nipple distance showed a much smaller effect on *RGD* in the CC view than in the MLO view. The results for the CC view are also shown in Table 2.3. The variation of *RGD* with T and CND were still deemed important enough so as to not fit *RGD* as only a function of projection angle. Therefore, the *RGD* values for CC view were also surface-fitted (r^2>0.995), using the same software, resulting in an equation for all seven thicknesses of the form:

$$RGD_{CC} = a+b\alpha+c\delta+d\alpha^2+e\delta^2+f\alpha\delta+g\alpha^3+h\delta^3+i\alpha\delta^2+j\alpha^2\delta \qquad (2.5)$$

Where the parameters are the same as those for the MLO fit, and the fit coefficients *a* through *j* are also specified in Table 2.4.

Table 2.4 Coefficients for the fit equations Equations (2.4) and (2.5) to compute relative glandular doses, *RGD*(*α*), for both the MLO and CC views.

T (cm)	a	b	c	d	e	f	g	h	i	j	k
MLO View											
2	1.03494E+0	-1.65291E-2	1.00774E-2	6.26922E-2	5.85952E-2	5.75274E-5	-1.72520E-4	-1.06080E-3	-9.39210E-4	8.10352E-4	-5.64650E-4
3	9.82852E-1	-2.23069E-2	1.00550E-2	8.43868E-2	8.70390E-2	8.21086E-5	-2.32480E-4	-1.77038E-3	-1.85537E-3	1.10061E-3	-5.62040E-4
4	1.02248E+0	-2.65315E-2	1.28243E-2	1.10024E-1	1.06782E-1	1.47124E-4	-2.47630E-4	-2.61289E-3	-2.49434E-3	1.18141E-3	-8.18180E-4
5	1.01833E+0	-2.85816E-2	1.26781E-2	9.50638E-2	9.23550E-2	1.88028E-4	-2.38960E-4	-2.02151E-3	-1.91150E-3	1.14239E-3	-9.30900E-4
6	9.93639E-1	-2.85375E-2	1.49711E-2	8.63644E-2	8.78953E-2	2.42803E-4	-2.17640E-4	-1.81360E-3	-1.86082E-3	9.04143E-4	-1.25308E-3
7	9.65189E-1	-2.45517E-2	1.11576E-2	1.71019E-2	2.37657E-2	2.23244E-4	-1.81270E-4	8.29182E-4	5.74141E-4	6.11906E-4	-1.12520E-3
8	9.47287E-1	-2.04840E-2	7.91617E-3	-3.96519E-2	-3.03155E-2	1.99299E-4	-1.45320E-4	2.97715E-3	2.62238E-3	3.68977E-4	-9.83380E-4
CC View											
2	9.76713E-1	-2.82880E-4	7.05012E-3	-1.21630E-4	-6.52770E-4	-1.04600E-5	-3.52440E-7	1.87954E-5	2.24852E-6	6.41383E-8	
3	9.86396E-1	3.84791E-4	3.61175E-3	-1.42520E-4	-2.69700E-4	-1.18920E-4	-2.08500E-7	5.79388E-6	7.09579E-6	-1.22720E-6	
4	9.85448E-1	9.06653E-4	3.47655E-3	-1.47280E-4	-2.37550E-4	-2.26040E-4	3.28555E-7	4.51560E-6	1.22245E-5	-3.39230E-6	
5	9.87935E-1	1.83842E-3	2.56731E-3	-1.36680E-4	-1.33900E-4	-3.78450E-4	2.85779E-7	1.10465E-6	1.76519E-5	-4.78660E-6	
6	9.59574E-1	2.75632E-3	1.11315E-2	-1.21930E-4	-9.11400E-4	-5.14030E-4	2.81729E-7	2.29331E-5	2.22628E-5	-6.52830E-6	
7	9.21211E-1	3.81409E-3	2.13709E-2	-7.12920E-5	-1.77956E-3	-7.23430E-4	-5.31470E-7	4.66016E-5	2.96015E-5	-8.40010E-6	
8	8.71762E-1	4.51444E-3	3.55204E-2	-5.57220E-5	-3.03082E-3	-8.40090E-4	-2.33850E-7	8.12397E-5	3.47119E-5	-1.10590E-5	

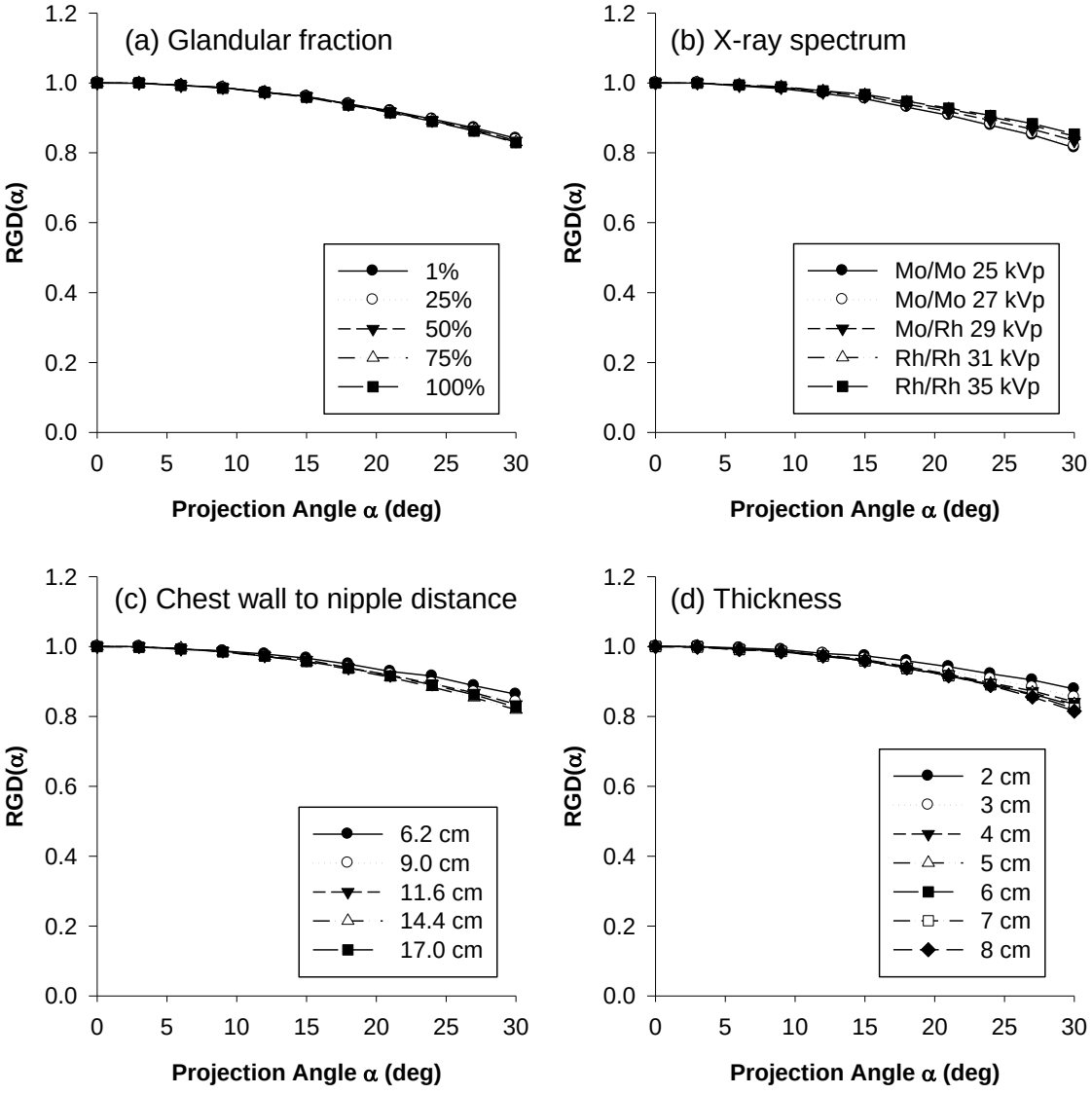

Figure 2.8 Sample graphs of *RGD* variation with varying (a) breast glandular fraction, (b) x-ray spectrum (only six spectra are included for visibility), (c) chest wall to nipple distance, (d) compressed breast thickness. All four graphs are for CC view, CND = 11.6 cm, T = 5 cm, G = 50% and Mo/Rh 29 kVp x-ray spectrum, unless specified otherwise.

Discussion

Comparison of D_gN_0 between the MLO and CC views shows that an MLO acquisition imparts a lower normalized glandular dose than a CC acquisition, by as much as 11%. This could be attributed to the fact that in the CC view model, the breast tissue is located around the central ray, where the photon fluence is highest. In the MLO view, the breast is located towards one side of the detector, where, due to the heel effect and inverse square distance relationship, the photon fluence is decreased. Also, more importantly, the pectoralis muscle present in the MLO view absorbs a portion of the dose that would otherwise be absorbed by the breast tissue. The presence of the pectoralis muscle in the compressed breast acts as a shield for the breast tissue under it, resulting in a lower total dose to the breast tissue. The energy deposited in the muscle tissue was found to range from 1.5-12% of that deposited in the breast tissue, varying inversely with breast thickness. When a breast is compressed in the MLO position it is almost always of greater thickness than when it is compressed in the CC position (Young et al 2000; Jamal et al 2003). Therefore, for MLO view images a higher exposure is used than for CC view images, resulting in a higher total dose even though the D_gN_0 is lower.

Given the definition of $RGD(\alpha)$, if the mean RGD, μ_{RGD}, of a complete tomosynthesis study is under 1, then the study will result in a lower total glandular dose than a planar mammography study, if the mAs setting for all the projections in the tomosynthesis study is constant and the sum of the mAs used equals that of the planar study. Similarly, if μ_{RGD} is over 1, the tomosynthesis study will result in a higher glandular dose than the equivalent planar study. If in an advanced tomosynthesis system the mAs is adjusted for each projection, this can be taken into account by incorporating the increase at each angle into Equation (2.2). Furthermore, if the kVp setting is also varied with angle, then the total dose of the study can also be computed by multiplying each

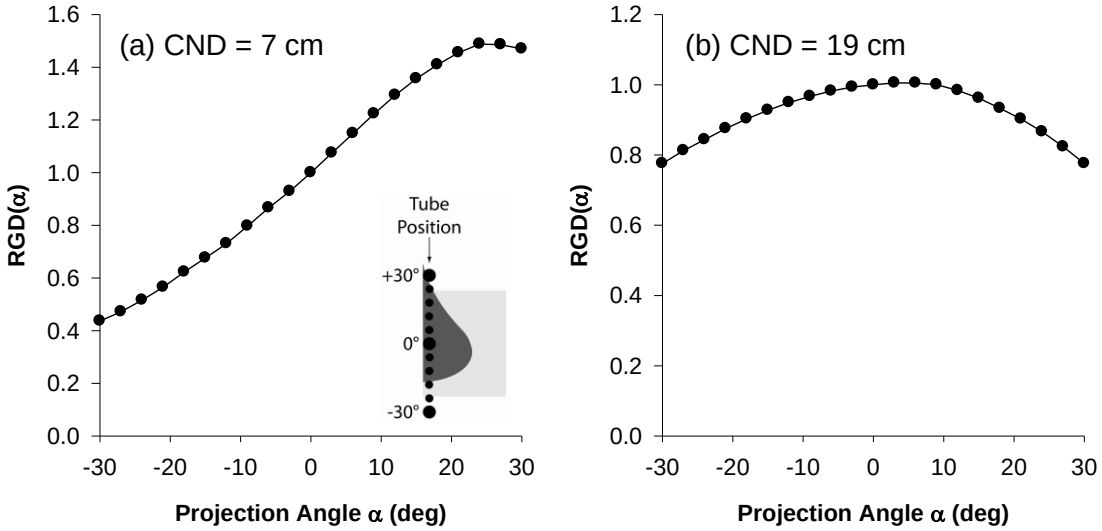

Figure 2.9 Graphs of RGD versus projection angle for (a) CND = 7 cm, T = 8 cm, and (b) CND = 19 cm, T = 8 cm, both for the MLO view.

angle's coefficient by its corresponding D_gN_0 and then totaling the normalized glandular doses.

Using the tomosynthesis protocol reported for a current prototype tomosynthesis system (Eberhard et al 2006) (21 views over an angular range of α=±30°, in 3° steps), μ_{RGD} can be calculated for different breast parameters. For all the sets of possible parameter values (1,575 combinations) used in this study in the MLO view the maximum μ_{RGD} for the protocol described above is 1.01, while the minimum is 0.91. For the CC view the maximum and minimum μ_{RGD} are 0.97 and 0.91, respectively. This means that for the tomosynthesis protocol described, conventional mammography dosimetry could overestimate the dose to the breast by almost 10% for both views. This seemingly small deviation from unity of μ_{RGD} is not due to the individual $RGD(\alpha)$ values being always close to unity. In the cases where the $RGD(\alpha)$ deviates considerably from unity, the $RGD(\alpha)$ distribution's approximate negative symmetry about 1 ($RGD(-\alpha) = 1 - (RGD(\alpha) - 1)$) still results in a μ_{RGD} of approximately 1 (Figure 2.9(a)). Specifically, for the breast

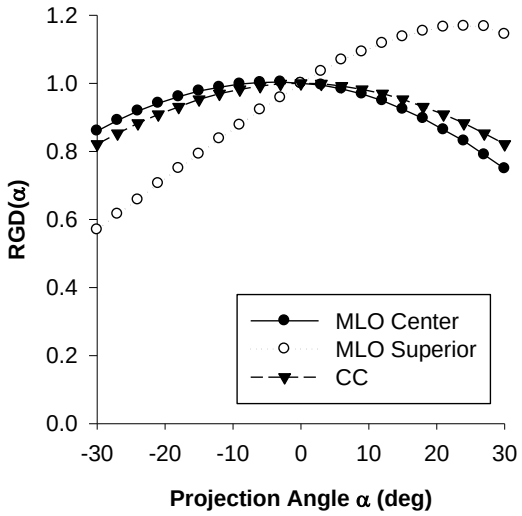

Figure 2.10 Graph of RGD versus projection angle for a small breast in MLO view located at the superior portion and at the center portion of the detector.

with CND=7 cm and T=8 cm, the extreme individual $RGD(\alpha)$ values are 0.44 to 1.47, but the resulting μ_{RGD} is 1.0. In the MLO views where CND is large (e.g. CND=19 cm, T=8 cm), $RGD(\alpha)$ has a distribution which is approximately positive symmetric ($RGD(-\alpha) = RGD(\alpha)$) about the zero degree projection angle, resulting in a μ_{RGD} of 0.92 (Figure 2.9(b)). Therefore, in this case, the total glandular dose to the breast during a tomosynthesis study will be 8% lower than that of a planar mammography study performed with equal total mAs. In addition, it must be noted that a small breast results in a higher μ_{RGD} than that for a large breast. The CC view with large CND results in approximately the same μ_{RGD} as that of the MLO view.

In case that some small breasts are placed in the center of the detector for the MLO view rather than towards the superior side, some simulations were repeated to study this positioning. Using a small breast of varying thickness (CND=10 cm, T=2, 5, and 8 cm, G=50%) with the MLO view shape but positioned about the centerline of the imager, simulations were performed for the ±30° range in 3° steps, and the resulting $RGD(\alpha)$ was computed. The results for the T=5 cm case are displayed in Figure 2.10. As

can be seen from the graph, the *RGD*(*α*) for the MLO view breast, when centered on the detector, presents a very similar distribution with projection angle to that of the CC view of equivalent mass. Similar results were found for the breasts with T=2 and 8 cm. Therefore, the fit equation for *RGD*(*α*) for the CC view could be used to compute doses for MLO view breasts positioned in this manner. These results are expected since the small size of the breast make the difference in shape relatively unimportant.

A simulation with a median geometry (CND=13 cm, T=5 cm, G=50%) was repeated without taking into account the heel effect in the x-ray field distribution. Therefore, the only non-uniformity present in the x-ray fluence was due to the divergence of the x-rays from the point source, which follows the inverse square law. As expected, it was found that the removal of the heel effect has a substantial effect in the D_gN_0 values, which increased by approximately 7% for all spectra, while the *RGD*(*α*) was minimally affected, the variation ranging from 0% to 0.5%, with a mean variation of 0.14%.

Additional simulations were performed with two different values for the distance from the detector surface to the x-ray tube's center of rotation (DCOR), originally 4 cm in this study. This distance was specified as 0 cm (center of rotation at the detector surface) and 8 cm above the detector surface. The source to detector distance at the zero degree projection angle was maintained at 66 cm. Simulations with these two values for DCOR were performed for CND=13 cm for MLO view (11.6 cm for CC view), T=2, 5 and 8 cm and G=50%. For both views the *RGD*(*α*) was found to be directly proportional with DCOR, having lower values compared to the original study's data with DCOR=0 cm and higher with DCOR=8 cm (Figure 2.11). For the MLO view, the values for *RGD*(*α*) varied by a maximum at the extreme angles of approximately 5%, while for the CC view the maximum deviations were found to be of approximately 2%, both in relation to the values found for the original study of DCOR=4 cm. These results could be

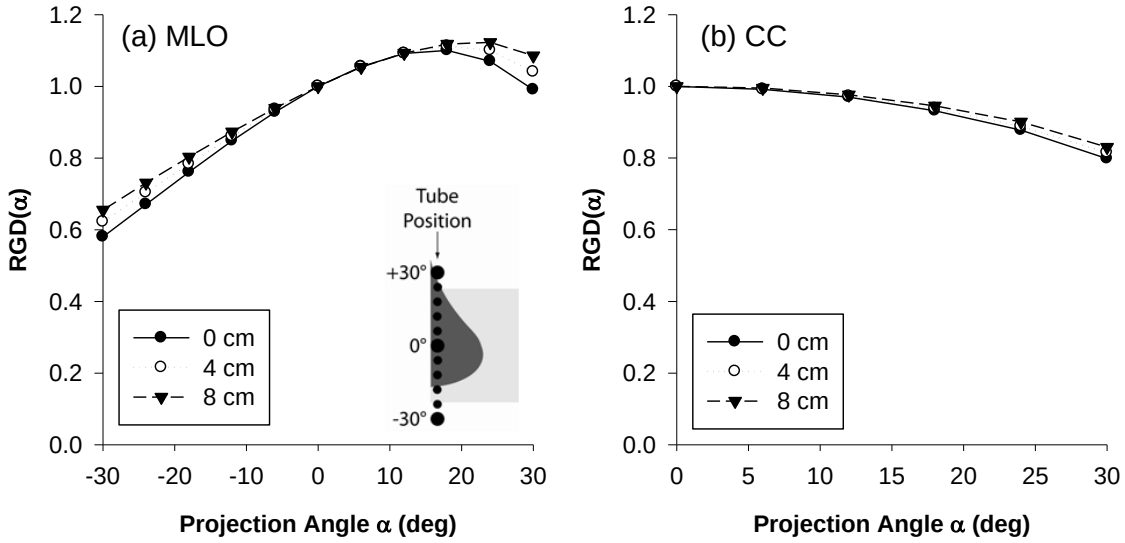

Figure 2.11 Graphs of *RGD* versus projection angle for three different detector to x-ray tube center of rotation distances for the (a) MLO view, and the (b) CC view.

explained by the fact that a higher center of rotation results in a shorter distance from the x-ray source to the compressed breast at non-zero projection angles compared to the distance for a lower center of rotation. Therefore, since the x-ray source is closer to the compressed breast, the relative glandular dose is higher.

These additional simulations show that the tables and equations reported in this study are approximately valid for tomosynthesis systems with some deviations, such as different x-ray fluence non-uniformities and different locations of the x-ray tube's center of rotation. However, this study is not necessarily applicable to tomosynthesis projection geometries in which the detector rotates in conjunction with the x-ray tube. This limitation is especially true for the MLO view dose simulations, for which some of the breast tissue falls outside the x-ray field at certain tomosynthesis projection angles. These results would be applicable for small to medium sized breasts in the CC view, for which the whole breast is always within the x-ray field.

Conclusion

Conventional mammographic dosimetry was not designed to address the complex geometry of tomosynthesis projections. In this study, it was found that geometric asymmetry, specific characteristics of the MLO view, varying x-ray field collimation, and inclusion of the heel effect result in a complex variation of normalized glandular dose with projection angle. For a complete tomosynthesis acquisition, the normalized glandular dose to the breast, when computed with conventional dosimetry was found to be over-estimated by as much as approximately 10%. Although this percentage difference might be deemed unimportant compared to the errors introduced by the necessary approximations of this type of simulations (breast geometry variations, tissue inhomogeneities, etc.), it is important to note that for some projection angles the deviation was found to be as much as 56%, which could introduce important deviations if advanced tomosynthesis protocols, such as varying mAs with projection angle, are introduced.

This new model of dosimetry can be used for a more realistic and accurate characterization of the normalized glandular dose in digital tomosynthesis of the breast than that obtained from the conventional mammography models. This model allowed for a comprehensive characterization of the parameters involved in tomosynthesis dosimetry, giving insight into which imaging and geometric parameters are important to consider when performing a tomosynthesis dosimetry calculation.

CHAPTER 3

WHOLE BODY DOSIMETRY IN MAMMOGRAPHIC IMAGING

Introduction

In Chapter 2 the dose to the imaged breast during a tomosynthesis imaging study was investigated. That data, along with previously published reports on dose to the imaged breast for standard (planar) mammography (Hammerstein et al 1979; Dance 1980; Doi et al 1980; Dance 1990; Wu et al 1991; Wu et al 1994; Boone 1999; 2002) and for dedicated breast computed tomography (Boone et al 2004; Thacker et al 2004) provides a comprehensive database of the radiation dose to the breast involved in all three mammography procedures. However, the doses received by the other organs and tissues of the body from any type of mammographic procedure are unknown. Data about organ dose during mammographic acquisition will help the study of issues relating to the safety of mammograms during pregnancy, and the epidemiological study of radiation related onset of specific diseases (Preston-Martin et al 2003). In more practical terms, radiologists have adequate data to communicate the radiation dose delivered to the breast in mammography but no detailed data are available on radiation dose to other tissues as a result of this procedure. This information is important for patients who were not aware they were pregnant at the time of the procedure and for pregnant women with suspected breast abnormalities that may warrant mammography. At present, only one study (Hatziioannou et al 2000) has been published on the radiation dose to the other organs of the human body from a planar mammography procedure, and no studies have been reported on dose to the other organs from tomosynthesis or DBCT. That study, using a phantom and thermoluminescence dosimetry, reported the measured dose in a limited number of organs and tissues.

An advanced Monte Carlo program was used to simulate the human body and the conditions present during planar and tomographic mammographic imaging to compute the radiation dose to each of 66 tissues in the body. In this chapter, the methodology and results for the planar and tomosynthesis breast imaging is presented, while the DBCT imaging case is presented in the next chapter.

Methods

With the use of the Geant4 toolkit (Agostinelli et al 2003; Allison et al 2006) for Monte Carlo simulations, a C++ computer program was implemented to simulate a representation of the human body based on the current version of the Cristy phantom (ORNL Center for Biokinetic and Dosimetric Research 2005), developed by Cristy and Eckerman (Cristy 1980) at the Oak Ridge National Laboratory (ORNL). In addition to the anthropomorphic phantom, the simulation included the main components of a mammography imaging system; an x-ray point source as an approximation of the focal spot of the mammographic x-ray tube, the breast compression plate, the breast support plate, and the x-ray detector with cover plate. It must be noted that this geometry is applicable for both planar mammography as well as tomosynthesis imaging of the breast.

Anthropomorphic phantom

The Cristy phantom consists of a representation of the human body and its organs with the use of geometrical shapes based on mathematical formulas. With the use of different parameters for the formulas the phantom is adjusted to represent a human body of six different ages. The phantom used in this study is that which represents an adult female (denoted in the ORNL report as “15-AF”).

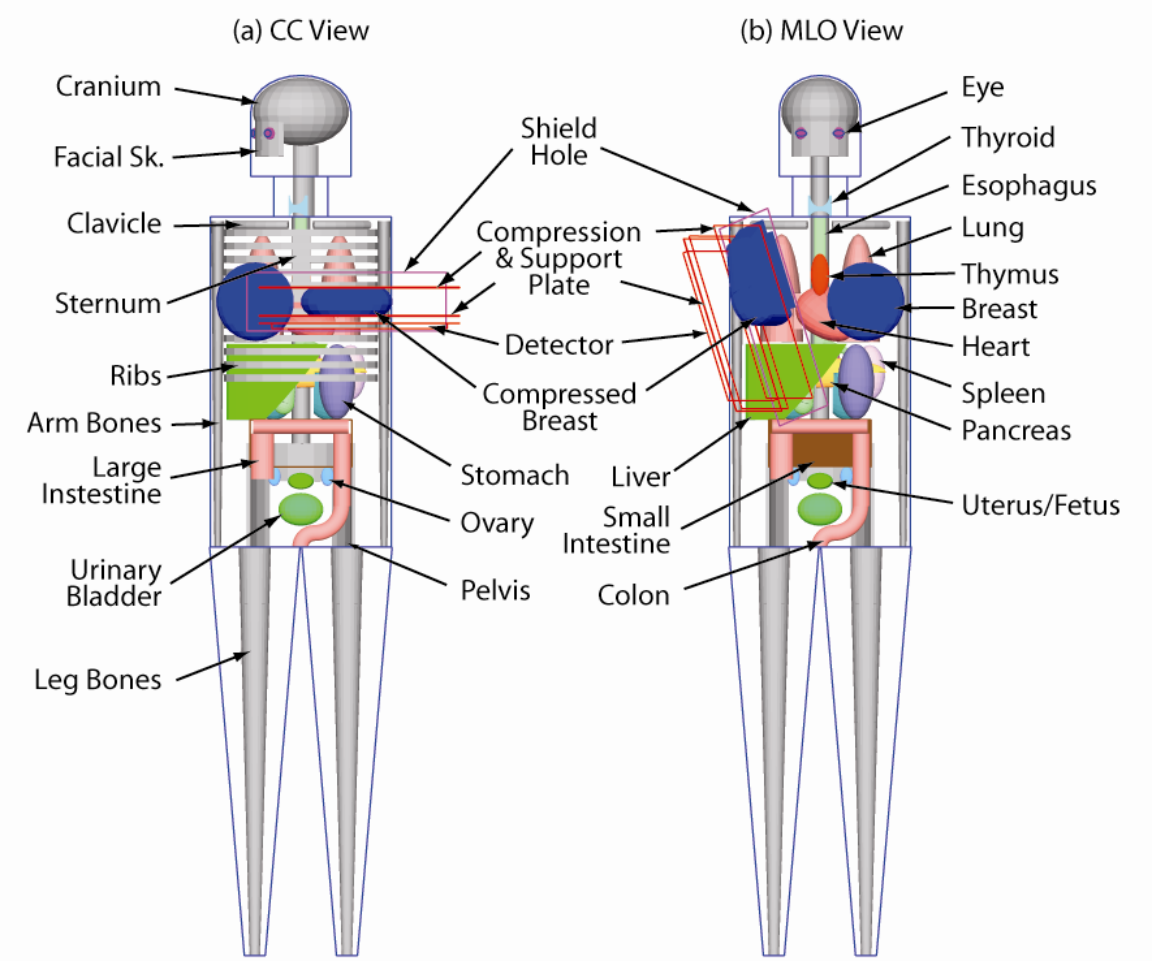

Figure 3.1 Simulation geometry used in this study for the (a) CC view and (b) MLO view. In the CC view, only the small intestine's outline is included to show the pelvis. In the MLO view the rib cage and the sternum are omitted to show the other organs.

In this implementation of the Cristy phantom (Figure 3.1), some modifications were made to enhance the simulation, adapt the geometrical shapes to Geant4's capabilities, and to recreate the conditions present during breast imaging. The major modifications, based on data from the International Commission on Radiological Protection (ICRP) Publication 89 (International Commission on Radiological Protection 2002) and the ICRU Report 46 (International Commission on Radiation Units and Measurements 1992) and anatomy literature (Gray et al 1973), were the use of different elemental compositions and densities for each tissue, and the addition of the eyes, eye

lenses and sternum to the phantom. Two geometrical adaptations were introduced in the phantom to allow for a simpler implementation in Geant4. These were the re-orientation of the legs so that their long axis was vertical as opposed to at an angle as in the original description, and the cross-section of the tori representing the sigmoid colon were circular, as opposed to elliptical. These modifications were estimated to have a negligible impact on the results. The adaptations necessary to recreate the conditions during a breast imaging study were simulating the imaged breast as compressed either horizontally for the CC view or at an angle for the MLO view, and rotating the head of the phantom towards the opposite side of the imaged breast in the CC view. The anthropomorphic phantom in this simulation had a total of 66 organs, bones, skin sections and other soft tissues, listed, along with their mass, in Table 3.1.

The compressed breast in the CC view was modeled in a similar fashion as that used in Chapter 2, namely, as a semicircular cylinder with rounded edges. In this study, the CND was set to 10 cm and the thickness of the compressed breast to 5.2 cm. This size represents a mean breast in the CC view (Boone et al 2000b). The compressed breast in the MLO view was also similar to that used in the previous chapters, with a compressed thickness of 5.7 cm, and a CND of 10.2 cm. The thickness of the MLO view breast was chosen to be approximately 10% thicker than that of the CC view (Young et al 2000; Jamal et al 2003), while the CND was chosen so that the mass of the breast tissue was equal to that in the CC view. The breast in both views was implemented as a homogeneous mixture of 50% glandular and 50% adipose tissue, as described by Hammerstein et al (Hammerstein et al 1979). The elemental composition of the pectoralis muscle used in the MLO view breast was specified as that of skeletal muscle (International Commission on Radiation Units and Measurements 1989). The contents of the organs of the digestive system were specified as water, while the heart was filled with blood.

Table 3.1 List of organs, bones, skin sections and soft tissue volumes that compose the anthropomorphic phantom used in this study and their respective mass.

Tissue Type	Name	Mass (g)
Organ	Adrenal	5.1
	Brain	1407.6
	Breast	601.6
	Colon (ascending)	71.6
	Colon (transverse)	95.2
	Colon (descending)	70.4
	Colon (sigmoid)	55.4
	Esophagus	34.3
	Eye	6.6
	Eye Lens	0.2
	Gall Bladder	9.1
	Heart	242.7
	Kidney	125.2
	Liver	1425.5
	Lung (left)	266.1
	Lung (right)	305.4
	Ovary	5.4
	Pancreas	64.9
	Pectoralis Muscle of Imaged Breast	116.5
	Small Intestine	830.4
	Spleen	125.6
	Stomach	116.5
	Thymus	28.0
	Thyroid	12.1
	Urinary Bladder	35.5
	Uterus/Fetus	78.2
Skeleton	Arm Bone (lower section)	173.6
	Arm Bone (middle section)	145.1
	Arm Bone (upper section)	193.0
	Clavicle	29.2
	Cranium	711.5
	Facial Skeleton	92.8
	Leg Bone (lower section)	484.6
	Leg Bone (middle section)	588.6
	Leg Bone (upper section)	396.1
	Pelvis	644.0
	Rib Cage	725.8
	Scapulae	104.8
	Spine	1059.1
	Sternum	58.1
Soft Tissue	Head	2108.1
	Leg	7033.0
	Neck	561.8
	Trunk	24892.2
Skin	Breast	76.4
	Head	205.1
	Leg	514.5
	Neck	47.8
	Trunk	1068.2

Monte Carlo simulation

To simulate the acquisition of a planar mammogram or a tomosynthesis projection set, the compression plate, support plate, and detector were placed in the appropriate location according to the simulated mammographic view and the imaged breast in a geometry equivalent to that shown in Figure 2.3 and Figure 2.4. The air gap between the support plate and the detector cover plate was set to 1.5 cm. The x-ray source, approximated as a point source, was located at a SID of 66 cm for the 0º tomosynthesis projection, while the DCOR was set to 0 cm. For this study, the tomosynthesis projection set simulated consisted of 11 projections, over an angular range of ±30º. The Monte Carlo results for these angles were later interpolated to represent a tomosynthesis projection set consisting of 21 projections over the same angular range, which is one of the acquisition protocols presently used in a prototype machine (Eberhard et al 2006). To study the dosimetry involved with planar mammography, the results for the 0º projection alone were used as representative of standard planar mammographic imaging.

At each projection angle and at each energy level sixty million monochromatic x-rays were emitted from the point source towards a random location on the detector surface so that the x-ray field at the detector surface was uniform and congruent with the detector edges. The path traveled by the x-rays was followed until the x-ray either exited the simulation limits or was completely absorbed. The energy lost by the x-ray at each interaction, along with the organ in which the deposition took place, was recorded. The total energy deposited in the imaged breast was used to compute the glandular dose as described in Chapter 2, while the total energy deposited in the other organs was divided by each organ's mass to obtain the dose to each organ. For each projection angle the simulation was repeated with monochromatic x-rays of energies ranging from 6 to 40 keV in 1 keV steps. Due to the asymmetry of the distribution of the organs, the

Table 3.2 List of x-ray spectra used in this study, along with their first half value layers.

Target	Filter	Tube Potential (kVp)	HVL above Compression Plate (mm Al)	HVL under Compression Plate (mm Al)
Mo	Mo	25	0.284	0.322
Mo	Mo	30	0.340	0.378
Mo	Mo	35	0.380	0.417
Mo	Rh	25	0.336	0.371
Mo	Rh	30	0.397	0.431
Mo	Rh	35	0.434	0.465
Mo	Rh	40	0.459	0.488
Rh	Rh	25	0.314	0.353
Rh	Rh	30	0.395	0.442
Rh	Rh	35	0.458	0.508
Rh	Rh	40	0.507	0.557

simulations were performed for both breasts. The monochromatic results were interpolated to 0.5 keV resolution and combined by weighing them with the relative number of photons in each spectrum studied. The simulated spectra (Boone et al 1997) used and their first half value layers are listed in Table 3.2. As previously mentioned, to study the dosimetry to the organs from tomosynthesis the results for the 11 projections simulated were interpolated to obtain a 3º angular step (a total of 21 projections) using a piecewise polynomial fit, and the resulting data was combined to represent a complete tomosynthesis acquisition. To obtain the dosimetry results for planar mammography, only the 0º projection angle data was used.

The dose to each organ was normalized to that of the glandular dose to the breast, resulting in the relative organ dose (ROD), representing the dose to an organ in the body per unit glandular dose to the breast. The simulations were performed in the same computer cluster as that used for the previous Monte Carlo studies.

Computation of dose to the red bone marrow and the bone surfaces

Bone dosimetry is affected by the complex microscopic histological features of the bones which are impossible to account for in macroscopic Monte Carlo simulations. Therefore, the development of methodologies to compute dose to the bone surfaces (BS) and to the red bone marrow (RBM) from macroscopic data has been an issue of intense research (Rosenstein 1976; Kramer et al 1982; King et al 1985; Cristy et al 1987; Zankl et al 2001; Kramer et al 2003; Kramer et al 2004; Lee et al 2006). In this study, the dose to the RBM was estimated using the three-parameter mass-energy absorption coefficient ratio method (MEAC) (Rosenstein 1976; Kramer et al 1982; King et al 1985; Lee et al 2006). This method has been shown to obtain results comparable to all other methods applicable to a macroscopic Monte Carlo simulation (Lee et al 2006). To compute the dose to the BS, the homogeneous bone approximation (HBA) (Lee et al 2006) was used, which assigns the dose to the whole homogeneous bone volume as the dose to the BS. These two methods have been shown to overestimate the dose to the RBM and BS at the low energy range, so the results in this study represent a conservative upper limit (Lee et al 2006).

Study of possible dose reduction with a lead shield

To study the possibility of reducing the radiation dose to the organs of the body, a virtual 0.25 mm thick lead shield between the simulated patient and the x-ray field was included in the simulations. In the simulation the shield was implemented as transparent to the x-rays, but the fact that the x-ray had entered the shield was recorded. With this record, a second computation of the dose to the organs was performed, in which the dose deposited in the organs by x-rays that were flagged as having entered the shield was ignored. This allowed for the simultaneous computation of the dose to the organs with and without shield. The only assumption necessary for this algorithm to work was

that the lead shield was thick enough to absorb all x-rays that entered it. This was accomplished by simulating the shield as having a thickness of 0.25 mm, which results in an absorption of 98.3% of x-rays of 40 keV.

The shield was simulated as large enough to cover the whole body, with an opening for the imaged breast with length along the chest wall of 20 cm and a height of 11 cm.

Validation

The breast in the CC view was modified to match the geometry reported by Boone (Boone 2002), and the simulations were repeated with one million monochromatic x-rays from 6 to 35 keV, in 1 keV steps for the 0º projection angle. The resulting glandular dose to the breast was compared to the results reported in that study. The mean deviation between the resulting data and the fit equation reported by Boone was 7.2%. In addition, the attenuation coefficients and the x-ray scatter functions in mammography used by Geant4 were validated in other chapters of this work and in published reports (Grabski et al 2005; Sechopoulos et al 2006), pointing to the applicability of this package in the study of dosimetry related to x-rays scattered in the breast.

Results

Table 3.3 (CC view) and Table 3.4 (MLO view) show the ROD value for the organs, bones (discriminated into bone surfaces and red bone marrow), and skin sections during tomosynthesis imaging. Except the uterus, only the volumes that received a ROD of 0.10% or higher in at least one view and one spectrum are included in the tables. Doses that resulted in a ROD lower than this level were deemed negligible

Table 3.3 Dose to the organs, bones and skin sections per unit dose to the imaged breast (ROD) in the CC view

Tissue Type	Volume	Mo/Mo			Mo/Rh				Rh/Rh			
		25 kVp	30 kVp	35 kVp	25 kVp	30 kVp	35 kVp	40 kVp	25 kVp	30 kVp	35 kVp	40 kVp
Organ	Breast (CL)	0.44%	0.46%	0.49%	0.46%	0.48%	0.50%	0.53%	0.72%	0.73%	0.73%	0.73%
	Eye (IL)	0.08%	0.08%	0.08%	0.08%	0.07%	0.08%	0.08%	0.09%	0.09%	0.09%	0.09%
	Eye Lens (IL)	0.10%	0.10%	0.10%	0.10%	0.09%	0.10%	0.10%	0.11%	0.11%	0.11%	0.11%
	Heart	0.01%	0.03%/0.02%	0.08%/0.05%	0.03%/0.02%	0.04%/0.03%	0.08%/0.05%	0.13%/0.08%	0.40%/0.22%	0.40%/0.22%	0.39%/0.22%	0.39%/0.21%
	Liver	0.00%	0.00%	0.00%	0.00%	0.00%	0.00%	0.00%	0.01%/0.04%	0.01%/0.03%	0.01%/0.03%	0.01%/0.03%
	Lung (IL)	0.01%	0.03%/0.04%	0.08%/0.09%	0.02%	0.04%	0.08%	0.13%/0.15%	0.41%/0.46%	0.40%/0.46%	0.40%/0.46%	0.39%/0.45%
	Stomach	0.00%	0.00%	0.00%	0.00%	0.00%	0.00%	0.01%	0.01%	0.01%	0.01%	0.01%
	Thymus	0.02%	0.04%	0.09%	0.03%	0.05%	0.09%	0.15%	0.45%	0.45%	0.45%	0.44%
	Uterus or Fetus	0.00000044%	0.0000027%	0.0000092%	0.0000015%	0.0000035%	0.0000087%	0.000021%	0.000061%	0.000056%	0.000054%	0.000053%
Bone Marrow	Arm Bone (upper section, IL)	0.03%	0.04%	0.05%	0.04%	0.04%	0.05%	0.06%	0.12%	0.12%	0.12%	0.12%
	Clavicle (IL)	0.05%	0.06%	0.08%	0.06%	0.07%	0.08%	0.11%	0.23%	0.23%	0.23%	0.23%
	Rib Cage	0.08%	0.10%	0.13%	0.10%	0.12%	0.14%	0.18%	0.40%	0.40%	0.40%	0.40%
	Sternum	0.33%	0.38%	0.46%	0.38%	0.43%	0.49%	0.57%	1.09%	1.10%	1.10%	1.09%
Bone Surface	Arm Bone (middle section, IL)	0.08%	0.10%	0.13%	0.10%	0.11%	0.14%	0.18%	0.37%	0.37%	0.37%	0.37%
	Arm Bone (upper section, IL)	0.13%	0.16%	0.20%	0.15%	0.18%	0.21%	0.26%	0.52%	0.52%	0.52%	0.51%
	Clavicle (IL)	0.19%	0.24%	0.33%	0.23%	0.28%	0.34%	0.44%	0.99%	0.98%	0.98%	0.97%
	Clavicle (CL)	0.06%	0.07%	0.09%	0.07%	0.08%	0.09%	0.11%	0.23%	0.23%	0.23%	0.22%
	Facial Skeleton	0.01%	0.02%	0.02%	0.02%	0.02%	0.02%	0.03%	0.06%	0.06%	0.06%	0.06%
	Ribs	0.33%	0.42%	0.56%	0.42%	0.50%	0.61%	0.74%	1.68%	1.69%	1.70%	1.69%
	Sternum	1.37%	1.62%	1.96%	1.61%	1.82%	2.08%	2.39%	4.58%	4.62%	4.63%	4.61%
Skin	Breast (IL)	255.04%	227.98%	211.79%	225.89%	205.49%	195.40%	188.79%	128.43%	126.14%	124.67%	124.47%
	Breast (CL)	2.19%	2.04%	1.96%	2.02%	1.91%	1.86%	1.84%	1.58%	1.57%	1.56%	1.56%
	Head	0.53%	0.47%	0.43%	0.46%	0.42%	0.40%	0.38%	0.27%	0.27%	0.26%	0.26%
	Neck	0.18%	0.16%	0.15%	0.16%	0.14%	0.13%	0.13%	0.10%	0.10%	0.10%	0.10%
	Trunk	0.60%	0.56%	0.54%	0.55%	0.52%	0.51%	0.50%	0.45%	0.45%	0.45%	0.45%

Table 3.4 Dose to the organs, bones and skin sections per unit dose to the imaged breast (ROD) in the MLO view

Tissue Type	Volume	Mo/Mo			Mo/Rh				Rh/Rh			
		25 kVp	30 kVp	35 kVp	25 kVp	30 kVp	35 kVp	40 kVp	25 kVp	30 kVp	35 kVp	40 kVp
Organ	Breast (CL)	0.49%	0.52%	0.56%	0.52%	0.54%	0.57%	0.60%	0.83%	0.84%	0.84%	0.84%
	Eye (IL)	0.09%	0.09%	0.10%	0.09%	0.10%	0.11%	0.12%	0.19%	0.19%	0.19%	0.19%
	Eye Lens (IL)	0.12%	0.13%	0.15%	0.13%	0.15%	0.16%	0.17%	0.29%	0.29%	0.29%	0.29%
	Heart	0.01%	0.03%/0.01%	0.06%/0.03%	0.03%/0.01%	0.04%/0.02%	0.07%/0.03%	0.10%/0.05%	0.29%/0.14%	0.28%/0.13%	0.28%/0.13%	0.28%/0.13%
	Liver	0.01%	0.00%/0.02%	0.01%/0.03%	0.00%/0.02%	0.00%/0.02%	0.01%/0.04%	0.01%/0.05%	0.03%/0.14%	0.03%/0.14%	0.03%/0.14%	0.03%/0.14%
	Lung (IL)	0.02%	0.04%	0.08%	0.03%	0.05%	0.09%	0.14%	0.45%	0.45%	0.44%	0.44%
	Pectoralis Muscle (IL)	23.63%	25.88%	27.77%	26.31%	28.21%	29.46%	30.54%	41.76%	42.19%	42.44%	42.46%
	Stomach	0.03%/0.00%	0.04%/0.00%	0.06%/0.01%	0.04%/0.00%	0.05%/0.00%	0.07%/0.01%	0.09%/0.01%	0.23%/0.02%	0.23%/0.02%	0.23%/0.02%	0.23%/0.02%
	Thymus	0.01%	0.02%	0.06%	0.02%	0.03%	0.06%	0.09%	0.28%	0.28%	0.27%	0.27%
	Uterus or Fetus	0.000021%	0.000102%	0.000375%	0.000051%	0.000125%	0.000343%	0.000763%	0.0023%	0.0021%	0.0021%	0.0020%
Bone Marrow	Arm Bone (upper section, IL)	0.00%	0.00%	0.01%	0.00%	0.00%	0.01%	0.02%	0.06%	0.06%	0.06%	0.05%
	Clavicle (IL)	0.02%	0.03%	0.05%	0.03%	0.04%	0.05%	0.08%	0.22%	0.22%	0.21%	0.21%
	Rib Cage	0.11%	0.13%	0.16%	0.13%	0.15%	0.18%	0.21%	0.42%	0.42%	0.42%	0.42%
	Sternum	0.15%	0.17%	0.21%	0.17%	0.19%	0.22%	0.26%	0.51%	0.51%	0.51%	0.51%
Bone Surface	Arm Bone (middle section, IL)	0.00%	0.00%	0.01%	0.00%	0.00%	0.01%	0.02%	0.06%	0.05%	0.05%	0.05%
	Arm Bone (upper section, IL)	0.00%	0.01%	0.04%	0.01%	0.02%	0.04%	0.08%	0.25%	0.24%	0.23%	0.23%
	Clavicle (IL)	0.08%	0.13%	0.22%	0.11%	0.16%	0.23%	0.35%	0.92%	0.91%	0.90%	0.89%
	Clavicle (CL)	0.04%	0.04%	0.05%	0.04%	0.05%	0.06%	0.07%	0.12%	0.12%	0.12%	0.12%
	Facial Skeleton	0.03%	0.04%	0.06%	0.04%	0.05%	0.06%	0.08%	0.18%	0.18%	0.18%	0.18%
	Ribs	0.46%	0.55%	0.69%	0.55%	0.63%	0.74%	0.87%	1.75%	1.77%	1.77%	1.76%
	Sternum	0.61%	0.72%	0.89%	0.71%	0.81%	0.94%	1.10%	2.15%	2.16%	2.16%	2.15%
Skin	Breast (IL)	184.61%	165.34%	153.62%	163.86%	149.27%	141.99%	137.08%	93.23%	91.56%	90.50%	90.36%
	Breast (CL)	2.26%	2.08%	1.98%	2.06%	1.93%	1.87%	1.84%	1.54%	1.52%	1.51%	1.51%
	Head	0.18%	0.17%	0.16%	0.17%	0.16%	0.15%	0.15%	0.14%	0.14%	0.14%	0.14%
	Neck	0.13%	0.11%	0.10%	0.11%	0.10%	0.09%	0.09%	0.08%	0.08%	0.08%	0.08%
	Trunk	0.81%	0.75%	0.72%	0.74%	0.70%	0.68%	0.67%	0.59%	0.58%	0.58%	0.58%

and were not included. For most volumes the ROD was found to remain constant after varying which breast was imaged. For these volumes the mean ROD is reported. For the volumes for which a different ROD was found depending on which breast was imaged, both values are shown.

Using the computed ROD, an example calculation of the total doses to the organs, bones and skin sections resulting from a single-breast two-view tomosynthesis acquisition was computed. For this example, it was assumed that the CC view tomosynthesis acquisition results in a glandular dose to the imaged breast of 2 mGy, while the MLO view tomosynthesis acquisition results in a glandular dose of 2.5 mGy. The resulting doses are shown in Table 3.5.

With the lead shield present, the ROD of the organs that received the highest dose was not lowered substantially. The contralateral breast in the CC view, and the heart, the ipsilateral lung, the stomach and the thymus in both views were minimally protected by the shield. The dose to the contralateral breast in the MLO view was reduced to a third of the dose without the shield, while the dose to the ipsilateral eye and eye lens in both views were almost completely eliminated. The dose to the uterus was reduced by approximately a factor of two by the presence of the shield. Of the bones, the contralateral clavicle, the cranium and the facial skeleton were well protected, while the dose to the ipsilateral clavicle, the rib cage and the sternum was somewhat reduced.

The results for planar mammography were found to be very similar to the ones presented here for tomosynthesis imaging for both views and all spectra studied, with only small variations in some of the volumes studied. Therefore, although the results will not be included, all the conclusions discussed here are applicable to both imaging methodologies.

Table 3.5 Example computation of the total dose to the organs in µGy resulting from a two-view tomosynthesis acquisition to one (left/right) breast, assuming 2 mGy glandular dose to the imaged breast for the CC view and 2.5 mGy glandular dose to the imaged breast for the MLO view, and using the data from Table 3.3 and Table 3.4.

Tissue Type	Volume	Mo/Mo			Mo/Rh				Rh/Rh			
		25 kVp	30 kVp	35 kVp	25 kVp	30 kVp	35 kVp	40 kVp	25 kVp	30 kVp	35 kVp	40 kVp
Organ	Breast (CL)	20.98	22.22	23.71	22.24	23.24	24.34	25.63	35.22	35.44	35.54	35.48
	Eye (IL)	3.68	3.87	4.15	3.85	4.02	4.23	4.55	6.37	6.40	6.42	6.40
	Eye Lens (IL)	4.89	5.30	5.75	5.34	5.53	6.02	6.35	9.31	9.41	9.42	9.39
	Heart	0.49	1.51/0.81	3.15/1.65	1.24/0.67	1.89/1.00	3.19/1.67	5.21/2.75	15.17/7.83	14.99/7.70	14.84/7.60	14.66/7.50
	Liver	0.30	0.11/0.52	0.21/0.97	0.09/0.46	0.13/0.65	0.21/1.00	0.35/1.56	0.96/4.30	0.94/4.25	0.93/4.21	0.92/4.16
	Lung (IL)	0.66	1.57/1.85	3.62/4.18	1.21	2.03	3.85	6.09/6.96	18.61/21.26	18.46/21.14	18.32/21.00	18.10/20.75
	Pectoralis Muscle (IL)	590.65	646.99	694.31	657.70	705.13	736.53	763.39	1043.90	1054.64	1061.04	1061.40
	Stomach	0.64/0.05	0.99/0.08	1.61/0.16	0.95/0.07	1.26/0.10	1.74/0.16	2.41/0.27	6.33/0.72	6.33/0.70	6.32/0.69	6.27/0.68
	Thymus	0.58	1.36	3.13	1.05	1.75	3.15	5.32	16.09	15.90	15.75	15.55
	Uterus or Fetus	0.00052	0.0026	0.010	0.0013	0.0032	0.0088	0.020	0.058	0.055	0.053	0.052
Bone Marrow	Arm Bone (upper section, IL)	0.65	0.83	1.21	0.78	0.94	1.24	1.72	3.95	3.89	3.85	3.80
	Clavicle (IL)	1.39	1.90	2.89	1.79	2.24	3.01	4.17	10.17	10.09	10.02	9.92
	Rib Cage	4.27	5.29	6.80	5.24	6.15	7.28	8.68	18.37	18.52	18.58	18.50
	Sternum	10.15	11.96	14.58	11.88	13.46	15.42	17.90	34.51	34.72	34.80	34.64
Bone Surface	Arm Bone (middle section, IL)	1.63	2.06	2.87	1.97	2.34	2.97	3.99	8.84	8.71	8.62	8.53
	Arm Bone (upper section, IL)	2.72	3.50	5.10	3.28	3.96	5.21	7.23	16.65	16.38	16.20	16.02
	Clavicle (IL)	5.85	8.01	12.19	7.52	9.42	12.66	17.56	42.83	42.49	42.19	41.77
	Clavicle (CL)	2.04	2.44	3.05	2.42	2.77	3.22	3.88	7.62	7.61	7.59	7.54
	Facial Skeleton	1.02	1.33	1.86	1.29	1.56	1.97	2.54	5.81	5.80	5.79	5.74
	Ribs	17.96	22.29	28.64	22.08	25.89	30.64	36.56	77.34	77.99	78.25	77.88
	Sternum	42.76	50.36	61.38	50.02	56.68	64.92	75.38	145.32	146.20	146.51	145.83
Skin	Breast (IL)	9716.07	8692.97	8076.14	8614.25	7841.47	7457.59	7202.77	4899.26	4811.90	4755.80	4748.58
	Breast (CL)	100.32	92.74	88.68	92.03	86.41	83.91	82.77	70.07	69.46	69.05	68.93
	Head	15.00	13.50	12.65	13.38	12.24	11.74	11.46	8.91	8.80	8.73	8.72
	Neck	6.76	5.93	5.51	5.86	5.24	5.01	4.94	3.99	3.91	3.87	3.85
	Trunk	32.22	29.86	28.68	29.63	27.89	27.21	26.93	23.69	23.52	23.41	23.37

Discussion

As can be seen from the results, all organs outside the x-ray field receive less than 0.9% of the glandular dose received by the imaged breast. Except for the contralateral breast, the organ that absorbs the most dose from a tomosynthesis or a mammogram acquisition is the ipsilateral lung, with a maximum ROD of 0.46%. Considering the x-ray spectrum that results in the maximum dose deposition to the lungs (Rh/Rh 25 kVp), the dose deposited in the lungs during a complete two-view bilateral breast tomosynthesis study is approximately 18.6 μGy. This is equivalent to approximately one tenth of the dose to the lungs from a chest x-ray (International Commission on Radiological Protection 1982), and one hundredth to one thousandth of the dose to the lungs from a single chest CT scan (Huda et al 2000; McWilliams et al 2005). In case of the red bone marrow, the maximum ROD found was 1.1%, while the maximum ROD for the bone surfaces was 4.6%. The results for both the bone marrow and the bone surfaces can be taken as a conservative upper limit, since at these energy levels it has been found that the methods used in this study tend to overestimate the dose (Lee et al 2006). Therefore, it seems that in both planar and tomosynthesis breast imaging, the dose to the organs and skeleton outside the x-ray field are minimal, if not negligible.

As expected, compared to the glandular dose, the skin of the imaged breast receives a much higher dose, which becomes lower with increasing x-ray spectrum energy. If only the portion of the breast skin facing the x-ray tube is considered, its local dose can be approximated to be double that specified for the whole breast skin. The dose to the skin of the contralateral breast (1.5%-2.2%) can normally be ignored since that same skin will receive the full dose when the contralateral breast is being imaged.

In this study it was found that the dose to the uterus due to an average two-view bilateral tomosynthesis study is at most only 0.058 μGy (0.0058 mrad) per imaged breast. This result can be representative of the dose to the fetus during the first trimester, when the volume of the uterus as simulated in this study is still representative of that of a pregnant woman and the conceptus is very small. This amount of dose to the fetus is approximately 60 to 380 times lower than that received by the fetus from a helical chest CT scan of a pregnant patient (Winer-Muram et al 2002). Even though the dose to the fetus from breast imaging can be considered to be minimal, the use of a lead shield seems to reduce this dose further by about a factor of two. Therefore, if a patient underwent either a planar mammogram or a tomosynthesis study not knowing that she was in the early stages of pregnancy, these findings suggest that the dose to the fetus is minimal. If, however, a patient is known to be pregnant and a breast must be imaged, a lead apron can lower this low amount of dose to the fetus by approximately one half.

The shield results show that most of the dose to the organs is a consequence of x-rays that scatter in the breast tissue and enter the trunk through the breast, minimizing the benefit of using a lead shield or apron under normal circumstances.

Using the results from this study, the effective dose (to the whole body) for a complete tomosynthesis examination (two views, both breasts) per unit glandular dose to both breasts was computed. Using the current recommended tissue weighting factors based on ICRP Publication 60 (International Commission on Radiological Protection 1991) the value found was 0.0521 mSv/mGy (or mrem/mrad), while using the tissue weighting factors from the draft of the new ICRP recommendations posted on the ICRP website on January 12, 2007 (International Commission on Radiological Protection 2007), the value was 0.124 mSv/mGy (or mrem/mrad). These values vary by a maximum of 0.84% for the eleven spectra used in this study. The value for the effective dose in planar mammography using the ICRP Publication 60 recommendations was

found to be approximately within 2.5% of that reported by Hatziioannou et al (Hatziioannou et al 2000).

The results in this study depend on the applicability of the mathematical phantom as representative of the human body. Although this phantom is used extensively for dosimetry in radiology, its simplification of the shapes of the organs of the human body has the potential of introducing severe errors in the results, particularly with patients with body habitus that greatly deviates from the assumed shape of the phantom. However, a recent study by Castellano et al (Castellano et al 2005), comparing the dose estimations of the Cristy phantom to a voxel based phantom from CT acquisitions has found the disagreements between the two phantoms to be less than 38%, and within 15% if the imaged sections of the phantoms are matched appropriately. Although these deviations are considerable, the importance or lack thereof of the dose to the different organs from breast tomosynthesis found in this study is still applicable since an increase in ROD by 40% would still result in maxima of 0.64% (ipsilateral lung), 1.53% (sternum bone marrow) and 6.45% (sternum bone surface). The effective dose computations, even with the additional 40% in the dose to all the organs except the imaged breast, is still valid, since the breast accounts for over 95% of the effective dose.

Two sources of radiation were not taken into account in this study: x-ray leakage from the shielded portions of the x-ray tube, and the fraction of x-rays from the primary field that are transmitted through the imager support arm. According to the Code of Federal Regulations (21CFR1020.31), the x-ray leakage in a mammography system must be limited to a maximum air kerma of 0.88 mGy (100 mR exposure) per hour. Approximating a bilateral two-view tomosynthesis acquisition to entail ten seconds of x-ray exposure (Eberhard et al 2006), the air kerma at 1 m from the focal spot from leakage radiation must be less than 2.5 μGy (0.278 mR exposure). The same chapter limits the radiation transmitted through the imager support arm to 0.88 μGy air kerma

(0.1 mR exposure) 5 cm under the support arm per acquisition. Therefore, the radiation from tube leakage and primary barrier transmission is well within the uncertainty level of this study.

Conclusion

An advanced computer program based on Monte Carlo methods was used to simulate the radiation dose received by the organs and tissues of the human body during both planar mammography and breast tomosynthesis imaging. By measuring the dose to the uterus, an estimate of the radiation dose to a first trimester fetus during breast imaging was also found. The results showed that introducing breast tomosynthesis as a tomographic imaging method for breast cancer detection does not result in increased dose to the rest of the body. Therefore, if the maximum glandular dose to the breast used during tomosynthesis imaging is limited to that used in standard planar mammography, then the effective dose to the body from tomosynthesis will also be equivalent to that from planar mammography. The next chapter will investigate if another method of tomographic imaging of the breast, dedicated breast computed tomography, also maintains the effective dose to the body for equivalent glandular dose to the breast conditions.

During both planar and tomosynthesis breast imaging, the dose to the fetus was found to be minimal. For increased security, the use of a lead shield was found to decrease this minimal dose by approximately a factor of two. Therefore, in the event that a woman in the early stages of pregnancy needs to undergo breast imaging, the use of standard mammography or breast tomosynthesis imaging is possible, and the use of a lead apron is advised.

CHAPTER 4

WHOLE BODY DOSIMETRY IN DEDICATED BREAST COMPUTED TOMOGRAPHY

Introduction

Dedicated breast computed tomography has been the subject of several studies in the last few years (Boone et al 2001; Chen et al 2002; Glick et al 2002; Chen et al 2003; Boone 2004; Boone et al 2004; Gong et al 2004; Thacker et al 2004; Kwan et al 2005). DBCT aims at acquiring a high number (350-500) of cone beam projections of the breast from at least a full revolution around it, resulting in a 3D reconstruction of the breast volume (Boone et al 2001; Ning et al 2002; Ning et al 2004; Zeng et al 2006). DBCT's ability to fully reconstruct the 3D volume of the imaged breast presents a very interesting alternative to tomosynthesis imaging, which only achieves partial vertical separation of the imaged tissue. However, since the breast is uncompressed during DBCT acquisition, to maintain the dose to the breast comparable to the dose to the breast from a two-view planar mammography acquisition, the proposed x-ray spectra in DBCT projection acquisition are of considerably higher energy than that of planar mammography and tomosynthesis imaging (McKinley et al 2004; McKinley et al 2005; Huang et al 2006). Preliminary DBCT imaging studies are typically performed with tungsten targets with kVp settings in the 70-80 kVp range.

Several studies on the glandular dose to the breast from these high energy x-ray spectra in DBCT have been reported (Boone et al 2001; Chen et al 2002; Boone et al 2004; Thacker et al 2004; Boone et al 2005; Sechopoulos et al 2006), but the effect that these higher energies have on the dose to the organs outside the x-ray field has not been investigated. If DBCT is to be introduced in the clinical environment, as either an alternative to planar mammography or tomosynthesis imaging for screening for breast

cancer, or as an adjunct for a subset of patients (high-risk groups, diagnostic stage, etc.), the radiation dose to the organs and tissues of the body from DBCT acquisition must be well understood. In addition, the dose to the fetus must be studied and compared to that in planar mammography and tomosynthesis imaging of the breast.

In this study, the Monte Carlo program used in the previous chapter was modified to compute the radiation dose deposited in the important organs and tissues of the body during DBCT acquisition. To accomplish this, the geometrical description of both breasts, and the positioning of the x-ray source and detector had to be modified to recreate the geometry and conditions present during a DBCT acquisition. The modified program was then used to compute the dose to the 65 volumes, representing organs, bones, skin sections, and other soft tissues present in the anthropomorphic phantom.

Methods

Monte Carlo simulation modifications

The x-ray source, approximated as a point source, was placed 86 cm away from the detector surface, which was located 40 cm from the iso-center of the imaged breast (Boone et al 2005). With varying projection angle, both the x-ray source and the detector were rotated about the isocenter of the breast, maintaining constant both the source-to-imager distance and the breast isocenter-to-imager distance (IID) throughout the DBCT acquisition. In Figure 4.1(b) the movement of the x-ray source and detector with projection angle around the imaged breast can be seen. Since there is no breast compression used in DBCT, the breast compression and support plates were removed from the simulation. The detector cover plate, which can be seen in Figure 4.1(a), was maintained.

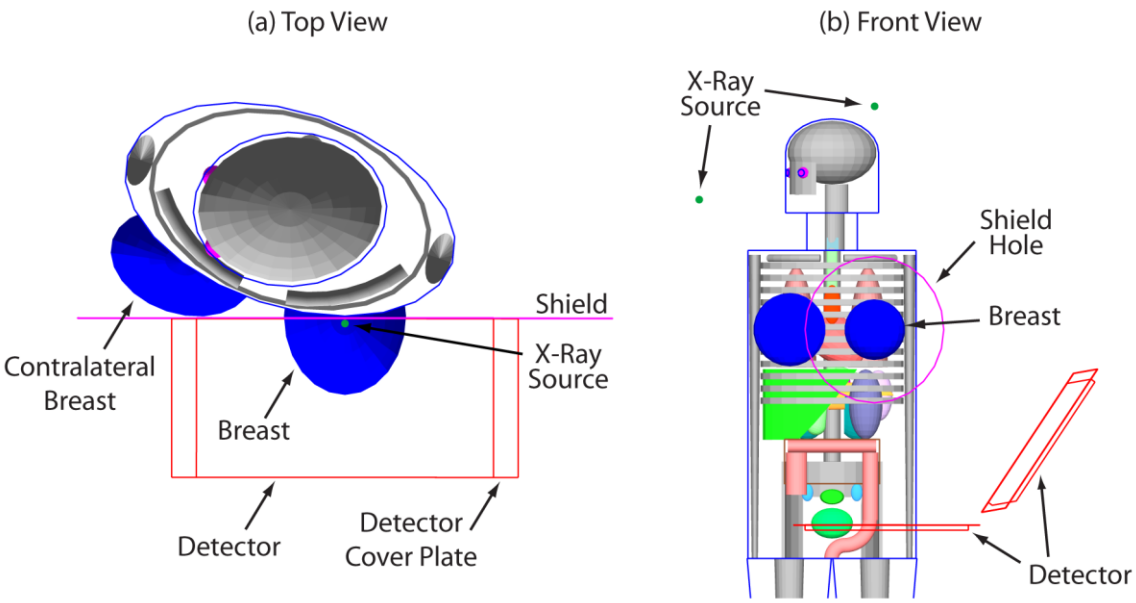

Figure 4.1(a) Top view and (b) front view of the DBCT simulation.

The simulation was performed for 40 million monochromatic x-rays of energies varying from 17 keV to 80 keV in 1 keV steps, interpolating these results to 0.5 keV resolution, and then combining these monochromatic results with the relative number of photons in each spectrum as reported by Cranley et al (Cranley et al 1997). The x-ray spectra used consisted of a Tungsten target, with 0.5 mm Beryllium window and 0.3 mm Copper added filtration, with kVp settings of 60 kVp, 70 kVp and 80 kVp. Their first half-value layers were 4.29 mm Al, 5.04 mm Al, and 5.81 mm Al, respectively. After simulating all 64 energies, the x-ray source and detector were rotated around the isocenter of the breast by 10 degrees, and the process was repeated. Simulations were performed from a total of 35 positions, covering an entire revolution around the imaged breast. The results from these 35 positions were later interpolated and summed to obtain dose results from the equivalent of 500 projections from an entire 360º revolution (Boone et al 2005). Due to the asymmetric location of some organs of the body, all simulations were performed for both breasts. This resulted in a total of 4,480 simulations of 40 million x-rays each.

The methodologies used in the previous chapter to compute the glandular dose to the breast and to separate the dose to the red bone marrow and bone surface portions of the skeleton were used for this study as well

Anthropomorphic phantom modifications

Slight modifications had to be introduced in the anthropomorphic phantom to better recreate the geometry during DBCT imaging. The DBCT acquisition geometry simulated consisted of the patient laying prone on a table with the imaged breast hanging through a hole (Boone et al 2006). Therefore, the breasts were implemented as portions of ellipsoids of equal volume but different shape. The imaged breast was implemented to reflect a pendant breast, having a longer CND and smaller diameter along the chest wall than the contralateral breast. The latter was implemented as slightly compressed by the body against the table (Figure 4.1). The head and neck of the phantom were rotated towards the contralateral side, as shown in Figure 2 of Boone et al (Boone et al 2006). The imaged breast was specified as having a diameter at the chest wall of 12.4 cm and a CND of 8 cm. The contralateral breast had a diameter at the chest wall of 15.0 cm and a CND of 5.2 cm. The composition of the breasts was again specified as a homogeneous mixture of 50% adipose and 50% glandular tissue, as reported by Hammerstein et al (Hammerstein et al 1979).

The organs, bones, skin sections and other volumes included in the anthropomorphic phantom were the same as those used in the previous chapter. Given the higher energy x-rays used in DBCT, the simulated lead shield was specified as 1 mm thick, resulting in an absorption of approximately 94% of 80 keV x-rays and more than 98% of x-rays of energy of 70 keV or less. The shield was large enough to cover the whole body and included a 30 cm diameter gantry opening.

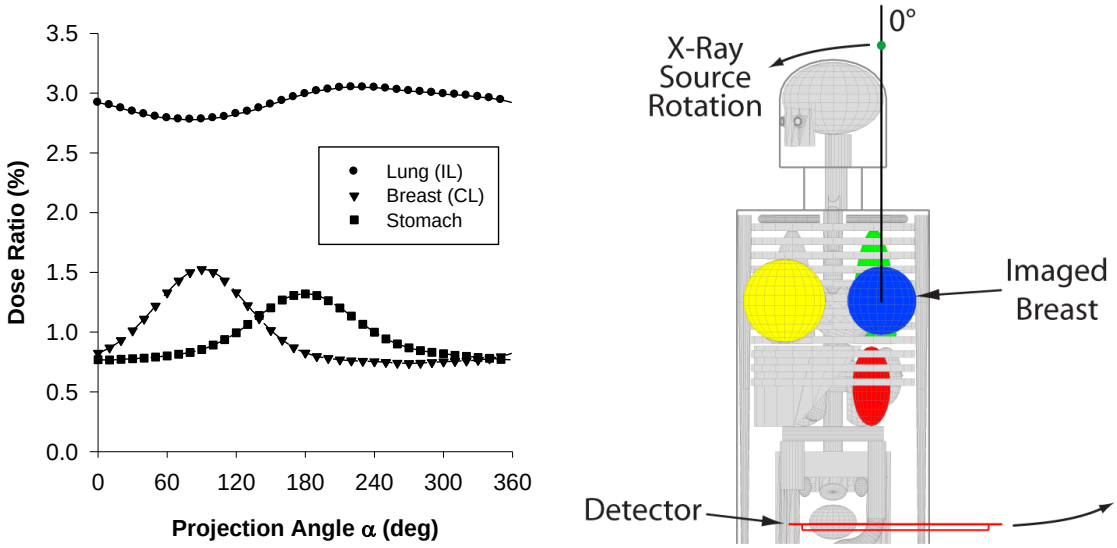

Figure 4.2 Variation of dose deposition in different organs with projection angle during a DBCT imaging of the left breast (blue). The organs highlighted in color are the ones included in the graph.

Results

Figure 4.2 shows an example graph of the dose ratio variation with projection angle for three different organs, along with the anthropomorphic phantom highlighting the organs included in the graph and the imaged breast (blue). Both the actual simulation results (symbols) and the results of the interpolation to 500 projections (lines) are shown. As expected, the variation with projection angle (0º is defined as when the x-ray source is exactly above the breast, and the x-ray source rotates counter-clockwise facing the patient with increasing angle) is different for different organs, due to the position of the organs with respect to the x-ray source. The distributions chosen for this example graph are representative of those found for the rest of the organs. The suitability of the angular interpolation can also be clearly seen.

Table 4.1 shows the dose to the organs per unit glandular dose to the imaged breast (ROD), in percentages. Only the organs that received more than 0.1% of the

glandular dose to the breast in at least one spectrum and the uterus are included. In the cases were the ROD was found to be equivalent for both the left and right imaged breasts, the ROD is shown. When the ROD varied between imaged breasts, both values are included.

The effective dose per unit glandular dose to the breast averaged for the three spectra studied was found to be 0.0574 mSv/mGy (mrem/mrad). With the revised tissue weighting factors, this values increases to 0.128 mSv/mGy (mrem/mrad). The maximum deviation from the mean was 1.9% and 0.9%, respectively.

The inclusion of the lead shield had an even smaller effect than that found in the previous chapter for planar and tomosynthesis imaging. Only the skin of the head, the ipsilateral lower section of the arm bone, the cranium and the facial skeleton were considerably protected. All other organs received doses similar to those received without the shield present. Although the uterus received a relatively low dose without the lead shield present, this amount of dose was lowered by approximately a factor of four.

Discussion

The higher energy spectra used in DBCT imaging result in higher dose to the organs and tissues of the body compared to those resulting from planar mammography and tomosynthesis imaging. For the 80 kVp spectra, the heart, ipsilateral lung and thymus receive a dose of approximately 100-150 μGy from a DBCT acquisition that deposits 5 mGy in the imaged breast. This dose level for the lungs is comparable to that of a single projection chest x-ray (International Commission on Radiological Protection 1982), but one or two orders of magnitude less than that of a chest CT scan (Huda et al 2000; McWilliams et al 2005). By comparison, these organs received approximately one order of magnitude more dose than that from a planar mammogram or a tomosynthesis

Table 4.1 Relative organ dose found from DBCT imaging to the (left/right) breast.

Tissue Type	Volume	60 kVp	70 kVp	80 kVp
Organ	Adrenal (IL)	0.16%/0.23%	0.23%/0.31%	0.29%/0.39%
	Adrenal (CL)	0.05%/0.06%	0.08%/0.10%	0.11%/0.13%
	Breast (CL)	0.83%	0.91%	0.97%
	Colon (transverse)	0.06%	0.08%	0.10%
	Esophagus	0.34%/0.27%	0.46%/0.37%	0.57%/0.46%
	Gall Bladder	0.11%/0.20%	0.15%/0.27%	0.19%/0.34%
	Heart	2.32%/1.11%	2.74%/1.37%	3.08%/1.58%
	Kidney (IL)	0.06%	0.09%	0.12%
	Liver	0.15%/0.63%	0.20%/0.79%	0.24%/0.92%
	Lung (IL)	2.29%/2.57%	2.65%/2.95%	2.93%/3.25%
	Lung (CL)	0.19%/0.16%	0.26%/0.22%	0.32%/0.28%
	Pancreas	0.29%/0.13%	0.40%/0.19%	0.50%/0.25%
	Spleen	0.27%/0.03%	0.36%/0.05%	0.44%/0.07%
	Stomach	0.66%/0.11%	0.82%/0.14%	0.95%/0.18%
	Thymus	1.72%	2.07%	2.35%
	Thyroid	0.12%	0.15%	0.19%
	Uterus/Fetus	0.015%	0.021%	0.026%
Bone Marrow	Arm Bone (middle section, IL)	0.33%	0.43%	0.52%
	Arm Bone (upper section, IL)	0.29%	0.38%	0.46%
	Clavicle (IL)	0.56%	0.69%	0.81%
	Clavicle (CL)	0.09%	0.12%	0.15%
	Rib Cage	1.28%	1.45%	1.59%
	Scapulae (IL)	0.08%	0.12%	0.15%
	Spine (trunk section)	0.06%/0.07%	0.09%/0.10%	0.12%/0.14%
	Sternum	1.69%	1.99%	2.24%
Bone Surface	Arm Bone (lower section, IL)	0.14%	0.17%	0.20%
	Arm Bone (middle section, IL)	1.22%	1.50%	1.72%
	Arm Bone (upper section, IL)	1.07%	1.30%	1.49%
	Clavicle (IL)	2.11%	2.50%	2.80%
	Clavicle (CL)	0.34%	0.42%	0.50%
	Cranium	0.09%	0.10%	0.11%
	Facial Skeleton	0.10%	0.12%	0.13%
	Rib Cage	4.86%	5.30%	5.56%
	Scapulae (IL)	0.32%	0.43%	0.52%
	Spine (head section)	0.07%	0.10%	0.13%
	Spine (neck section)	0.12%	0.18%	0.23%
	Spine (trunk section)	0.21%/0.25%	0.31%/0.37%	0.41%/0.48%
	Sternum	6.37%	7.18%	7.74%
Skin	Breast (IL)	114.00%	111.35%	109.63%
	Breast (CL)	1.17%	1.23%	1.27%
	Head	0.10%	0.11%	0.11%
	Neck	0.10%	0.12%	0.14%
	Trunk	0.61%	0.65%	0.67%

study. The highest doses to the skeletal tissues are that of the ribs and sternum, which receive approximately 50 μGy to 100 μGy to the red bone marrow and approximately 250 μGy to 400 μGy to the bone surface from a similar DBCT study, which is approximately three to four times more dose than that resulting from the other breast imaging methods. It is again important to note that the dose to the bone tissues are upper limit estimates, due to the known overestimation of the dose to the bone tissues by the methodology used in these studies.

The dose to the uterus, representative of that to the fetus in the first trimester, was found to be low, in the range of 0.7 μGy to 1.3 μGy from a 5 mGy DBCT acquisition, depending on the x-ray spectrum used. Although there is a wide variability in estimates of detrimental biological effects or increase of risk to the fetus from different levels of x-ray radiation, all studies seem to suggest that biological effects to the fetus or increase in risk of damage to the fetus is possible at several orders of magnitude above the levels found in this study (Wagner et al 1997).

Even though these radiation levels to the fetus are comparable to the natural background radiation, it was found that the presence of the 1 mm lead shield decreased these levels substantially, introducing the possibility of lowering the dose to the fetus further. Aside from the protection to the uterus, which is of utmost importance, the presence of the lead shield did not contribute substantially to the protection of the body; again pointing to the fact that most x-rays that deposit dose in the tissues of the body scatter through the breast into the trunk. It is important to note, though, that the proposed geometry of DBCT acquisition lends itself well to the introduction of a thin lead shield, given the presence of the table on which the patient is to lie prone.

The computation of the effective dose during DBCT imaging shows that the dose to the organs outside the x-ray field, though low, is not negligible. Using the current recommended tissue factors the dose to the other organs increase the effective dose by

13% to 17%. Using the proposed draft factors, due to the increased radiosensitivity assigned to the breast, the importance of the dose to the other organs decreases, with a contribution of approximately 6% to 8%.

Conclusion

The Monte Carlo program implemented in the previous chapter was modified to simulate the conditions present in a different tomographic breast imaging method, dedicated breast computed tomography. Since DBCT involves the use of higher energy x-rays than those used in tomosynthesis imaging, the effect that these x-rays have on the dose to the tissues of the body outside the x-ray field was of concern. As expected, the dose to the organs closest to the imaged breast, namely the ipsilateral lung, thymus, and heart among others do receive a considerably higher dose, with up to an order of magnitude increase. These levels of radiation though, are still very low compared to other radiographic studies, such as chest computed tomography, and therefore the limiting factor in DBCT imaging is the glandular dose to the imaged breast, not the dose to the organs outside the x-ray field.

CHAPTER 5

CHARACTERIZATION OF X-RAY SCATTER IN TOMOSYNTHESIS

Introduction

In one of the variations of digital tomosynthesis imaging of the breast, the x-ray tube rotates through a limited angular range around the compressed breast, while the breast and the digital imager remain stationary (Wu et al 2003; Eberhard et al 2006). The movement of the x-ray tube with respect to the digital imager during acquisition of the tomosynthesis projections makes the use of an anti-scatter grid challenging. With the use of a traditional linear or cellular anti-scatter grid, the primary (non-scattered) x-rays incident on the imager for the oblique views would be cut off. At a tomosynthesis projection angle of 10°, approximately 65% and 88% of the primary x-rays would be cut off at the center of the detector by anti-scatter grids with grid ratios of 4:1 and 5:1 (Rezentes et al 1999), while at 15° and 11°, respectively, all primary x-rays would be cut off. A focused linear anti-scatter grid with the septa oriented parallel to the chest wall could be used if the motion mechanism of the grid is also re-oriented. Other options to make anti-scatter grids suitable in tomosynthesis imaging are to have a low grid ratio with inefficient scatter rejection or to rotate the septa of the grid with the x-ray tube to maintain their parallelism with the incident x-rays for all projections. All these variations would still suffer from the limitation that anti-scatter grids do not absorb all incident scattered x-rays and do not transmit all incident primary x-rays (Kaufhold et al 2002), and therefore other methods for scatter rejection are being sought.

A different approach that is being investigated for the reduction of x-ray scatter content in the projections is to introduce post-acquisition, software-based scatter reduction (Seibert et al 1988; Baydush et al 2000; Gonzalez Trotter et al 2002; Nykanen

et al 2003; Sechopoulos et al 2005). Several scatter reduction algorithms have been proposed for planar mammography and could be potentially adapted for digital tomosynthesis.

Another alternative to reduce the effect of x-ray scatter in tomosynthesis imaging is the introduction of an x-ray scatter model in the reconstruction stage. With iterative reconstruction techniques where simulated projections of the estimated reconstructed volume are compared to the acquired projections to adjust the estimated volume, the effect of x-ray scatter can be added to the simulated projections before comparison with the acquired projections. This method is used in the reconstruction algorithm implemented in Chapter 7.

Both of the alternative approaches for x-ray scatter reduction mentioned above, however, require some form of prior knowledge of the scatter content in the projections to be processed. This prior knowledge includes the scatter point spread function (PSF) or the scatter to primary ratio (SPR). The purpose of this study is to characterize x-ray scatter in digital tomosynthesis of the breast to facilitate the further development and application of these approaches. Extensive studies based on experimental and simulation methods have been published on x-ray scatter in planar mammography (Barnes et al 1978; Fritz et al 1983; Klein et al 1983; Dance et al 1984; Boone et al 2000a; Boone et al 2000b; Cooper et al 2000; Nykanen et al 2003) and some work has been done on characterizing x-ray scatter in breast CT (Kwan et al 2005). Although limited studies of x-ray scatter in breast tomosynthesis have been presented (Liu et al 2005; Sechopoulos et al 2005; Karellas 2006; Liu et al 2006), no comprehensive characterization of the x-ray scatter in tomosynthesis projections of clinically realistic mammographic shapes has been reported. In this work, the variation of x-ray scatter content in the tomosynthesis projections under different conditions such as varying breast size, compressed thickness, composition, x-ray spectrum, and tomosynthesis

projection angle is studied. Computer fit equations for the SPR at the center of mass, as well as insights into the variations in scatter PSF with varying projection angle are reported.

Methods

A modified version of the C++ program described in Chapter 2 was used for this study. The detector was modified so that it can discriminate between primary (x-rays that did not undergo any scatter event) and scatter (x-rays that underwent at least one scatter event) photons. This results in two separate images being recorded per acquisition, one primary and one scatter image. The simulated detector was programmed to have a 1 mm resolution, which was deemed small enough for appropriate characterization of x-ray scatter variation with position, but still large enough to obtain reasonable statistics. This resulted in SPR maps of size 240 x 307.

Characterization of Scatter to Primary Ratio

To analyze how the SPR varies under different conditions, the Monte Carlo simulation was performed repeatedly while varying breast size, specified as the chest wall to nipple distance and compressed breast thickness, for both CC and MLO views. Simulations were performed for the compressed breast using a 50% glandular fraction, as described by Hammerstein et al (Hammerstein et al 1979), with the CND and T set to the values specified in Table 5.1. For the compressed breast in CC view, the CND was chosen so that the breast tissue mass would be equal to that of the MLO simulations, not including the pectoralis muscle. To study the behavior of SPR with glandular fraction, additional simulations were performed by setting the glandular fraction to 0, 25, 50, 75

Table 5.1 Values of the geometric parameters used in the Monte Carlo simulations for the scatter to primary ratio studies.

Parameter	CC View	MLO View
Breast Size Studies		
Chest-wall to Nipple Distance (CND)	6.2, 9.0, 11.6, 14.4 and 17.0 cm	7, 10, 13, 16 and 19 cm
Thickness (T)	2, 4, 5, 6 and 8 cm	
Glandularity (G)	50%	
Breast Composition Studies		
Chest-wall to Nipple Distance (CND)	11.6 cm	13 cm
Thickness (T)	2, 5 and 8 cm	
Glandularity (G)	0, 25, 50, 75 and 100 %	

and 100% for the more limited set of parameter values shown in the second part of Table 5.1.

For each breast setup, projections were acquired at ±30° in 6° steps (due to symmetry, only the positive angles were used for the CC view studies). For each of these 518 geometry and composition combinations, 50 million monochromatic x-rays at each energy between 9.5 and 31.5 keV in steps of 1 keV were tracked. This resulted in a total of 11,914 sets of primary and scatter images. To perform these simulations, the same computer cluster as that used in the previous chapters was utilized. To obtain SPR maps for a specified x-ray spectrum, the monochromatic primary and scatter images were median filtered (11 x 11 kernel size) to reduce noise, weighted by the relative number of photons at each energy bin of the spectrum, and then totaled to obtain spectrum-weighted primary and scatter images. A median filter, rather than a mean filter, was used because it was found by analyzing pre- and post-filter profiles of the data that although the noise reduction was similar, the median filter preserved the sharp features present in the primary images better than the mean filter. The spectrum-weighted spatially-variant SPR maps were obtained by pixel-by-pixel division of the spectrum-weighted scatter image by the spectrum-weighted primary image. To study how the x-

Table 5.2 X-ray spectra used in this study and their first half-value layer values.

Target	Filter	Tube Potential (kVp)	HVL above Compression Plate (mm Al)	HVL under Compression Plate (mm Al)
Mo	Mo	25	0.284	0.322
Mo	Mo	26	0.297	0.335
Mo	Mo	27	0.309	0.347
Mo	Rh	27	0.364	0.400
Mo	Rh	29	0.387	0.422
Rh	Rh	29	0.380	0.426
Rh	Rh	31	0.408	0.457

ray spectrum affects the SPR, the monochromatic data were combined using the relative number of photons for seven different spectra (Boone et al 1997), specified in Table 5.2. From these simulations, the SPR at the projection of the center of mass (COM) of the breast was found and its variation under the different imaging conditions characterized. The SPR at the center of mass reported is the mean from a 1 x 1 cm region surrounding the COM. In addition, SPR maps and profiles are presented for qualitative analysis.

Study of Scatter Point Spread Functions

Scatter reduction algorithms typically require an estimate of the scatter PSF as prior knowledge. To gain insight into how the scatter PSF behaves in tomosynthesis conditions, the Monte Carlo simulation was modified so that the x-ray field was reduced to a pencil beam directed at the center of mass. The variation in shape of the scatter PSF for different projection angles is presented. This analysis was performed only for a breast in the CC view with CND=10 cm, T=2, 5 and 8 cm, G=0, 50 and 100% and projection angles from 0° to 30° in 6° steps.

To reduce computation time, a variance reduction scheme, based on the concept of importance sampling (Hammersley et al 1964), was introduced in the Geant4 simulation. This scheme consisted of modifying the Rayleigh and Compton scatter

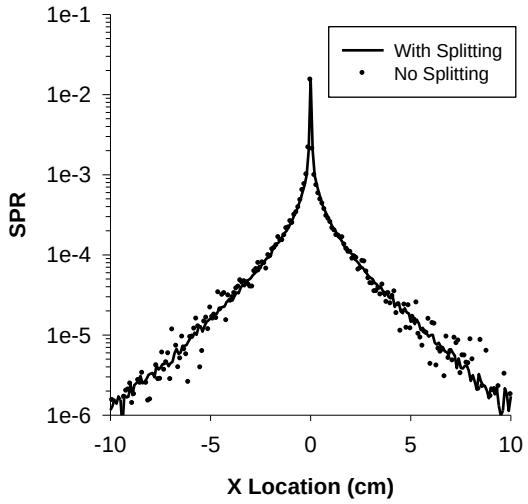

Figure 5.1 Comparison of a scatter PSF computed with and without the variance reduction scheme.

physics models so that at each scatter event, more than one photon would be output, each one sampled independently from the appropriate energy and angular distribution functions for the incident photon. To compensate for this multiplication of photons, a relative weight was assigned to each photon, so that each original photon emitted from the x-ray source had a weight value of 1, and this value was reduced according to the number of photons that were produced for each scatter event. For example, if, at each scatter event, the incident photon were split into 5 photons, these output photons would each have a relative weight of 0.2. If any of these photons scattered again, another 5 photons would be produced, each one with a relative weight of 0.04. When a photon arrived at the imager, the number recorded at that position would be the photon energy times its relative weight. To verify that this variance reduction scheme yielded the correct results, the same simulation was repeated with and without the variance reduction. The resulting PSF for both cases were virtually identical and are shown in Figure 5.1. This variance reduction scheme succeeded in reducing the number of emitted x-rays needed to be simulated, since the computer program spends more processing time following the

x-rays that have scattered, and less time following the primary x-rays that do not provide scatter information.

Validation

Although the Geant4 Monte Carlo toolkit has been already validated for x-ray scatter studies at mammographic energies (Grabski et al 2005), and this Geant4 tomosynthesis simulator was validated for glandular radiation dose predictions Chapter 2, the C++ program was modified to match the geometry described by Boone and Cooper (Boone et al 2000a) to compare Geant4's predictions on scatter PSF for the 0° projection angle with the scatter PSF reported for planar mammography.

Results

To verify the statistical precision obtained by performing monochromatic runs of 50 million photons, two simulations were repeated five times to compute the COV of the SPR at the COM. For an average breast, 5 cm thick, CND=11.6 cm, G=50%, projection angle=0°, the COV for the spectra below 27 kVp was lower than 1.25%, while for the rest the COV was 0.5% or lower. For a similar breast but with the maximum thickness, 8 cm, the COV for the Mo/Mo 25 kVp spectrum was 8.6%, while for the 27 kVp spectra the COV was lower than 5.0%, and for the 29 kVp spectra and above the COV fell to below 1.8%. Considering that in a clinical environment an 8 cm thick compressed breast is rarely imaged with a spectrum below 27 kVp, this precision was deemed sufficient.

Validation

Figure 5.2 shows the scatter PSF computed by the Geant4 simulation compared to those reported by Boone and Cooper (Boone et al 2000a). The scatter PSF presented

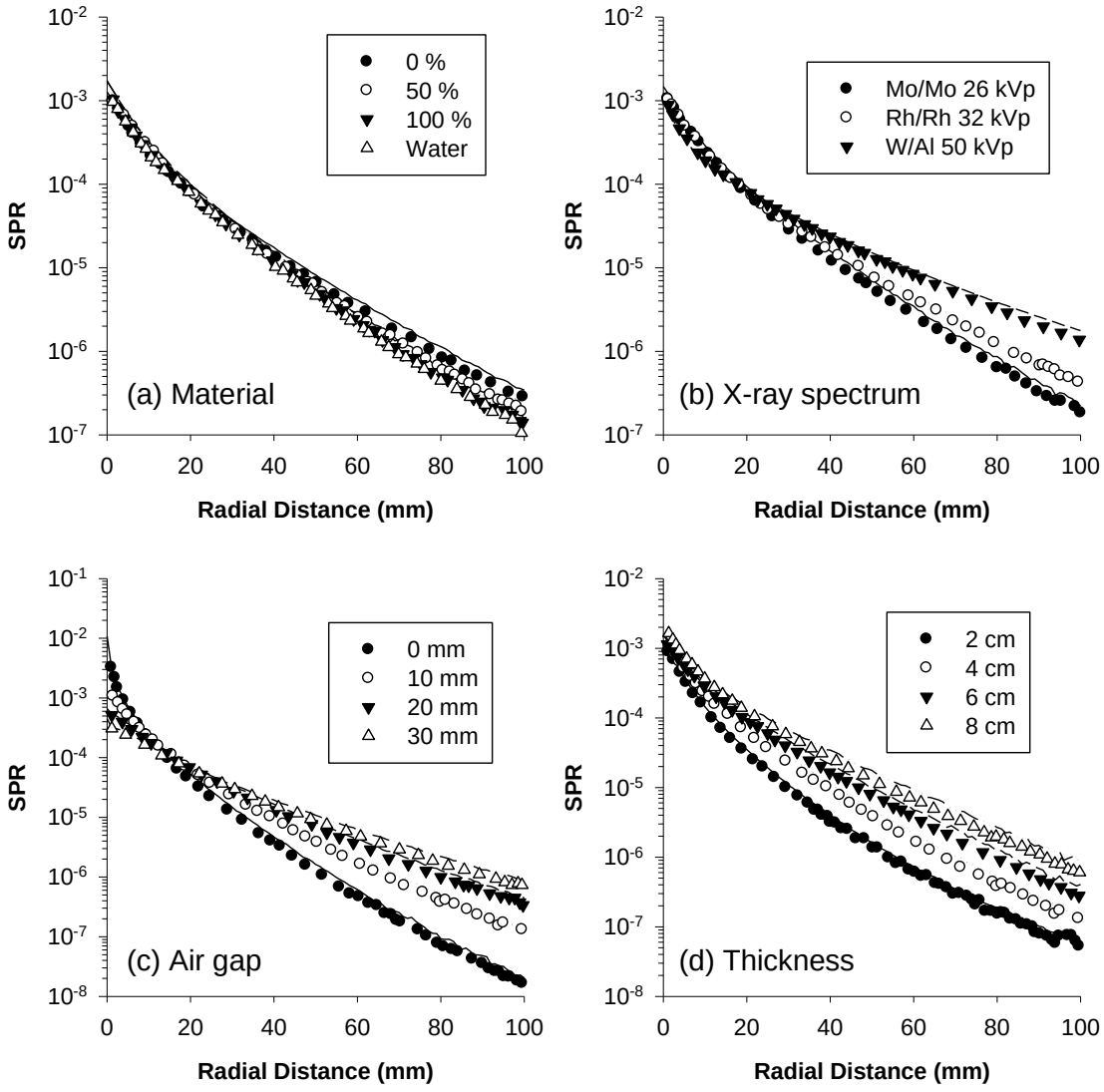

Figure 5.2 Comparison of the scatter PSF computed by the Geant4 program (lines) against those previously reported by Boone and Cooper (symbols) (Boone et al 2000a).

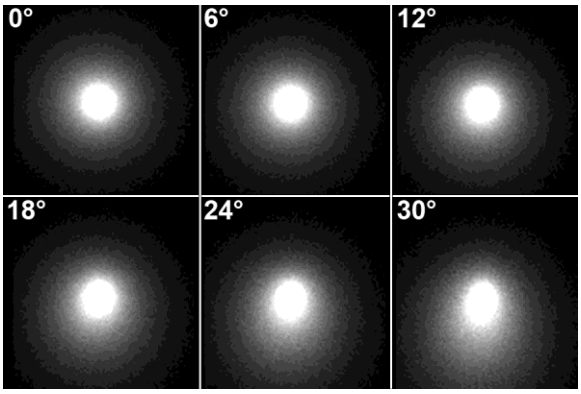

Figure 5.3 Images of the scatter PSF for a 5 cm compressed breast in the CC view for projection angles from 0° to 30°, in 6° steps.

are radially averaged and normalized to the number of primary photons detected. The results show agreement for all the variations reported by Boone and Cooper, which included varying breast tissue composition, x-ray spectrum, breast-to-imager air gap, and compressed breast thickness.

Qualitative Analysis of the Scatter Point Spread Function

Figure 5.3 shows images of the computed scatter PSF for a 5 cm thick compressed breast, 50% glandular fraction and tomosynthesis projection angles ranging from 0° to 30° in 6° steps. The radial symmetry of the 0° scatter PSF is clear. Some progressive loss of symmetry can be observed with increased angle, with the last two projection angles (24° and 30°) presenting an obvious asymmetry. In these images, the x-ray tube moves towards the top of the page with increasing projection angle. This shows that as the x-ray tube moves in one direction, the “tail” of the scatter PSF is extended towards the opposite direction. Vertical profiles through the center of the scatter PSF for the three different compressed breast thicknesses simulated are shown in Figure 5.4. The x-ray tube moves towards the negative side of the x-axis with increasing projection angle. The increase in scatter in the direction opposite to tube

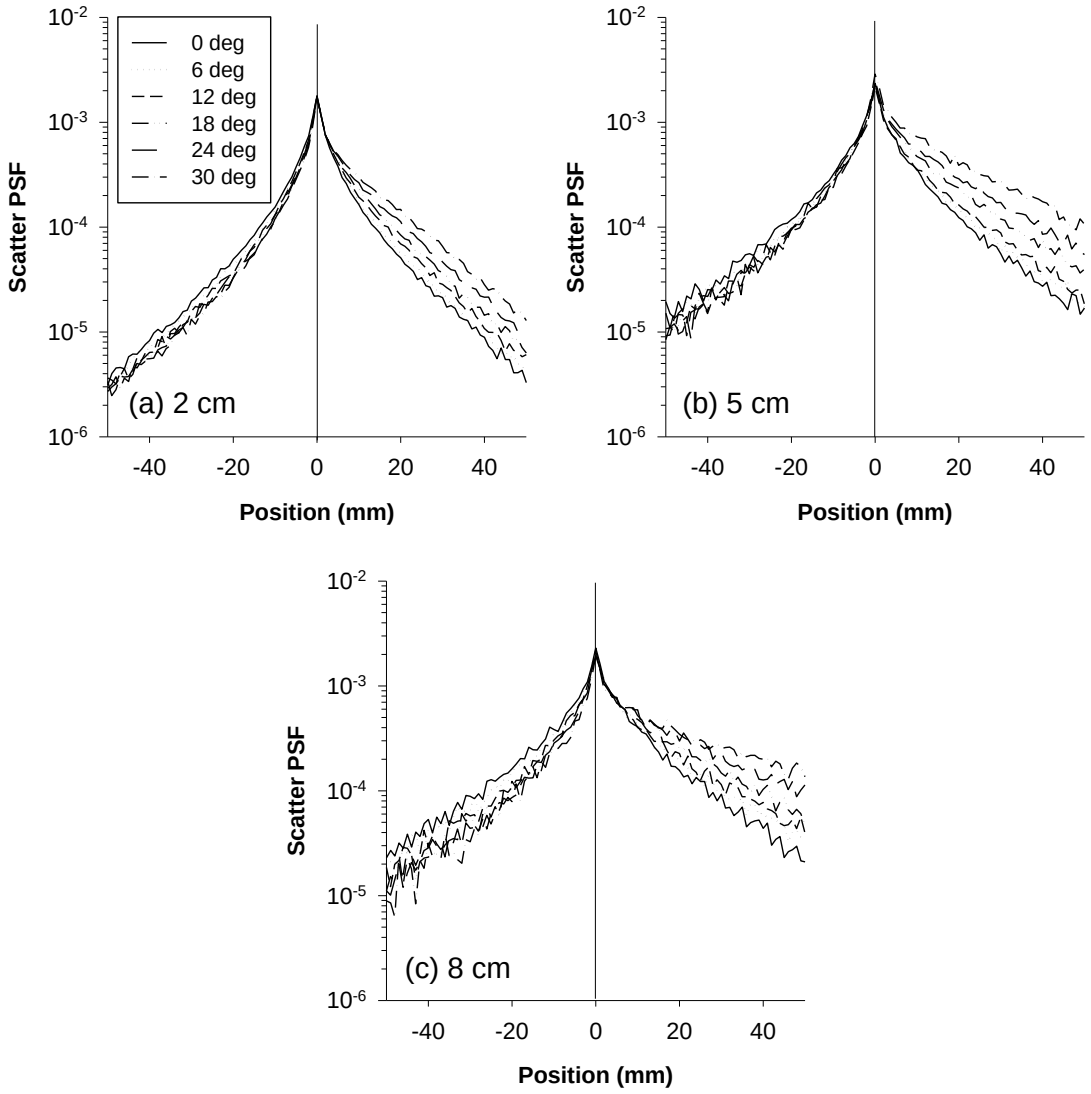

Figure 5.4 Vertical profile through the center of the scatter PSF of breasts of thickness 2, 5 and 8 cm.

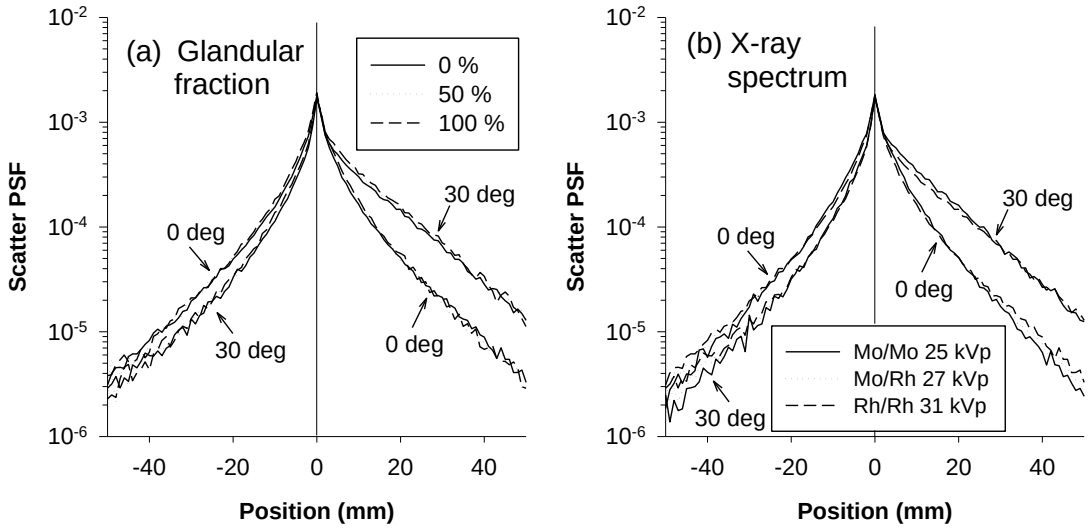

Figure 5.5 Sample graphs showing the variation of the 0° and 30° scatter PSF with varying (a) breast glandular fraction, and (b) x-ray spectrum.

movement, resulting in an asymmetric PSF, can be seen. This effect becomes more pronounced with increasing compressed breast thickness. It is important to note that asymmetry can be already seen at the 6° projection angle, which was not apparent in the two dimensional images.

The effect of glandular fraction and x-ray spectra on the behavior of the scatter PSF with angle is depicted in Figure 5.5. In both cases, as expected, a very small deviation was found.

Effect of the Breast Support and Detector Cover Plates on the Scatter to Primary Ratio

Figure 5.6 shows the computed SPR maps for compressed breasts of varying thickness in the CC view and in the MLO view for the 0° and the 30° tomosynthesis projection angle. The simulated breasts have a CND=11.6 cm (CC) and CND=13 cm (MLO), T=2, 5 and 8 cm and G=50%, and the x-ray spectrum is Rh/Rh 31 kVp. The images for the 5 and 8 cm thick breasts present a sharp increase in the SPR close to the outer edges of the compressed breast. This increase in SPR, although to a lesser

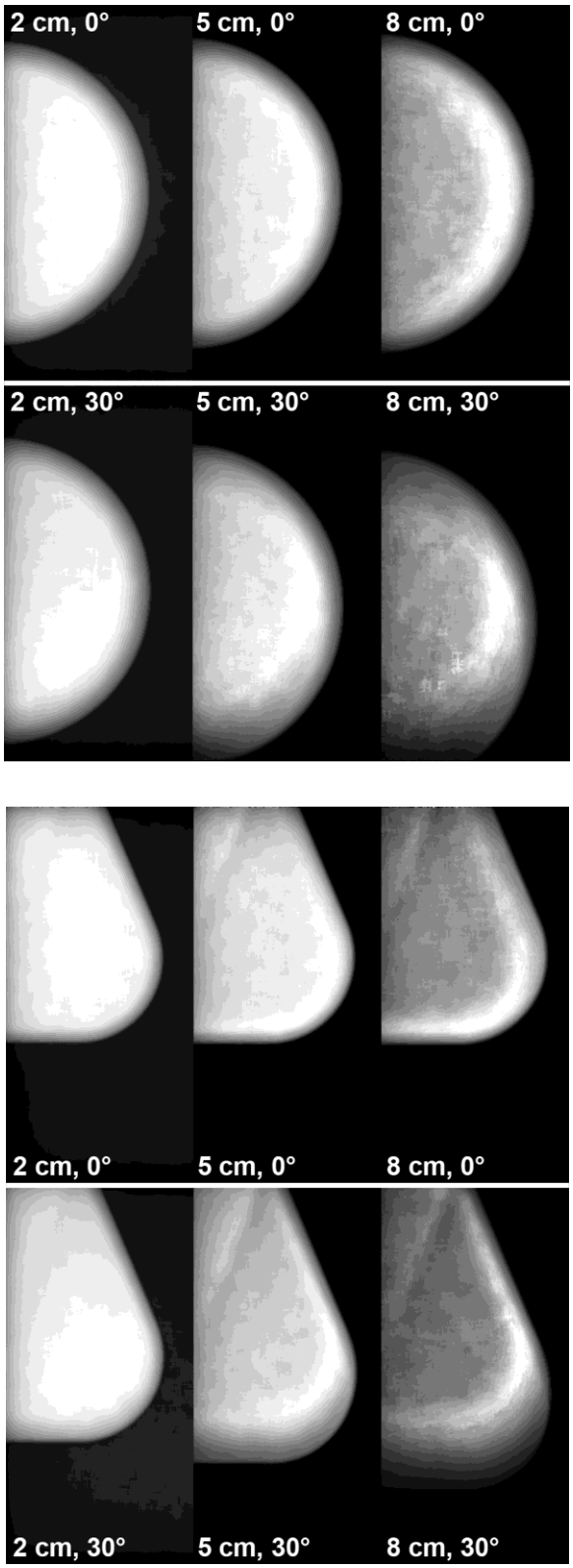

Figure 5.6 Images of the SPR for a CC (top) and a MLO (bottom) view breast showing the effect of the breast support plate and the detector cover plate.

degree, was previously reported by Lam and Chan (Lam et al 1990). To isolate the cause of these spikes in the SPR maps, three different modifications to the CC view simulations were attempted. In the first case, the possibility that this effect is due to the drop-off in tissue thickness at the curved edge of the compressed breast was studied by modifying the breast to be a perfect cylinder with semi-circular cross-section. To study the possibility that the inclusion of a 4 mm skin layer around the breast introduced unexpected differences in scattering cross-sections, the skin layer was eliminated in a second simulation. With these two variations, the spike in the SPR profile was still present.

The third modification of the simulation eliminated the breast compression plate, breast support plate, and detector cover plate. The results of this simulation are shown in Figure 5.7 where it is clear that this effect did not occur. Figure 5.8 shows horizontal (perpendicular to the x-ray tube's motion) profiles through the projection of the center of mass of the compressed breast showing clearly the effect that the presence of these plates have on the SPR. The spike and overall increase in SPR is due to the scattering contribution of the open field area of the plates. Although the plates are very thin compared to the compressed breast, the sections of these plates outside the area of the compressed breast are exposed to the full fluence of the x-ray field causing the absolute number of x-rays detected that underwent a scattering event in the open area to be high. Some portion of the x-rays that scattered in the plates is detected under the shadow of the breast, where the number of primary x-rays detected is reduced substantially due to the attenuation of the breast. This phenomenon is depicted graphically in Figure 5.9. The reduced attenuation of the primary x-rays in the thin breasts explains why this effect is not seen as prominently in the SPR maps for breast of T=2 cm.

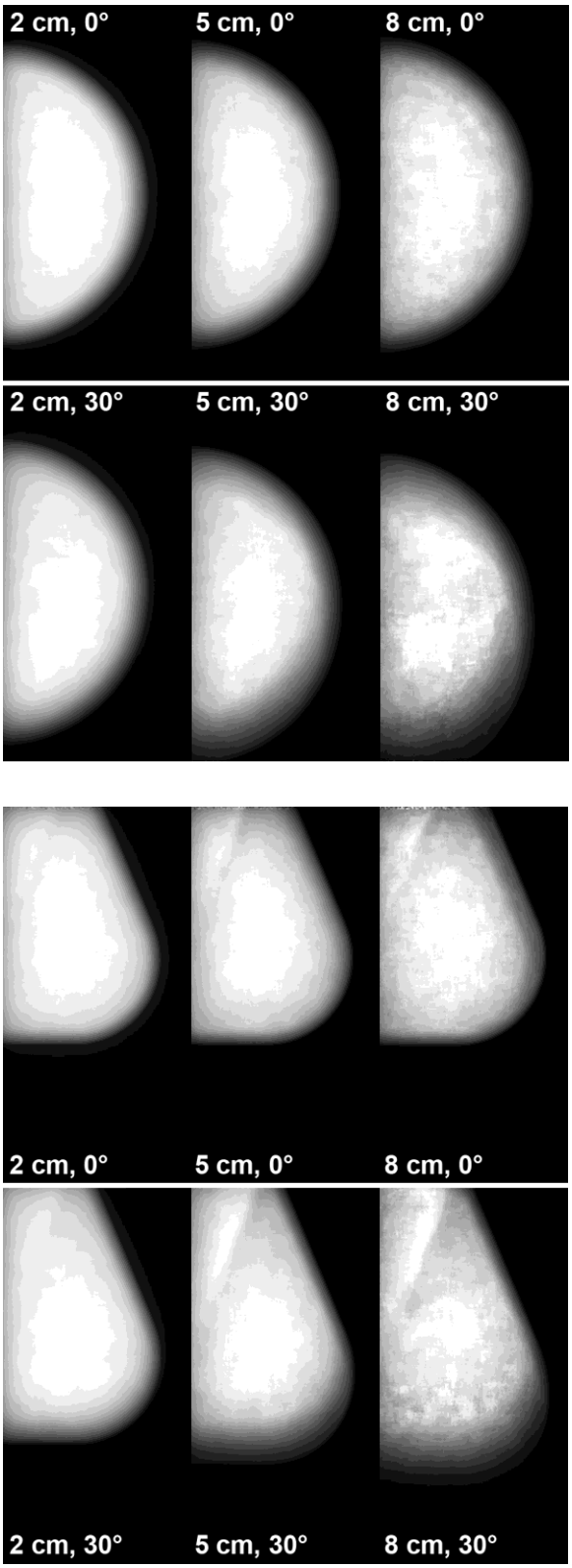

Figure 5.7 Images of the SPR for a CC (top) and MLO (bottom) view breast showing the absence of the increase in SPR when the breast support plate and the detector cover plate are not present.

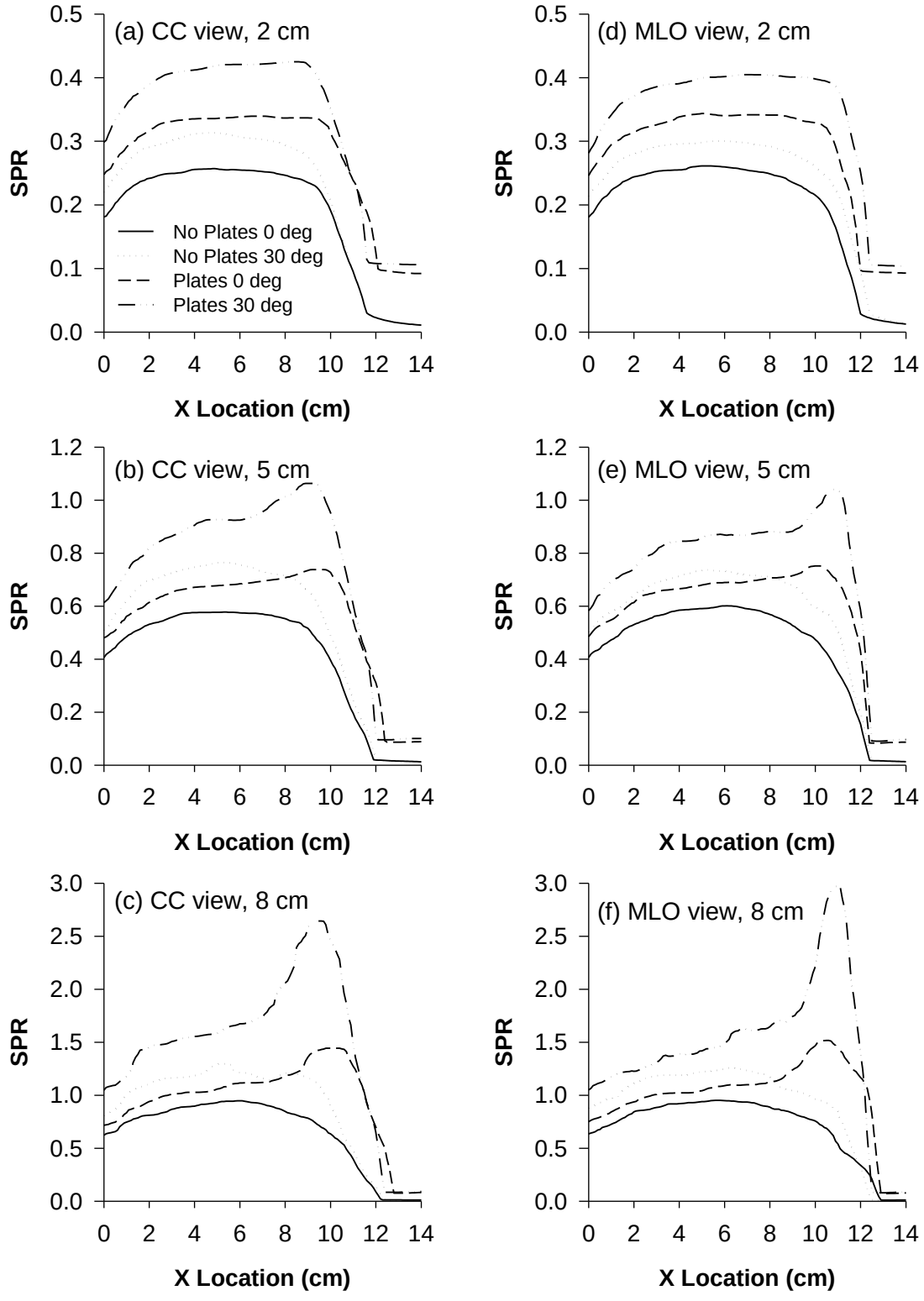

Figure 5.8 Horizontal profiles through the center of mass of the breast of the SPR maps depicted in Figure 5.6 and Figure 5.7. Profiles are for the CC view breast of thickness (a) 2 cm, (b) 5 cm, and (c) 8 cm, and for the MLO view with thickness (d) 2 cm, (e) 5 cm, and (f) 8 cm.

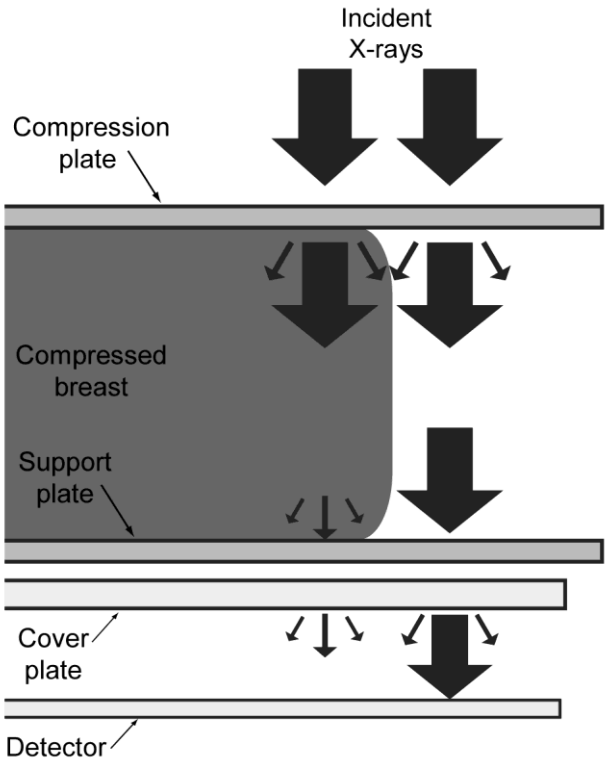

Figure 5.9 Diagram showing the cause of the SPR increase due to the presence of the breast support plate and the detector cover plate.

The rest of the SPR results reported in this paper are from simulations that include the breast compression plate, breast support plate and detector cover plate, since these are always necessarily present during a clinical tomosynthesis acquisition.

Scatter to Primary Ratio Maps

Figure 5.10 shows the 3D plot of the SPR maps of a compressed breast in the CC view (CND=11.6 cm, T=5 cm, G=50%, Rh/Rh 31kVp) for projection angles 0° to 30° in 6° steps. As in the scatter PSF section, the x-ray tube's movement with increasing projection angle is towards the negative side of the x-axis. The increase in SPR throughout the breast with increasing projection angle can be clearly seen. In addition, the symmetry of the SPR about the centerline of the imager is lost, with the tail of the SPR on the side opposite the x-ray tube becoming wider. This effect is expected, if one

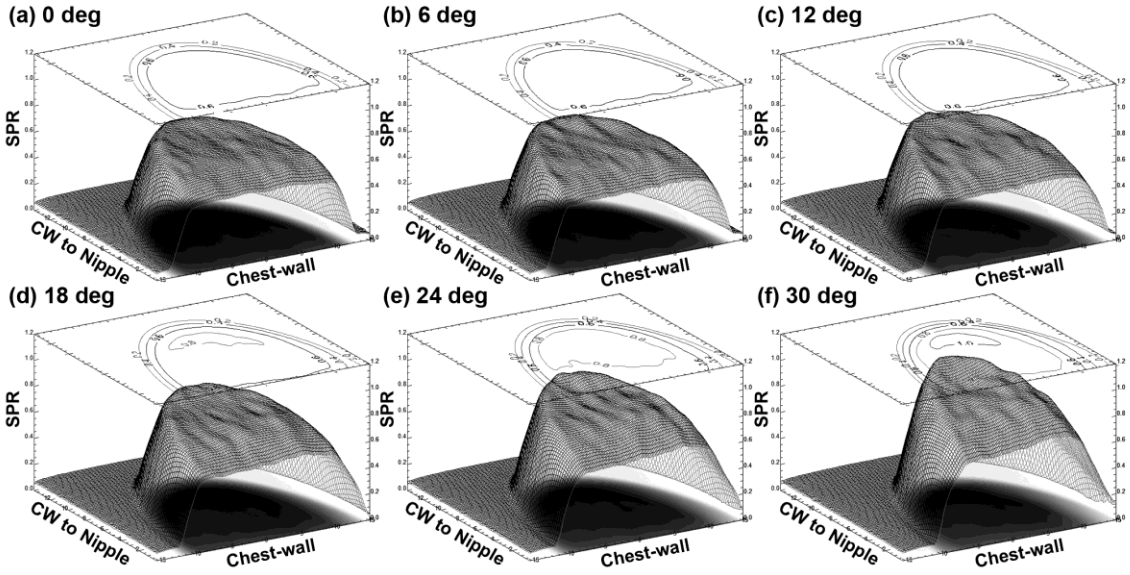

Figure 5.10 Surface and contour plots of the SPR for a CC view breast with CND=11.6 cm, T=5 cm, G=50% and projection angles 0° to 30° in 6° steps.

considers the shape of the scatter PSF described in the previous section. The increased SPR around the edge of the breast because of the presence of the compression plate, support plate and cover plate can also be seen, especially in the wider angle projection images. For improved visibility, profiles parallel to the chest wall (also parallel to the x-ray tube's motion), through the center of mass, are depicted in Figure 5.11. Profiles for compressed breasts of thickness 2 and 5 cm are also shown. The overall increase in SPR, loss of asymmetry, and the higher SPR at the borders can all be also seen in the profiles. In addition, the increase in SPR close to the borders of the breast can be seen more prominently for the T=8 cm breast.

Scatter to Primary Ratio at the Center of Mass

Figure 5.12 and Figure 5.13 show the variation of the SPR at the center of mass with varying breast size, thickness composition and x-ray spectrum for the CC and MLO views, respectively. Unless specified otherwise, the data shown is for a breast with CND=13 cm (11.6 cm for the CC view), T=5 cm, G=50% and Rh/Rh 31 kVp x-ray

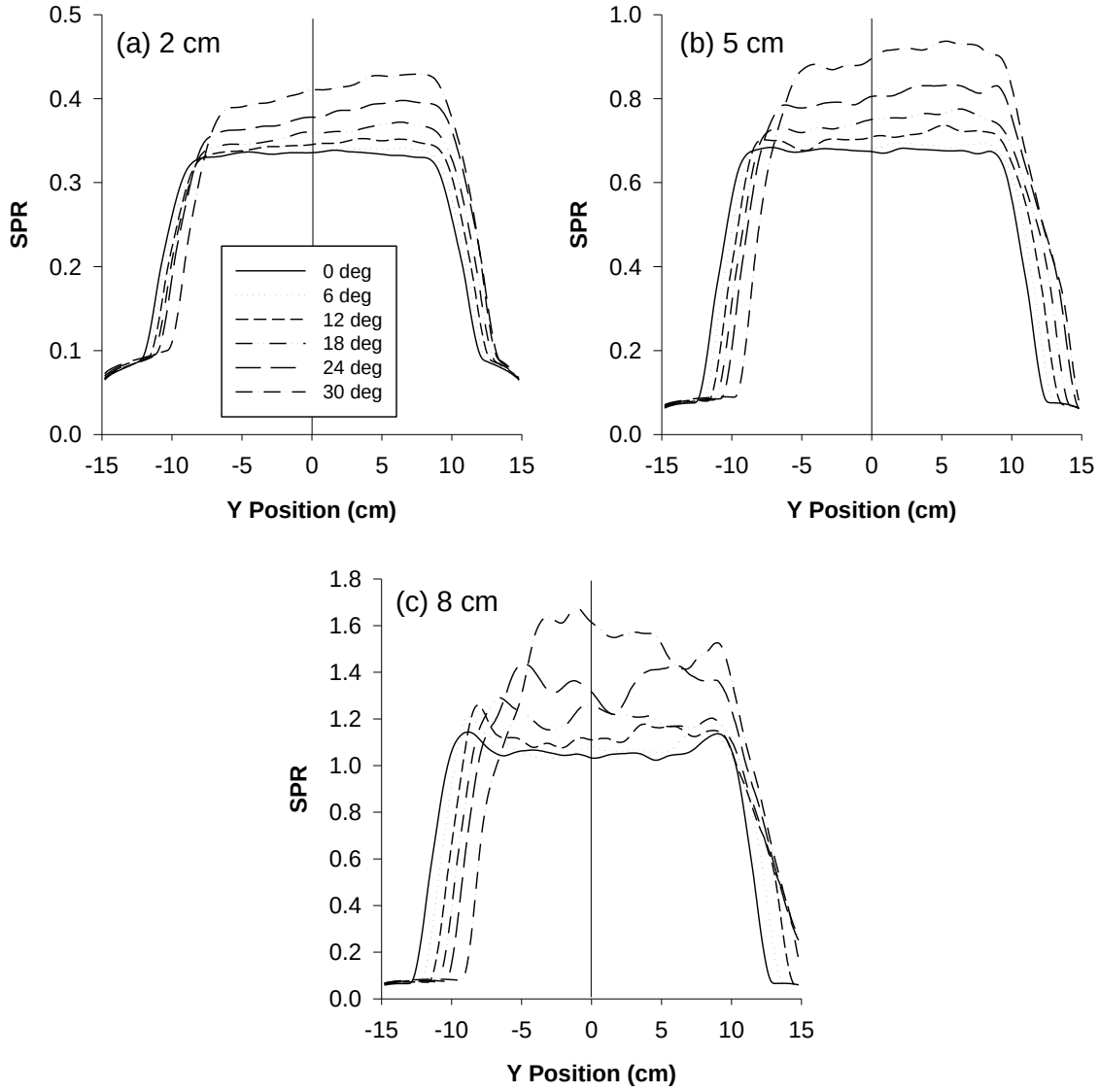

Figure 5.11 Profiles parallel to the chest wall, through the center of mass, of the CC view breast with a thickness of (a) 2 cm, (b) 5 cm and (c) 8 cm.

spectrum. As expected, SPR is most of all a function of compressed breast thickness, with a smaller dependence on glandularity and breast size. Specifically, chest wall to nipple distance appears to only have an influence on SPR when it is below a certain value. These results are consistent with those reported by Boone et al (Boone et al 2000b), in which the SPR curve approaches a horizontal line with increasing breast size

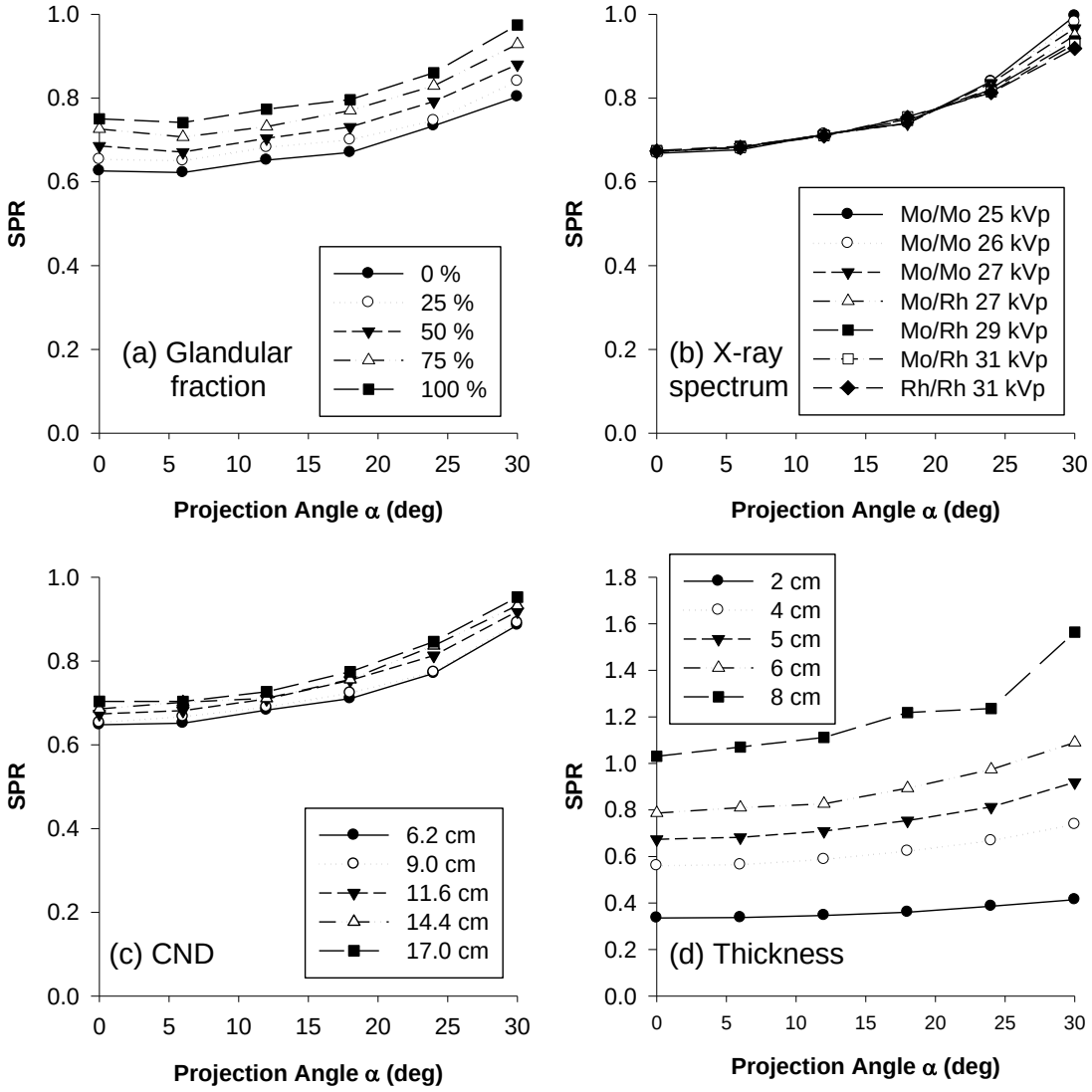

Figure 5.12 Sample graphs of SPR variation in the CC view with varying (a) breast glandular fraction, (b) x-ray spectrum, (c) chest wall to nipple distance and (d) compressed breast thickness.

and can be explained by the fall-off in intensity of the scatter PSF with radial distance. The x-ray spectrum does not appear to influence the SPR; the few data points that show some deviation can probably be attributed to higher statistical noise due to the fact that those points are the ones that include the fewest total x-ray histories.

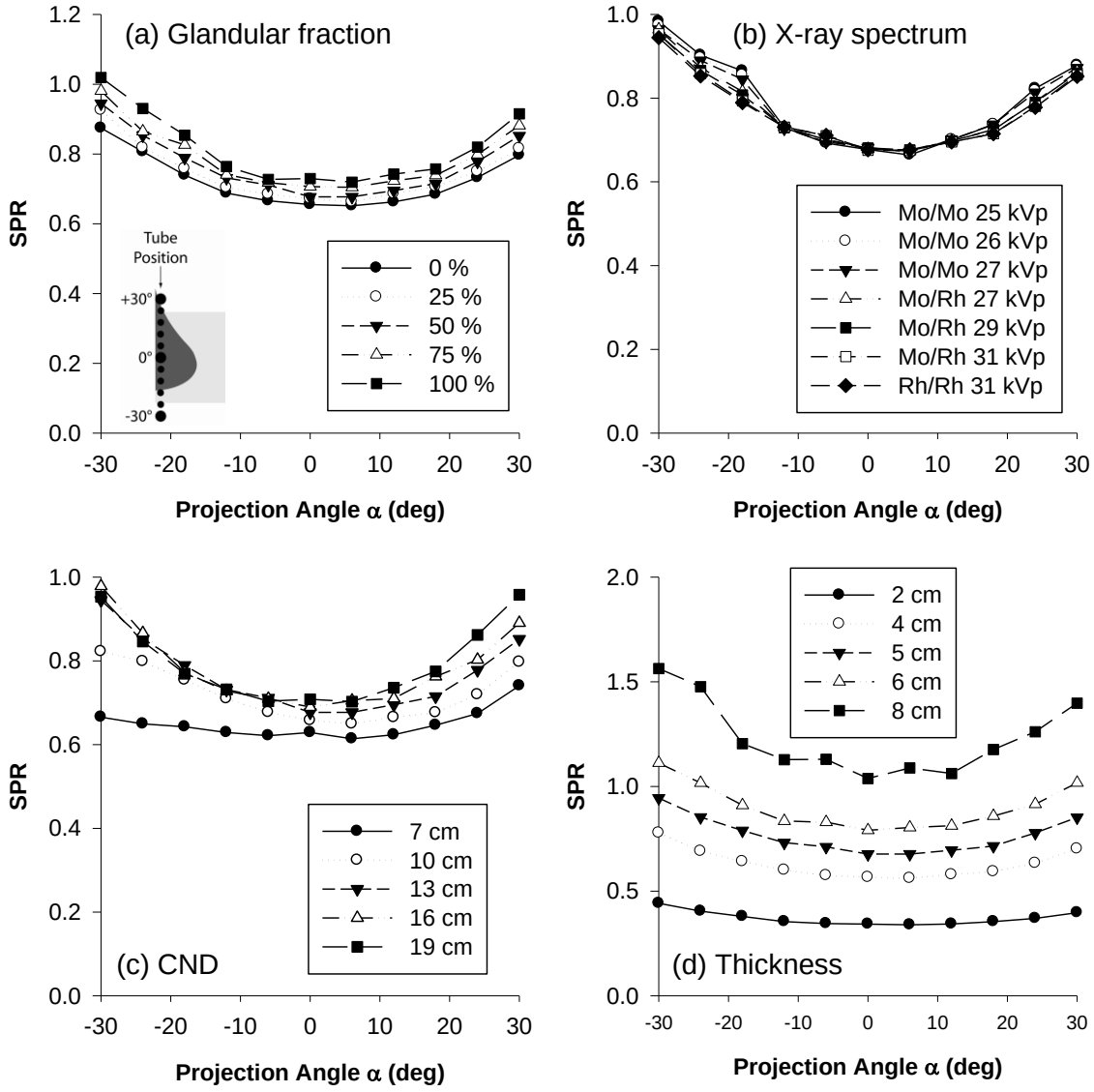

Figure 5.13 Sample graphs of SPR variation in the MLO view with varying (a) breast glandular fraction, (b) x-ray spectrum, (c) chest wall to nipple distance and (d) compressed breast thickness.

Given these results, the computed data was used to fit an equation for SPR as a function of tomosynthesis projection angle, compressed breast thickness and breast glandularity for each view. This was accomplished using commercially available software (TableCurve 2D and TableCurve 3D, Systat Software Inc., Richmond, California). Since TableCurve 3D can only fit functions with 2 independent variables, the glandularity

dependence was introduced as a linear coefficient to the surface equation found by TableCurve 3D for *SPR(T, α)*. The resulting equations for scatter to primary ratio at the center of mass for a tomosynthesis projection were:

For MLO View:

$$SPR_{MLO} = (aG + b)\frac{(c + dT + e\alpha + fT^2 + g\alpha^2 + hT\alpha)}{(1 + iT + j\alpha + kT^2 + l\alpha^2 + mT\alpha)} \quad (5.1)$$

For CC View:

$$SPR_{CC} = (aG + b)\frac{(c + dT + eT^2 + fT^3 + g\alpha)}{(1 + hT + i\alpha + j\alpha^2 + kT\alpha^3)} \quad (5.2)$$

Where *α* is the tomosynthesis angle (measured from the detector surface) in degrees; *T* is the compressed breast thickness, in cm; and *a* through *m* are the fit coefficients, given in Table 5.3. Both fits resulted in a $R^2 > 0.976$, and are applicable for any chest wall to nipple distance above 10 cm in MLO view, and for any CND for CC view.

Discussion

The variation found in the scatter point spread functions with varying tomosynthesis projection angle suggests the need of using different scatter PSF when attempting to perform scatter reduction image processing on tomosynthesis projections. Assuming the same scatter PSF for all projections would clearly result in sub-optimal corrections. To obtain estimations of the scatter PSF of a real breast, a Monte Carlo program like the one described in this study, which assumes a homogeneous breast is appropriate given the small variation in PSF for breasts with different glandular fractions. In addition, the same simulated scatter PSF can be used for breast imaged with different x-ray spectra, given the very small variation found within mammographic energies. To

Table 5.3 Coefficients for the fit Equations (5.1) and (5.2) to compute scatter to primary ratios at the center of mass, for both the MLO and CC views.

Coefficients	MLO View	CC View
a	1.324300E-03	2.088620E-03
b	9.337850E-01	8.955690E-01
c	1.169213E-01	9.800114E-02
d	9.455518E-02	1.116427E-01
e	-3.004900E-04	-8.647030E-03
f	-7.611100E-03	1.836750E-04
g	3.920070E-05	6.499170E-05
h	-1.561400E-04	-6.258962E-02
i	-9.134761E-02	-8.497300E-04
j	-6.803400E-04	-1.188400E-04
k	1.499353E-03	-1.570300E-06
l	-1.033000E-04	
m	-7.712700E-06	

compute the scatter PSF using Monte Carlo simulations, a variance reduction scheme like the one included in this work may be used, allowing for an important reduction in computation time.

If the scatter reduction technique being used involves an estimation of the SPR map as prior knowledge, it is important to compute the map with the presence of the breast support plate and detector cover plate included in the Monte Carlo simulation. As seen in the results, these contribute a very important amount of scatter close to the breast edge portion of the image, and in general increase the SPR throughout the whole breast. Using Boone et al's equation for SPR at the center of mass for a semi-circular breast in planar mammography (Boone et al 2000b), the SPR for the CND=11.6 cm, T=2, 5 and 8 cm breast should be 0.24, 0.55, and 1.03, respectively. In our simulations,

the values found when no plates are present were 0.26, 0.57 and 0.91 for the same three conditions. With the plates present, these values increase to 0.34, 0.67 and 1.03. This comparison not only serves as validation for our simulations, but show that if the plates are not taken into account, the SPR estimation in an image may be underestimated by as much as 31%.

By performing the same simulation for varying values of the four parameters relevant to the simulation, compressed breast thickness, breast size, glandular fraction, and x-ray spectrum, it was found that the SPR is, as expected, largely a function of thickness, and to a small extent, glandular fraction. The x-ray spectrum used, within mammographic energies, did not show any real variation in SPR. The breast size seems to affect SPR in very small breasts, when CND is past a certain threshold the SPR increase becomes very slow. This is expected due to the scatter PSF's limited range. Given these variations, equations were fit to be able to compute the SPR at the center of mass for a breast of any thickness between 2 and 8 cm, glandular fraction between 0 and 100 %, and for any tomosynthesis projection angle between ±30°.

Although in a clinical image an imaged breast will present anatomical structure, and is therefore not homogeneous, the small variations found in the scatter PSF and in the SPR maps for homogeneous breasts of varying glandular fraction seem to suggest that Monte Carlo simulations are still useful for the development of scatter reduction algorithms for application in clinical images.

Two other sources of resolution and contrast loss that are present in a clinical system but were ignored in this study are off-focus radiation and detector response. By excluding off-focus radiation from the simulation, the results presented are applicable independent of the x-ray tube used, and this effect can be added to the x-ray scatter effect described here. In addition, it has been shown that for the spectral energies analyzed in this study, the off-focus radiation-to-primary ratio varies approximately from

0.035 to 0.045 (Shen et al 2006), which is approximately 3 to 10% of the scatter to primary ratio found in this study, depending on the breast thickness.

The non-ideal detector response was excluded due to the vast variety of parameters (x-ray, optical, or electron spatial spread, conversion media thickness, packing fraction, columnar structure, etc.) that would have to be encompassed to make a comprehensive analysis. These effects have been studied for various imager technologies and incidence angles (Que et al 1995; Vedantham et al 2000; Mainprize et al 2006), and can be combined with the effects described in this study for any specific system.

In this study we assumed that the heel effect causes the same drop-off in intensity for x-rays of all energies. The validity of this assumption was checked by computing the first half value layer of the spectrum reaching the detector along the central ray (therefore exiting the anode straight down and entering the added filtration orthogonally) and of the spectrum reaching the detector at the farthest corner (therefore traveling through a longer path in the anode and the added filtration). The increase in HVL for the lowest energy spectrum used in this study (Mo/Mo 25 kVp) was found to be approximately 16%, while for the highest energy spectrum (Rh/Rh 31 kVp) was computed to be approximately 11%. Given the SPR's very weak dependence on x-ray spectrum, it is estimated that this difference is negligible.

Similar simulations for the study of scatter PSF and SPR, even with the presence of an anti-scatter grid, in the emerging field of dedicated cone beam breast computed tomography might prove useful, given the potential for introduction of artifacts in the reconstructed volume due to the inclusion of scatter in the projection images.

Conclusion

X-ray scatter inclusion in the image is an important concern in all radiographic applications. In digital tomosynthesis of the breast, x-ray scatter is an especially important consideration due to the difficulty of the use of an anti-scatter grid. To reduce the deleterious effect of x-ray scatter in tomosynthesis either before or during reconstruction, the magnitude and variation of the x-ray scatter field present in the projection images must be well understood. In this study, insight has been obtained as to the behavior of x-ray scatter in a tomosynthesis projection with varying projection angle. By analyzing the scatter point spread function and the scatter to primary ratio map for different conditions, the importance of considering the projection angle when attempting to reduce the scatter content of an image was identified. In addition, this data will be used in later chapters both to simulate the acquisition of tomosynthesis projection images and to correct for scatter during reconstruction.

The magnitude of the effect on the SPR due to the presence of the breast support plate and the detector cover plate was found to be higher than expected. This effect impacts not only tomosynthesis imaging, but planar mammography as well.

CHAPTER 6

THEORETICAL MODELING OF TOMOSYNTHESIS IMAGING SYSTEM

Introduction

To understand the limitations imposed by the imaging system on the quality of the tomosynthesis reconstruction, the effect on performance due to different imaging conditions must be understood. This characterization involves the analysis of the signal and noise transfer characteristics of the imaging system, and their variation under different imaging conditions, introduced by the various possible imaging protocols used for the acquisition of the tomosynthesis projection set. Furthermore, the characterization of the signal and noise transfer characteristics of the imaging system is required for the successful simulation of the acquisition of tomosynthesis projections. Universally accepted metrics that describe these characteristics are the modulation transfer function ($MTF(f)$), the noise power spectrum ($NPS(f)$), and the detective quantum efficiency ($DQE(f)$). The $MTF(f)$ describes the frequency-dependent signal transfer capabilities of an imaging system, and it is normally reported in the form of the presampling $MTF(f)$; the $MTF(f)$ before the discrete sampling of the signal by the detector pixels. The $NPS(f)$ is the noise equivalent to the $MTF(f)$, describing the square of the frequency characteristics of the noise present in an image. The $DQE(f)$ combines the signal and noise transfer characteristics described by the other two metrics to represent the fidelity of an x-ray imaging system.

In the past, mathematical modeling techniques based on the cascaded linear systems theory have been applied for the analysis of various x-ray imaging systems (Blume et al 1995; Spekowius et al 1995; Bissonnette et al 1997; Siewerdsen et al 1997; Zhao et al 1997; Siewerdsen 1998; Siewerdsen et al 1998; Ganguly et al 2003;

Vedantham et al 2004a; Suryanarayanan et al 2006). The theoretical derivation and application techniques of cascaded linear systems modeling have been described extensively (Metz et al 1979; Barrett et al 1981; Rabbani et al 1987; Rabbani et al 1989; Cunningham et al 1994; Cunningham 1998; Cunningham 2000; Cunningham et al 2001). These techniques are used to predict the *MTF*(*f*), *NPS*(*f*), and *DQE*(*f*) of a system, therefore characterizing system performance under specified conditions. These predictions are used to find the set of conditions which achieves maximum possible performance during design of the system and the imaging protocol, and to verify that the system is performing as expected.

In this study, cascaded linear systems modeling will be used to predict the variation in performance of the tomosynthesis imaging system with projection angle and with number of projections in the projection set. The first variation is caused by the angular dependence of the scintillator's modulation transfer function (Mainprize et al 2006). This angular dependence will also introduce a variation on the shape of the noise power spectrum, a factor that must be taken into account when performing projection acquisition simulations of a tomosynthesis system. The number of projections used in a tomosynthesis acquisition will impact the exposure available per projection to maintain a constant glandular dose to the imaged breast. Specifically, a projection set that involves a high number of projections will result in low signal levels per projection, affecting the inherent noise in each. This effect must also be taken into account when simulating tomosynthesis acquisition. With the use of serial cascaded modeling (Siewerdsen et al 1997; Siewerdsen 1998; Siewerdsen et al 1998), the signal and noise characteristics with these varying conditions will be found, and will later be applied in the simulation of tomosynthesis acquisitions.

Methods

Cascaded Linear Systems Theory

The cascaded linear systems approach consists of the step-by-step tracking of the signal and noise transfer characteristics of every stage in the imaging chain, resulting in the prediction of a metric describing the system's overall quality, in terms of the detective quantum efficiency. The imaging process is modeled as a series of stages, categorized into either amplifying or scattering stages (Rabbani et al 1987), each affecting the signal being acquired differently. Since the analysis is performed in the frequency domain, it imposes the assumption that the system is linear and shift invariant (Dainty et al 1974; Barrett et al 1981). Two variations of the cascaded linear systems analysis have been developed; the serial approach, developed by Siewerdsen (Siewerdsen et al 1997; Siewerdsen 1998; Siewerdsen et al 1998), applicable in imaging procedures where the x-ray energy levels remain below the k-absorption edge of iodine (33.2 keV), and the parallel approach, described by (Cunningham 1998; Yao et al 2001; Cunningham et al 2002), where the emission and re-absorption of the characteristic k-fluorescent x-rays in the scintillator are taken into account due to the presence of x-rays above the 33.2 keV threshold. In this study, the serial cascaded model was used since the results will be used to simulate projections acquired using x-ray spectra of energies under 33 kVp.

In cascaded modeling, the whole image acquisition process can be modeled using a combination of three elementary processes (Cunningham 2000):

i. *Quantum amplification:* Represents the conversion of the input quanta to a number of output quanta, governed by a random gain $\tilde{g}$ with mean $\bar{g}$ and variance σ_g^2. This process can also be used to represent a binomial selection process.

ii. *Deterministic blur:* Models the convolution of the signal with a known point spread function *psf*(*r*), which can also be represented in the frequency domain by *MTF*(*f*). An example of this process is the discrete sampling of the light field by the imager's pixels.

iii. *Quantum scatter:* Involves the image blur by a non-deterministic process, for example the scatter of light photons in the scintillator. It is described in the spatial domain by the scatter function *psf*(*r*), or its frequency domain equivalent, *MTF*(*f*).

To model an imaging system, a serial combination of these processes is put together in the appropriate order, where the output of one stage forms the input of the next. The input to a stage consists of two components, the signal and the noise characteristics of the quanta distribution, which consists of x-ray or light photons. The output of one stage consists of these same two components, but modified according to the transfer properties of the process.

Modeling of a Breast Tomosynthesis Imaging System

Using the three elementary processes described above, the stages involved in acquiring a tomosynthesis projection were modeled. Figure 6.1 depicts the acquisition stages involved and the characteristic parameters used to describe these stages. These parameters were used to derive the signal and noise transfer characteristics of a tomosynthesis system for 38 different projection sets, each with a different angular range and number of projections per set. The projections sets studied are listed in Table 6.1.

To compute the exposure available per projection for each set, the glandular dose to the imaged breast for a complete tomosynthesis acquisition was limited to 2 mGy. This upper limit and the angular range and number of projections in the set allowed for the computation of the exposure available per projection using the results of

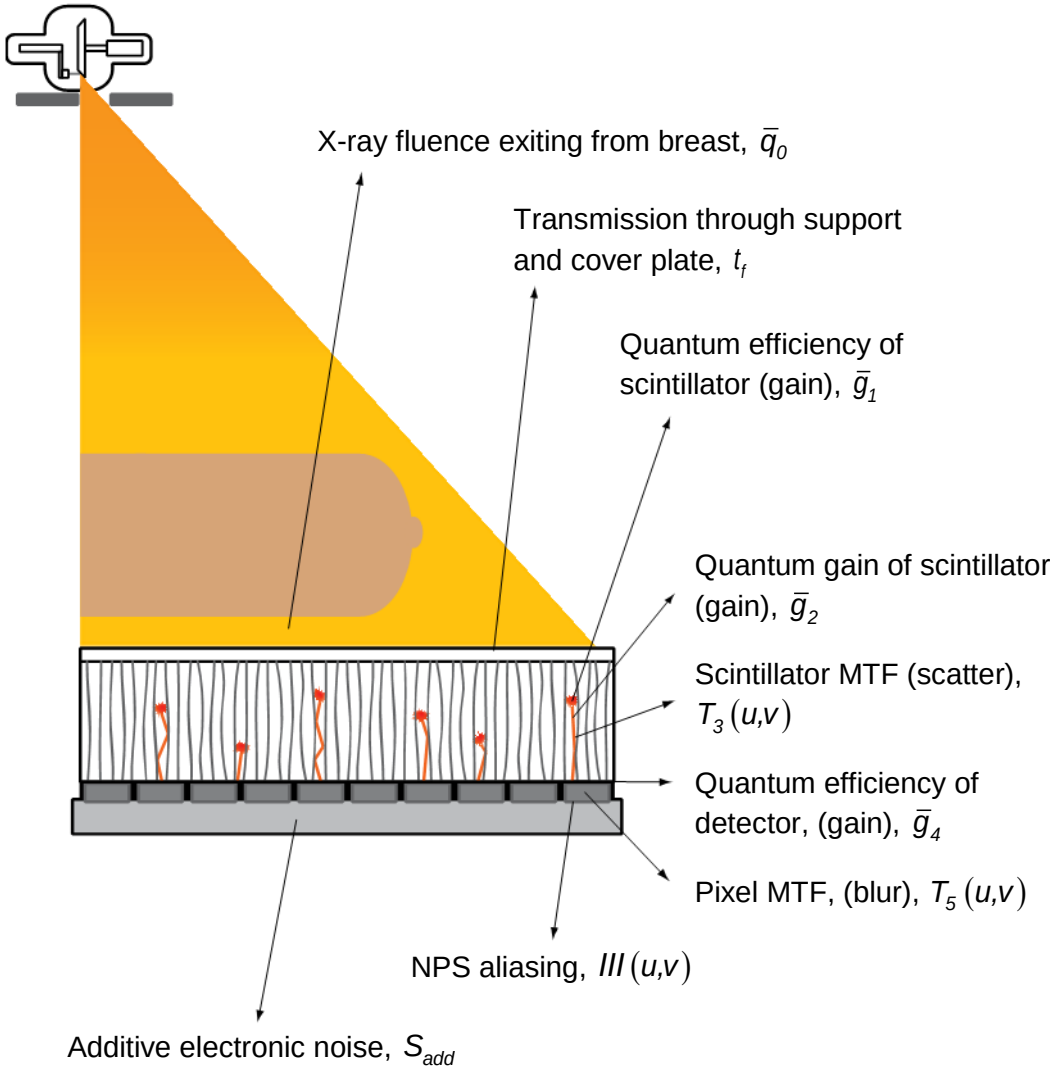

Figure 6.1 Signal and noise transfer stages in serial cascaded linear systems modeling of a breast tomosynthesis imaging system and their characteristic parameters.

Table 6.1 Tomosynthesis projection sets used in the serial cascaded model analysis. The exposure levels specified are at the entrance of the breast.

Angular Range (deg)	Number of Projections	Angular Step (deg)	Exposure per Projection (R)
8	3	4	0.606
	5	2	0.364
	9	1	0.202
16	3	8	0.610
	5	4	0.365
	9	2	0.203
	17	1	0.107
24	3	12	0.616
	5	6	0.368
	7	4	0.262
	9	3	0.204
	13	2	0.141
	25	1	0.073
32	3	16	0.625
	5	8	0.372
	9	4	0.206
	17	2	0.109
	33	1	0.056
40	3	20	0.637
	5	10	0.377
	9	5	0.208
	11	4	0.170
	21	2	0.089
	41	1	0.045
48	3	24	0.651
	5	12	0.384
	7	8	0.272
	9	6	0.211
	17	3	0.111
	25	2	0.076
	49	1	0.038
60	3	30	0.681
	5	15	0.396
	7	10	0.280
	11	6	0.177
	21	3	0.092
	31	2	0.062
	61	1	0.032

Chapter 2 for $RGD(\alpha)$ and $D_g N_o$. These exposure levels, also specified in Table 6.1, were used as input to the serial cascaded model. The model developed was based on the derivation by Siewerdsen (Siewerdsen 1998) for a planar mammography system, and assumed the characteristics of the detector to be equivalent to that of a current clinical digital mammography system. Following the stages depicted in Figure 6.1 the model was derived as follows:

Stage 0. Incident x-ray field: This stage describes the quantum image that is incident on the scintillating screen. This quantum image consists of a spatial distribution of x-ray photons of varying energy, according to the x-ray tube settings (target and filter materials, kVp, etc.) used and the thickness and composition of the various attenuating materials present between the x-ray source and the scintillator. The original x-ray signal was computed using the spectral simulations published by the Institute of Physics and Engineering in Medicine (Cranley et al 1997). For this study, the target and filter materials were set to Molybdenum, the target angle was set to 15º, the x-ray tube window was assumed as 0.8 mm thick Beryllium, and the filter thickness was set to 30 µm (Tkaczyk et al 2001). The x-ray spectrum was further attenuated by the breast compression plate, which was specified as 2 mm of polymethyl-methacrylate (PMMA) and the compressed breast, which in this study was specified as 5 cm thick, and composed of a homogeneous mixture of 50% glandular and 50% adipose tissue by mass. The elemental composition of the glandular and adipose breast tissues was specified as that described by Hammerstein et al (Hammerstein et al 1979), for which the attenuation coefficients used were those reported by the NIST (Berger et al 2005). From the spectral data, the mean number of x-ray photons at each energy per unit exposure of the whole spectrum, q_0/X was computed, according to the definition of the Roentgen (Johns et al 1983). Using the specifications provided by the manufacturer, the

energy dependent transmission factor of the breast support plate and cover plate, t_f, was found, resulting in the output signal of this stage, $\bar{q}_0 t_f$ and the mean number of photons incident on the scintillator per unit exposure *at the breast support plate,* $q_0 t_f / X$. Since the noise characteristics of the incident x-ray field follow the Poisson distribution, the output noise of this stage is equal to its signal, $\bar{q}_0 t_f$.

Stage 1. Interaction of x-ray photons with scintillator: This is a gain (or quantum amplification) stage which represents the stochastic process involved in whether an incident x-ray interacts with the scintillator or not. This binomial process yields a mean value of $\bar{g}_1$ which represents the mean quantum efficiency (QE) of the scintillator. This value was found by first computing the energy dependent quantum efficiency and then integrating over the x-ray spectrum as described by Siewerdsen (Siewerdsen 1998). The scintillator attenuation coefficients used were those reported by NIST (Berger et al 2005) and the surface density of the scintillator was estimated from data from the manufacturer (Hamamatsu Corp., Bridgewater, NJ).

Stage 2. Generation and emission of light photons: This gain stage is the result of the product of the generation of the light photons resulting from each interaction described in stage 1, $\bar{g}_{2a}(E)$, and the fraction of these that escape the scintillator towards the detector, $\bar{g}_{2b}(E)$. These were found using the equations derived by Siewerdsen (Siewerdsen et al 1997; Siewerdsen 1998; Siewerdsen et al 1998), assuming 55 light photons per keV of x-ray energy absorbed (Rowlands et al 2000) and a polynomial fit to the depth-dependent escape efficiency reported by Lubinsky (Lubinsky et al 2006). These two effects are combined as described by Siewerdsen (Siewerdsen 1998) into $\bar{g}_2$, the mean gain of the optical stage, and the noise contribution is characterized by the Poisson excess, ε_{g_2}.

Stage 3. Optical blurring in the scintillator: This stage incorporates the stochastic scattering inside the scintillator of the light photons generated in the previous stage. This stage, therefore, is treated as a quantum scatter stage. Physically, this process takes place coincidentally with the processes included in stage 2, but mathematically they are commutative, making the order of their application irrelevant. This photon spreading introduces the frequency and the projection angle dependence to the system. The angular dependence is caused by the positional variation of the light emission according to the depth in the scintillator where the x-ray was absorbed. This effect can be introduced as a product to that of the scintillator *MTF*(*f*), which is applicable for x-rays incident normal to the scintillator surface. Therefore the terms affecting the signal and noise in this stage are the characteristic scintillator *MTF*(*f*), $T_3(u,v)$, and the obliqueness *MTF*(*f*), $T_{3o}(u,v,\theta)$. The scintillator *MTF*(*f*) used was a fit to the result of the deconvolution of the empirical *MTF*(*f*) reported by (Suryanarayanan et al 2004) and the finite pixel size of the detector (Williams et al 1999; Vedantham et al 2004b). The obliqueness *MTF*(*f*) used was a surface fit to the data reported by (Mainprize et al 2006).

Stage 4. Absorption of light photons by the detector: This is a gain stage which represents optical coupling efficiency of the scintillator to the photodiodes in the detector. This efficiency is a combination of four binomial selection processes, namely (i) the transmission of photons through the surfaces above the photodiode, (ii) the light reflected at each of these surface boundaries, (iii) absorption of the light photons and conversion to electron-hole pairs, and (iv) collection of the resultant charge. These processes, taken as a single gain stage, result in a mean gain value $\bar{g}_4$ for which the value used was 0.49 (Jee et al 2003), and a gain variance given by $\sigma_{g_4}^2 = \bar{g}_4(1-\bar{g}_4)$.

Stage 5. Sampling of light photons in photodiode: This stage involves the integration of the light photons in each pixel, which is a deterministic blur process, and

can be characterized by the frequency domain response of the pixel, which is a sinc function, denoted $T_5(u,v)$. To obtain this function, the product of the pixel pitch a_{pix} (100 μm) (Vedantham et al 2000) and the square root of the fill factor f_{pix} (0.57) (Darambara et al 2002; Glick et al 2007) was used as the sinc function aperture size.

Stage 6. NPS aliasing: Due to the discrete sampling nature of any imager, the noise properties undergo aliasing, which is taken into account in this stage. Since the presampling *MTF*(*f*) is normally used as the characteristic signal transfer property of a detector, this aliasing does not have to be incorporated into the signal equation. Therefore the signal equations remain unchanged. Since the *NPS*(*f*) aliasing is a consequence of the discrete sampling of the input, this process is characterized as a two-dimensional convolution of the input NPS with a rectangular array of delta functions with spacing a_{pix} (Siewerdsen et al 1997; Siewerdsen 1998; Siewerdsen et al 1998). This yields another array of delta functions in the frequency domain, this one with spacing $u_s=v_s=1/a_{pix}$, which is denoted *III(u,v)*.

Stage 7. Additive electronic noise: The additive noise introduced by the electronics of the imager was added to the NPS by assuming white noise, with the magnitude estimated from manufacturer provided data (GE Healthcare, Waukesha, WI). This results in an additive noise term given by $S_{add} = \sigma_{add}^2 / 4u_N v_N$ where u_N and v_N are the Nyquist sampling limits along the two orthogonal directions (Vedantham et al 2004a).

This cascade of stages results in the three formulas that describe the mean signal, frequency-dependent signal, and frequency-dependent *NPS*(*f*) of the projections obtained with the tomosynthesis system as:

$$\bar{q}_{out} = a_{pix}^2 f_{pix} t_f \bar{g}_3 \bar{g}_2 \bar{g}_1 \bar{q}_0 \tag{6.1}$$

$$q_{out}(u,v,\theta) = a_{pix}^2 f_{pix} T_5(u,v) T_{3o}(u,v,\theta) T_3(u,v) \bar{g}_4 \bar{g}_2 \bar{g}_1 \bar{q}_0 t_f \tag{6.2}$$

Table 6.2 Summary of the values used for the parameters involved in the serial cascaded model.

Parameter	Value
X-ray tube target material	Mo
X-ray tube filter material	Mo
X-ray tube filter thickness	30 μm
kVp setting	26 kVp
Added filtration	0.8 mm Be
	2 mm PMMA
Breast tissue	5 cm, 50% glandular
Mean support and cover plate transmission factor, t_f	0.772
CsI:Tl thickness	100 μm
CsI:Tl suface density, ρ_s	42.8 mg/cm^2
Light photons per keV	55
Coupling efficiency	0.49
Pixel pitch, a_{pix}	100 μm
Fill factor, f_{pix}	0.57
Additive noise, σ^2_{add}	112985

$$S_{out}(u,v,\theta) = \bar{g}_4\bar{g}_2\bar{g}_1\bar{q}_0 t_f \left[1+\bar{g}_4\left(\bar{g}_2+\varepsilon_{g_2}\right)T_3^2(u,v)T_{3o}^2(u,v,\theta)\right]T_5^2(u,v)a_{pix}^4 f_{pix}^2 \\ **III(u,v)+\frac{\sigma_{add}^2}{4u_N v_N} \quad (6.3)$$

The frequency and angular dependent output *NPS*(*f*), $S_{out}(u,v,\theta)$, will be included in the simulation of the tomosynthesis projections for the optimization of the geometrical protocol, described in Chapter 7.

The model described above was implemented in Interactive Data Language (IDL 6.3, ITT Visual Information Solutions, Boulder, CO). Table 6.2 summarizes the values used for the parameters involved in the model. To test its accuracy, the predicted *DQE*(*f*)

for a 0º full exposure projection was compared to the empirically determined *DQE*(*f*) of a clinical planar mammography system (Suryanarayanan et al 2004).

Results

Validation

Figure 6.2 shows the result of the validation of the serial cascaded model by comparing an empirically obtained *DQE*(*f*) (Suryanarayanan et al 2004) against that predicted by the model. Excellent agreement can be seen.

X-Ray Spectra

Figure 6.3 depicts the x-ray spectra used for the modeling of the tomosynthesis projections. The graph in Figure 6.3(a) shows the energy distribution of the x-ray field incident on the breast, normalized to 1 R exposure at that point. The curves in Figure 6.3(b) show the x-ray spectra after the breast and after the support and cover plates. Both are normalized to 1R exposure *after the breast*. The preferential absorption of low energy x-rays by the breast is apparent, which also results in the much higher fluence needed to result in an exposure of 1 R.

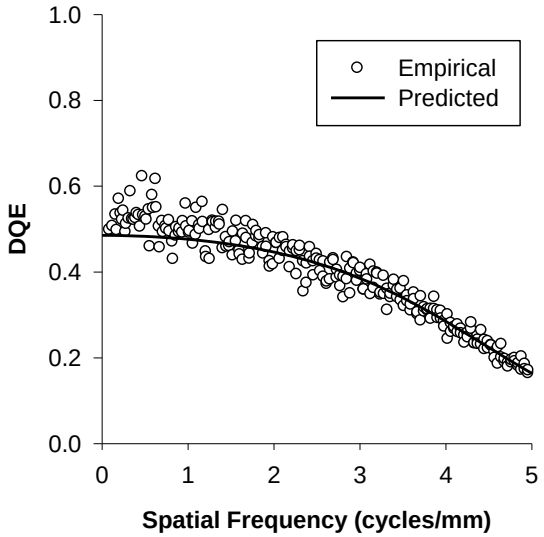

Figure 6.2 Comparison between the empirical (symbols) *DQE*(*f*) (Suryanarayanan et al 2004) and the predicted (line) *DQE*(*f*).

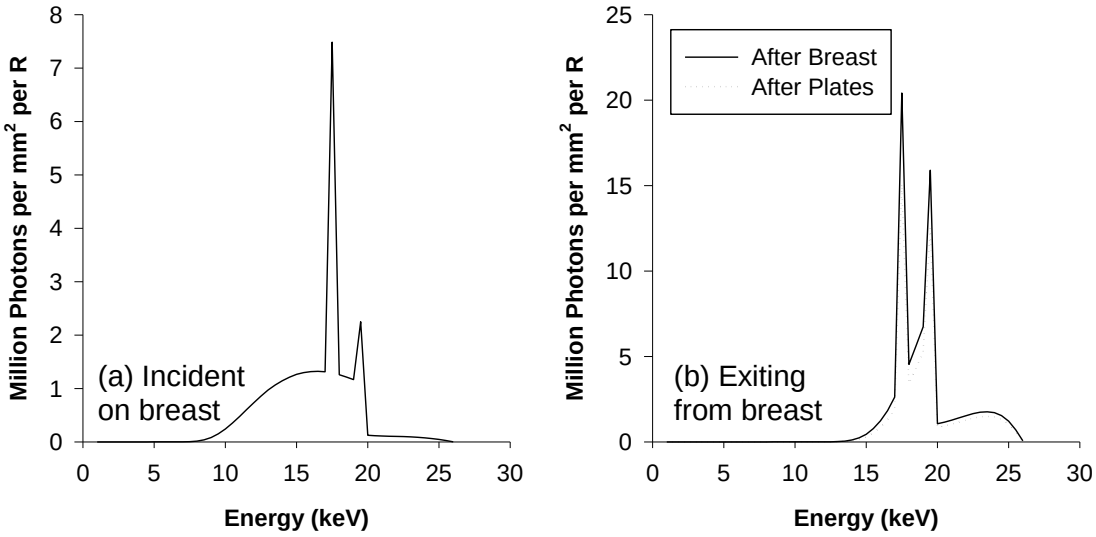

Figure 6.3 Simulated x-ray spectra (a) incident on the breast, and, (b) exiting the breast and the breast support and cover plates. The reference exposure in (b) is the exposure on the breast support plate for both spectra.

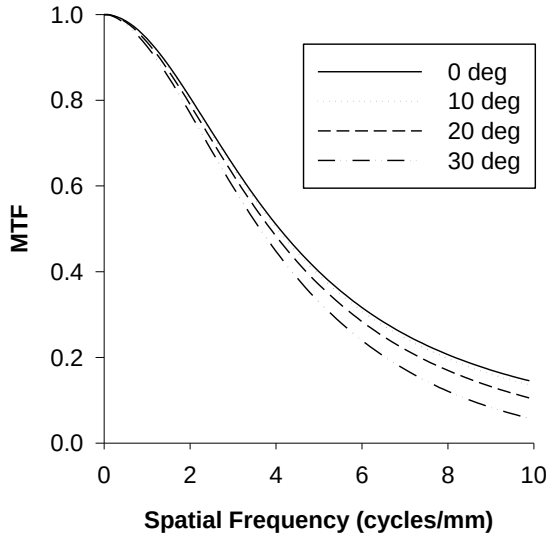

Figure 6.4 *MTF*(*f*) variation with projection angle.

Modulation Transfer Function

Figure 6.4 shows the product of the scintillator *MTF*(*f*), $T_3(u,v)$, and the obliqueness *MTF*(*f*),$T_{3o}(u,v,\theta)$, for four projection angles. The fall-off at high frequencies in T_{3o} with increasing projection angle introduces an important reduction in the signal transfer characteristics of the system.

Noise Power Spectra

The dependence of the noise power spectra with projection angle and with number of projections in the tomosynthesis projection set is shown in Figure 6.5. Graph (a) shows the variation in *NPS*(*f*) with varying number of projections per set, due to the decrease in exposure per projection. In graph (b) the variation in *NPS*(*f*) with projection angle for a given projection set (7 projection set) can be seen.

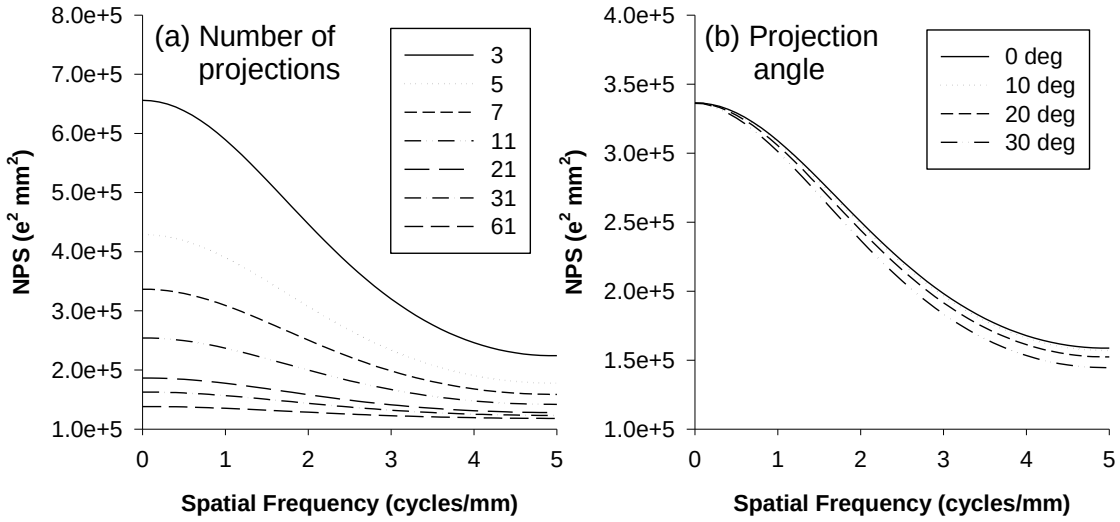

Figure 6.5 NPS for (a) 0º projection and varying number of projections in set, and, (b) varying projection angle of a 7 projection set.

Detective Quantum Efficiency

The predicted variation in *DQE*(*f*) with number of projections in each projection set is shown in Figure 6.6(a). The expected rapid fall-off in system performance with decreasing exposure is observed. The *DQE*(*f*) variation with projection angle within the same projection set, shown in Figure 6.6(b), is seen to not be substantial.

Discussion

Over the angular range studied, the noise characteristics of the tomosynthesis system, in the form of the *NPS*(*f*), vary substantially with projection angle and with the number of projections in the tomosynthesis set. The differences found with projection angle are introduced by the changing scintillator *MTF*(*f*), since the same pattern of decreasing values in the high frequencies are observed. These changes in *NPS*(*f*) signify that a different *NPS*(*f*) must be used when performing simulations of tomosynthesis projections.

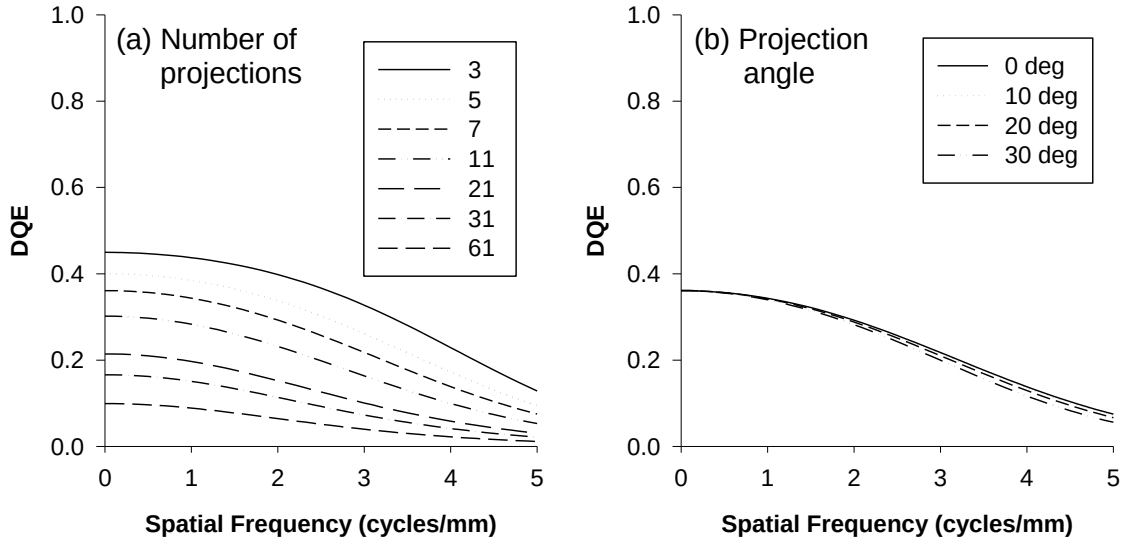

Figure 6.6 Predicted DQE for (a) 0º projection for sets with varying number of projections, and, (b) for varying projection angles of the 7 projection set.

A much more substantial effect on the *NPS*(*f*) is introduced by the necessary decrease in exposure per projection with increasing number of projections. The progressive loss of frequency dependence in the *NPS*(*f*) with decreasing exposure suggests that the white additive electronic noise is becoming dominant in the system, while the influence of the scintillator *MTF*(*f*) is becoming secondary, since under typical conditions the shape of the *NPS*(*f*) should follow the shape of the square of the *MTF*(*f*). This suggests that in an optimized tomosynthesis system, which needs to be designed specifically to handle low exposure acquisitions, the electronic noise will be the limiting factor in its general performance, and therefore the incorporation of technology to lower the electronic noise becomes critical.

The rapid drop in the *DQE*(*f*) with increasing number of projections is expected, given the assumption that the present clinical systems are operating at an exposure level just high enough to reach the quantum-limited state. Therefore, once the exposure is lowered under that used for planar mammography, the system's performance drops rapidly.

The *MTF*(*f*) and *NPS*(*f*) found in this chapter for the different angles in each of the 38 projection sets will be used to introduce realistic system-level limitations on the images simulated for the study described in the next chapter.

Conclusion

Based on published reports on the variation of scintillator *MTF*(*f*) and on the physical characteristics of a clinical planar mammography system, a mathematical model based on the serial cascaded modeling theory was developed to predict the performance of a digital tomosynthesis imaging system of the breast. This model was used to obtain angle and exposure dependent performance metrics, from which the necessity of minimizing the electronic noise present in a tomosynthesis system was found. In addition, the results of this study are needed to successfully perform simulations of projection acquisitions in digital tomosynthesis.

CHAPTER 7

OPTIMIZATION OF TOMOSYNTHESIS ACQUISITION GEOMETRY

Introduction

The geometrical acquisition protocol of a tomosynthesis study is defined by setting two variables, namely, the angular range of the complete acquisition and the number of projections included in the projection set. Assuming that the geometry used is symmetric around the 0º projection, and that the angular step size is constant, the two mentioned variables completely describe the geometrical protocol. The use of various angular ranges and number of projections per set has been published (Niklason et al 1997; Suryanarayanan et al 2000; Wu et al 2004b; Eberhard et al 2006; Chen et al 2007), but a comprehensive study of the optimal angular range and number of projections in a tomosynthesis projection set has not been reported. It is expected that by maximizing the angular range and the number of projections included in a tomosynthesis projection set the quality of the reconstruction is also maximized. This, however, is limited by the need to minimize the glandular dose to the breast during the tomosynthesis acquisition. Consequently, a trade off is encountered in which by increasing the number of projections, the exposure per projection must be lowered. This decrease in exposure will result in an increase in the noise in the projection images, due to increased quantum noise, and, as found in the previous chapter, a decrease in the DQE of the system.

In this chapter, using computer simulations, the effect that the angular range and the number of projections have in the tomosynthesis reconstruction quality is studied, and a geometrical protocol that maximizes the quality of the reconstruction is sought.

Methods

To compare the quality of the tomosynthesis reconstruction given various projection sets, three computer-based processes were performed. In the first place, a three dimensional matrix representing a volumetric portion of breast tissue with simulated lesions was created. Second, projections of this volume were acquired simulating the characteristics and limitations of a real world tomosynthesis imaging system. In the last step, the volume was reconstructed using these projections and the quality of the reconstructions was analyzed using appropriate metrics to quantify both the in-plane visibility of the lesions as well as the resultant vertical resolution.

Breast volume simulation

It has been reported that in the constant breast thickness regions of planar mammograms, the projection image of the breast tissue follows an isotropic 2D power law spectrum of approximately k/f^3, where k is a constant and f is the spatial frequency (Burgess et al 2001). This can be extended to the third dimension (Gong et al 2006), resulting in an equation in the frequency domain that governs the three dimensional anatomical structure found in normal breast tissue. A cube with 5 cm sides and with 100 µm voxels of breast tissue was simulated by filtering a white noise volume with the square root of the above function, and the result in the spatial domain was normalized to a minimum value of 0.0 and a maximum of 100.0. The values in each voxel of this cube were taken to represent percent glandular tissue fraction, such that a voxel with a value of 0.0 is composed of 100% adipose material, while a voxel with a value of 100.0 represents 100% glandular material. As expected, the mean value of the volume was approximately 50, representing a mixture of 50% adipose and 50% glandular tissue.

Three types of lesions were introduced in the breast volume: masses represented by 3 mm radius spheres with constant 65% glandular fraction (a value of 65.0), spiculations represented by cylinders of 0.5 mm radius, 5.0 mm length and 100% glandular fraction, and microcalcifications represented by a cube of 0.4 mm sides and attenuation equivalent to 30% apatite (Fandos-Morera et al 1988), resulting in a voxel value of approximately 2000.0. The masses and spiculations were included to measure in-plane soft tissue contrast in relatively large and small objects, respectively, while the microcalcifications were introduced as high contrast small objects to measure the vertical resolution of the reconstruction. Two copies of each lesion type were introduced in the volume to take into account the different cone angles involved according to the horizontal placement of the lesions, and to have two different samples of the visibility, given the randomness of the anatomic background. All the lesions were placed in the vertical center of the volume. Figure 7.1(a) shows the center slice of the volume, where the lesions can be clearly seen, while Figure 7.1(b) shows the resulting 0º projection of the 3D volume, where the reduced detectability of the soft tissue lesions is apparent.

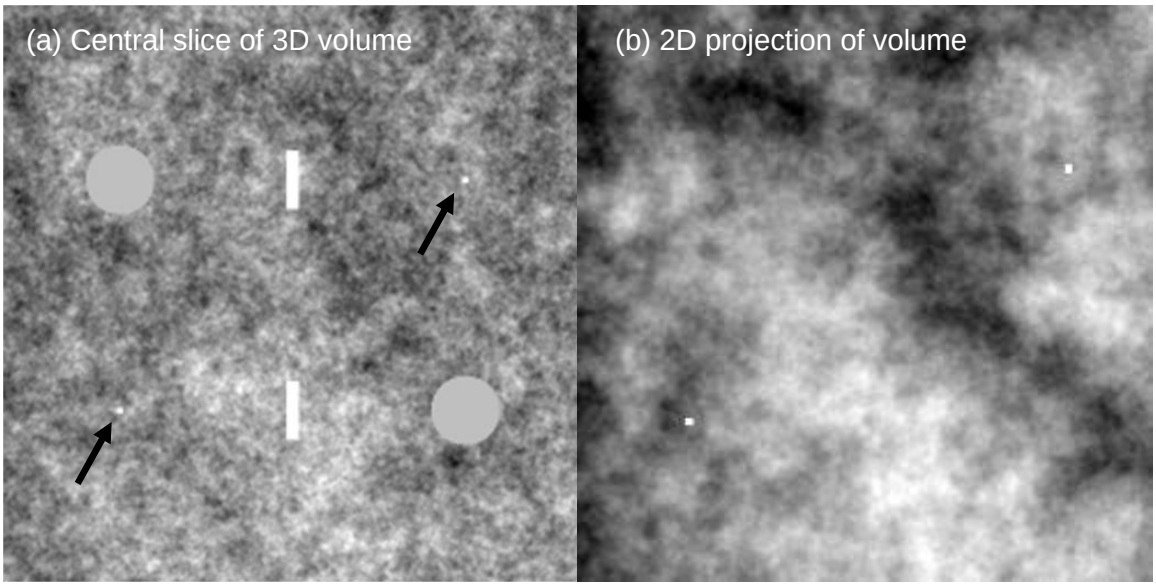

Figure 7.1 (a) Center slice of simulated 3D breast tissue. The simulated microcalcifications are marked with arrows. (b) Resulting 2D projection of the 3D volume.

Simulation of projection acquisition

To simulate the acquisition of tomosynthesis projections of the breast tissue volume taking into account all the characteristics and limitations of a clinical tomosynthesis imaging system, the processes summarized in Figure 7.2 were performed. The details of these processes are as follows:

Volume ray tracing: A ray tracing program based on the algorithm described by Siddon (Siddon 1985) was implemented in Interactive Data Language (IDL 6.3, ITT Visual Information Solutions, Boulder, CO). This implementation included the ability to specify the x-ray source to imager distance for the 0º projection, the distance from the imager to the center of rotation of the source, the number of projections and angle step to ray trace and the size and resolution of the volume and the projections. Since the

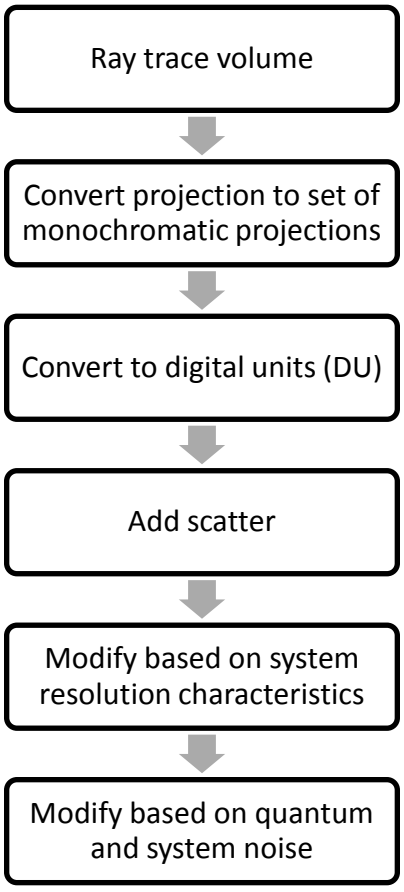

Figure 7.2 Summary of processes to simulate projection acquisition.

tracing of each ray is independent from all the others, the program was implemented as capable of parallel processing, to take advantage of multi-processor computers and computer clusters. For this study, a total of 61 projections were ray traced, covering an angular range of ±30º in steps of 1º. The detector size was set to 700 x 1600 pixels, with a resolution of 100 µm. The SID was set to 66 cm, and the DCOR to 0 cm.

Conversion to monochromatic projections: Normally, to obtain a ray tracing that represents the acquisition of a projection with a spectral x-ray field two approaches can be taken. The voxel values of the ray traced volume can be set to represent either the average linear attenuation coefficient of the material in the voxel for the x-ray spectrum used, or the ray tracing can be performed once for each energy in the spectrum, with each voxel value representing the linear attenuation coefficient of the material in the voxel for that energy. Although the first option involves only one ray tracing, beam hardening, the preferential absorption of low energy x-rays is not accounted for with this method. Ray tracing once per energy and for each projection angle takes too much computation time. Therefore, the volume was ray traced with the voxel values representing percentage glandular fraction, and then the projections were converted to monochromatic projections, each representing an energy present in the x-ray spectrum. To perform this conversion, linear fits were performed for the glandular fraction to linear attenuation coefficients at each energy level, using the data for elemental attenuation coefficients from NIST (Berger et al 2005) and for the elemental composition of the glandular and adipose tissue from Hammerstein et al (Hammerstein et al 1979). This resulted in equations of the form:

$$\mu(E) = g_v s(E) + z(E) \tag{7.1}$$

Where $\mu(E)$ is the energy dependent linear attenuation coefficient of a voxel containing material g_v, and $s(E)$ and $z(E)$ are the linear fit coefficients. Given Equation (7.1), the

conversion of the projection performed using the volume representing glandular fraction to monochromatic projections can be performed using the following derivation:

$$\begin{aligned} O(x,y,E) &= \sum_v \mu_v(E) T_v \\ &= \sum_v \left[g_v s(E) + z(E) \right] T_v \\ &= \sum_v \left[g_v s(E) T_v + z(E) T_v \right] \\ &= \sum_v g_v s(E) T_v + \sum_v z(E) T_v \\ &= s(E) \sum_v g_v T_v + z(E) \sum_v T_v \end{aligned} \tag{7.2}$$

This allows to ray trace the volume once per projection angle and, by storing the projection of the product of the voxel glandular fraction by the length traveled in each voxel and the projection of the total length traveled in the volume, and applying Equation (7.2), the projection of the product of the linear attenuation coefficient of each voxel by the length traveled in each voxel is obtained. The monochromatic projections for 5 to 26 keV in 0.5 keV steps were determined in this manner.

Conversion to digital units: To obtain simulated projections with the correct noise level, the result of the ray traces had to be scaled by the appropriate number of x-rays incident on the breast volume according to the number of projections in each set, and then convert the number of x-rays in each pixel to digital units (DU) in a clinical image. For this study, a total glandular dose to the imaged breast of 2 mGy resulting from the complete acquisition was set as the limiting factor. Using Equation (2.2) of Chapter 2 for D_g and the value for $D_g N_0$ found in Table 2.2 for a 5 cm thick breast in the CC view imaged with a Mo/Mo 26 kVp spectrum, the exposure per projection for each projection set was found. The projections sets used and the exposure incident on the breast volume found are listed in Table 6.1. The x-ray spectrum used for this study was the same one as that used in Chapter 6; Molybdenum target, 26 kVp, 30 μm Molybdenum

filter, 0.8 mm Beryllium window, and additional filtering by 2 mm of PMMA, representing the breast compression plate. The data used to obtain this spectrum were the x-ray spectra from Cranley et al (Cranley et al 1997) and the attenuation coefficients reported by NIST (Berger et al 2005).

The total exposure available per projection was used to compute the number of x-rays incident on the breast at each energy level from 5 to 26 keV in 0.5 keV steps, $N_0(E)$. The number of x-rays at each energy that exited the breast and reached each pixel in the projection, $N(x,y,E)$, were computed by multiplying $N_0(E)$ by the exponent of the negative of the corresponding monochromatic projection, $\exp\left[-\sum_v \mu_v(E)T_v\right]$. The total exposure arriving at each pixel was found by converting the number of photons at each energy level, $N(x,y,E)$ to the exposure at each energy $X(x,y,E)$ using the definition of the Roentgen (Johns et al 1983) and then summing the individual exposures to obtain a total exposure image, $X(x,y)$. To convert this exposure image to an image in DU, the relationship between DU and exposure had to be found. This relationship was found empirically using a clinical digital mammography system (GE Senographe 2000D, GE Healthcare, Waukesha, WI) by measuring the exposure incident on the detector using a calibrated dosimeter with a mammography ionization chamber (Radcal Corp., Monrovia, CA) and recording the mean DU signal in the resulting image over an area close to the central ray. The variance of the same area was also recorded to be used later in the noise addition step. To obtain measurements appropriate for this study, the x-ray tube was set to Mo/Mo 26 kVp, a 5 cm slab of 50% glandular breast tissue equivalent was placed close to the exit port of the x-ray tube, and the tube collimation was closed to the smallest area that covered the entire ionization chamber to minimize the inclusion of scatter x-rays. The exposure to DU relation found for different mAs was fitted to a line

and applied to the exposure images to obtain primary (non-scatter) projection images in DU, $I(x,y)$.

Addition of x-ray scatter: Since the breast tissue volume projected in this study represents the central portion of a compressed breast, the x-ray scatter field present in each projection was estimated to be a smoothed version of the primary projection scaled by a constant scatter-to-primary ratio. Therefore, the x-ray scatter field was estimated by multiplying the primary image $I(x,y)$ by the appropriate SPR for each projection angle and filtering the result with a smoothing filter with a kernel size of 21 x 21 pixels. The SPR to be applied was found using the surface fit for SPR at the center of mass found in Equation (5.2) of Chapter 5. The estimated scatter field was then added to the primary image.

Application of system resolution characteristics: The resolution limitations of a digital tomosynthesis system were estimated to be equivalent to those of a clinical digital mammography system (GE Senographe 2000D, GE Healthcare, Waukesha, WI), combined with the drop off in high resolution response due to the incidence of x-rays at an angle in oblique projections. These are the same signal transfer characteristics as those used in Chapter 6. The product of the digital mammography system MTF (Suryanarayanan et al 2004) and the oblique incidence MTF (Mainprize et al 2006) was multiplied by the Fourier Transform of the projection images, using the appropriate oblique incidence MTF for the projection angle involved in each image.

Introduction of noise: The magnitude of noise present in each projection is the limiting factor for not maximizing the number of projections in a tomosynthesis set. Therefore, the noise present in each projection must represent the appropriate magnitude of quantum and system noise given the exposure used to acquire it. To introduce noise in each projection the method described by Saunders et al (Saunders et al 2003) was followed. In the first step of this method a random white noise image is

multiplied in the frequency domain by the NPS of the system normalized to unity, resulting in a color noise image. The relationship between signal level and noise present in an image is then used to scale the color noise image in a pixel-by-pixel basis and the resulting noise is added to the noiseless image. To determine the relationship between signal and noise levels, the variance found for different exposure levels in the conversion to DU step was fitted against the mean signal.

The final images obtained after these processing steps simulate the projections of a breast tissue volume acquired with a digital tomosynthesis system, taking into account realistic x-ray absorption, x-ray scatter, system resolution limitations, and quantum and system noise characteristics.

Tomosynthesis reconstruction

The reconstruction algorithm used to perform this study was based on the iterative maximum likelihood expectation maximization (MLEM) approach (Rockmore et al 1977; Shepp et al 1982; Levitan et al 1987; Hebert et al 1989; Browne et al 1992; Manglos et al 1995; Pan et al 1997; Wu 2002). This reconstruction method was chosen for its balance between control of noise amplification and good vertical resolution (Wu et al 2004a), its capability of constraining the solution with a priori knowledge (e.g. non-negativity of voxel values), and the possibility of incorporating x-ray scatter correction in the reconstruction. MLEM reconstruction consists of an iterative approach in which the reconstructed volume maximizes the probability of resulting in the acquired projections, taking into account the Poisson statistics involved in x-ray imaging. This is achieved by performing an initial guess of the reconstructed volume, projecting this volume using the same geometry as that used for the acquired projections, and then adjusting the estimated volume by comparing the estimated projections with the acquired projections.

The maximization of the likelihood function dictates the adjustment of the estimated volume for the next iteration.

The reconstruction program was implemented in Interactive Data Language (IDL 6.3, ITT Visual Information Solutions, Boulder, CO) with multithreading capabilities to take advantage of multi-processor computers or computer clusters. The necessary inputs to the reconstruction algorithm are the acquired projections, the geometry used to acquire the projections (projection angles, x-ray source position and volume position with respect to the imager), the size and desired resolution of the reconstructed volume, the mean signal *S*, in DU, of the acquired projections where there is no attenuation present, and the number of iterations to run. Since this study involved ray tracing the same solid repeatedly for a fixed number of x-ray source locations, the ray tracing program based on Siddon's algorithm (Siddon 1985) described above was modified so as to save the coordinates of the voxels that each ray travels through and the length traveled inside each to a database in a hard disk. The ray tracing performed in the MLEM reconstruction program was then designed to only have to access this database and perform the multiplication of the voxel values with the corresponding length traveled in each voxel. This allowed for an increase in the reconstruction speed of approximately a factor of five.

In the first iteration, the reconstructed volume is estimated as a homogeneous solid of the appropriate size. This solid is then ray traced using the previously created database described above. The resulting ray trace *R* for projection angle α is denoted $R_\alpha(x,y)$. This image represents the array of sums of the products of the linear attenuation coefficients of each voxel with the length traveled in each voxel, specifically:

$$R_\alpha(x,y) = \sum_v \mu_v l_{vp} \tag{7.3}$$

Where μ_v is the linear attenuation coefficient of the voxel *v* and l_{vp} is the length travelled in voxel *v* by the ray that arrives at pixel *p*. To scale $R_\alpha(x,y)$ by the appropriate magnitude, the primary fluence incident on the volume is estimated by:

$$P = \frac{S}{1+SPR} \tag{7.4}$$

Where *S* is the mean non-attenuated signal inputted by the user, and *SPR* is computed using the results from Chapter 5. The projections of the estimated volume are then computed using:

$$E(x,y) = P \cdot R_\alpha(x,y) + SPR \cdot Sm\{P \cdot R_\alpha(x,y)\} \tag{7.5}$$

Where $Sm\{\ \}$ is the smoothing operator and *P* is the primary fluence found in Equation (7.4). Processing the ray tracing image $R_\alpha(x,y)$ with Equation (7.5) incorporates x-ray scatter correction into the reconstruction algorithm. This correction is especially important in tomosynthesis imaging of the breast due to the challenges involved in using a traditional anti-scatter grid. For clinical images where the whole breast is imaged and the SPR is not constant throughout the image, other methods of incorporating the x-ray scatter field in the projections can be used. These methods include convolving the primary projection with appropriate scatter PSF computed in Chapter 5. From the projections of the estimated volume found in Equation (7.5) the equivalent ray tracing is computed:

$$R'_\alpha(x,y) = -Ln\left[\frac{E(x,y)}{S}\right] \tag{7.6}$$

The images computed in Equations (7.5) and (7.6) are used to adjust the voxel values of the estimated solid according to the formula (Lange et al 1995; Wu 2002):

$$\mu_v^{i+1} = \mu_v^i + \frac{\mu_v^i \sum_p l_{vp}\left[E - Y_p\right]}{\sum_p l_{vp} R'_\alpha E} \tag{7.7}$$

Where μ_v^i is the estimate of the attenuation coefficient of voxel *v* in iteration *i*, l_{vp} is the length traveled by the ray *p* in the voxel *v* and Y_p is the acquired projection. The solid with the adjusted linear attenuation values, μ_v^{i+1}, is the input for the next iteration. If the number of iterations desired is reached, then this solid is the solution to the reconstruction. The number of iterations to perform on each projection set was set to four after testing a few projection sets by performing up to six iterations and finding that the noise present in the reconstruction started to increase in the fifth iteration.

Reconstruction quality analysis

To measure the quality of the in-plane feature reconstruction, the contrast-to-noise ratio (CNR) was used as the metric, defined as:

$$CNR = \frac{|\mu_S - \mu_B|}{\mu_B \sigma_B} \tag{7.8}$$

Where μ_S is the mean of the region of interest (ROI) in the signal (either the mass or the spiculation, μ_B is the mean of the ROI in the background (an approximately constant area close to the signal ROI), and σ_B is the standard deviation of the ROI in the background, representing the noise in the image. The ROIs of the signals and the backgrounds were selected to be of the same size.

To measure the quality of the vertical resolution of the reconstruction, the artifact vertical width (AVW), was defined. This metric measures the vertical resolution of the reconstruction by taking into account the amount of signal due to a feature present in the slices adjacent to the true position of that feature. To measure this for the simulated microcalcifications a ROI large enough to include the real signal and the artifacts present due to poor reconstruction was defined. The signal in the ROI of each slice was then averaged over the x direction, to obtain signal profiles in each slice. Then a morphological opening operation (Gonzalez et al 2002) was used to separate the signals

and artifacts of the microcalcifications present in the profiles from the background signal, and the result was subtracted from the original profile. This provided a profile for each slice consisting of only the signals and artifacts of the microcalcifications. The total area under the curve of each profile was then integrated, and the result was plotted against the vertical position. A linear combination of a quadratic and a Gaussian function was then fitted to each of these vertical profiles, from which the standard deviation of the Gaussian was used to obtain the full-width at half-maximum (FWHM) of the microcalcification signal, denoted the AVW. According to this definition, a low AVW represents better vertical resolution.

To determine the projection set that resulted in the highest reconstruction quality, the CNR of the four soft tissue lesions and the AVW of the two microcalcifications of the best iteration for each projection set were averaged separately, and the results normalized. For the AVW, in which a lower value represents a better reconstruction, the normalization was performed by dividing the minimum AVW by each AVW. For the CNR, the normalization was performed by dividing its each CNR with the maximum CNR. The product of the normalized metrics, denoted the quality factor (QF) was used to determine the highest quality reconstruction.

Results

Glandular fraction to linear attenuation coefficients fit

Figure 7.3 shows three of the linear fits computed for the conversion of the projections of the solid with voxels representing glandular fractions to monochromatic projections. The good fit of the linear functions over the whole range of the glandular fractions and a wide range of energies can be seen.

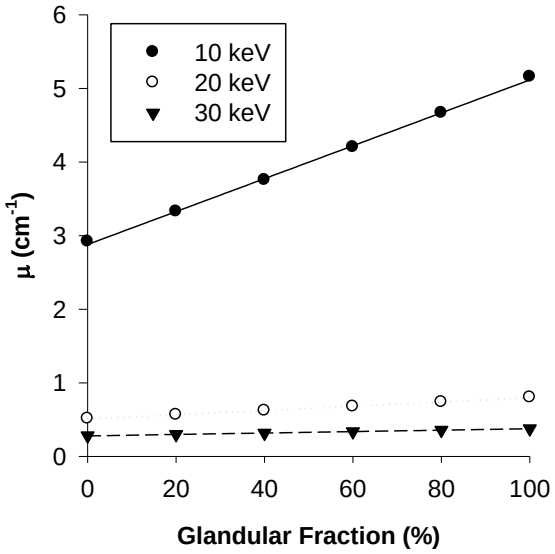

Figure 7.3 Sample of the linear fits computed for the conversion from glandular fraction to linear attenuation coefficients for various x-ray energies.

Relationship between image signal and exposure

Figure 7.4 shows the empirically determined relationship between exposure on the detector and image signal. As expected, the detector response was found to be linear, and the resulting linear fit equation is included in the figure. This equation was used to convert the exposure images $X(x,y)$ to the images in DU, $I(x,y)$.

Addition of noise to projection images

Figure 7.5 shows the relationship found between image signal and image noise, given by the signal variance. This relationship, found empirically, was used to apply the appropriate magnitude of noise to the simulated projection images.

The variation in magnitude of noise added to each projection with the number of projections in a projection set can be seen in Figure 7.6. The images in this figure are the 0º projections for sets with an angular range of ±30º.

Figure 7.7 shows a sequence of the resulting images after each of the steps implemented for the realistic simulation of tomosynthesis projection acquisition. The

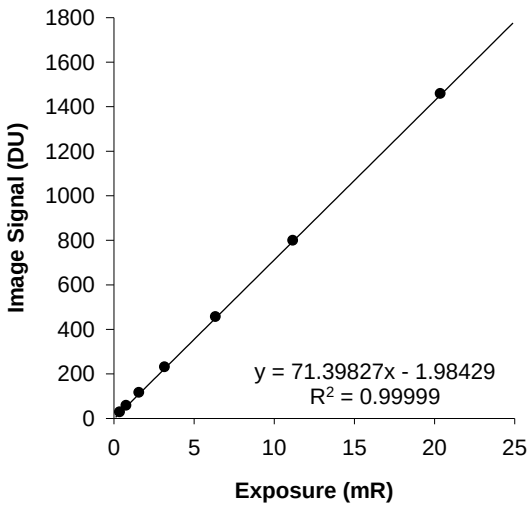

Figure 7.4 Empirically determined relationship between detector exposure and mean signal in the resulting image. The linear fit confirms the linearity of the imaging system.

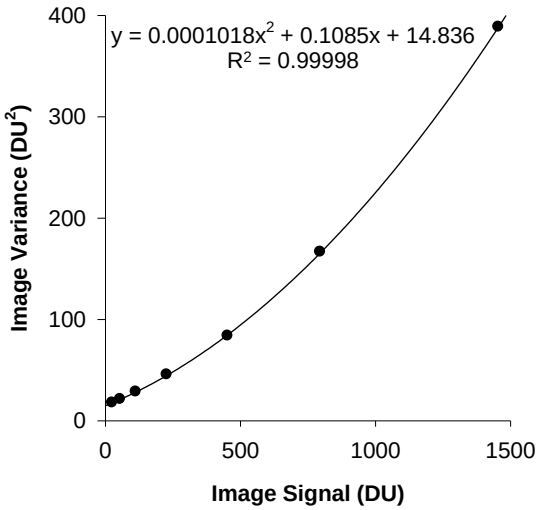

Figure 7.5 Empirically determined relationship between image signal and image noise.

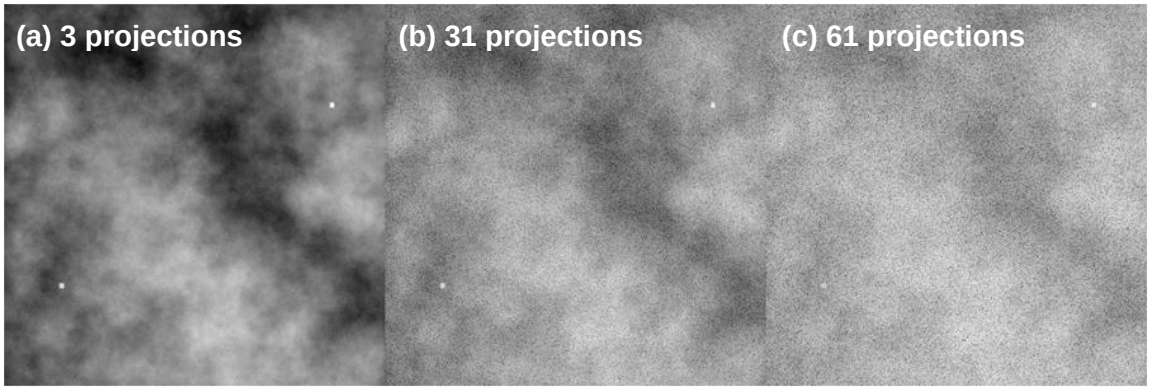

Figure 7.6 Difference in resultant noise levels according to the number of projections included in different projection sets. The increase in noise with increasing number of projections is apparent.

image in Figure 7.7(a) shows the original 0º projection resulting from the ray tracing of the breast tissue volume. Figure 7.7(b) shows the result of adding scatter to the original projection image. The blurring and loss of contrast associated with the presence of x-ray scatter is apparent. Figure 7.7(c) shows the final image of the projection acquisition stage. This image includes the system and oblique incidence MTF and the noise characteristics of the imaging system.

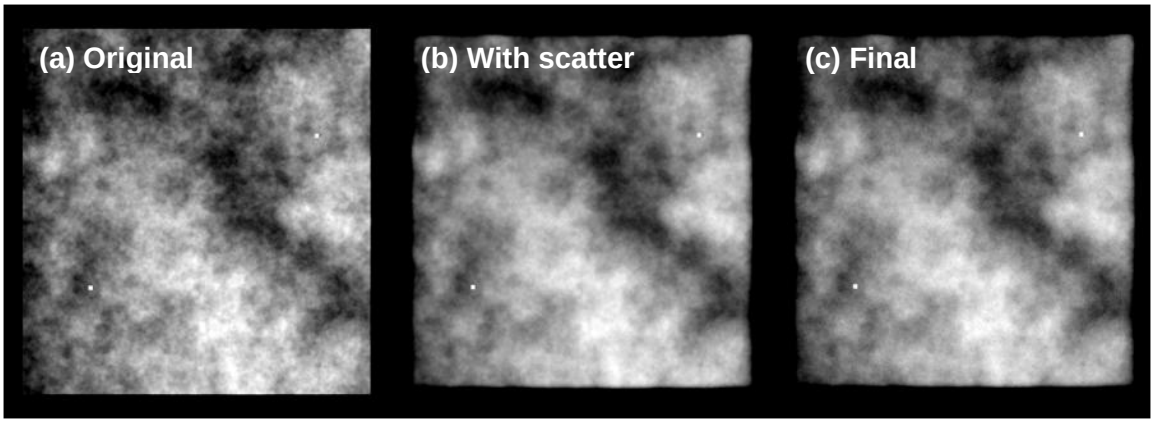

Figure 7.7 Sequence of the results of the image modification stages. (a) Original projection outputted from the ray tracing program, (b) projection after addition of scatter, and (c) after addition of resolution and noise characteristics. A decrease in contrast and resolution and the introduction of noise can be seen.

Tomosynthesis reconstruction

The best reconstructions, in terms of the highest CNR and lowest AVW values, were found to be after one or two iterations, depending on the projection set. For each projection set the reconstruction used was the one that yielded the best metrics.

Figure 7.8 shows the central slice of the reconstructions of the breast tissue volume resulting from six different projection sets with angular range ±30º after two iterations. The presence of the tissue superposition effect in the reconstructions of the sets consisting of 3 and 7 projections points to the lack of enough information in the projection sets for the reconstruction to be able to separate the vertical layers. This same limitation was found in all other reconstructions of the projection sets that included 7 or less projections and the sets with 9 and 11 projections that covered the widest angular range. In addition, all the projection sets that covered an angular range of ±4º were also deemed unsuitable due to their lack of vertical resolution. This elimination by visual inspection left only 18 different projection sets to be analyzed quantitatively. The result of the low exposure necessary due to a high number of projections can be seen in Figure 7.8(f), where the noise present in the reconstruction is considerable. This points to the expected tradeoff between vertical resolution and noise presence with increasing number of projections.

Quantitative tomosynthesis reconstruction analysis

Figure 7.9 shows the result of the morphological opening implemented to separate the background from the microcalcification signal. Graph (a) shows the result 12 slices away from the central slice, which contains the microcalcification. The correct separation from the larger central signal and the two artifact signals can be seen. Graph (b) displays the result for the central slice. The presence of only one higher peak is expected, and the correct separation of the background can again be seen.

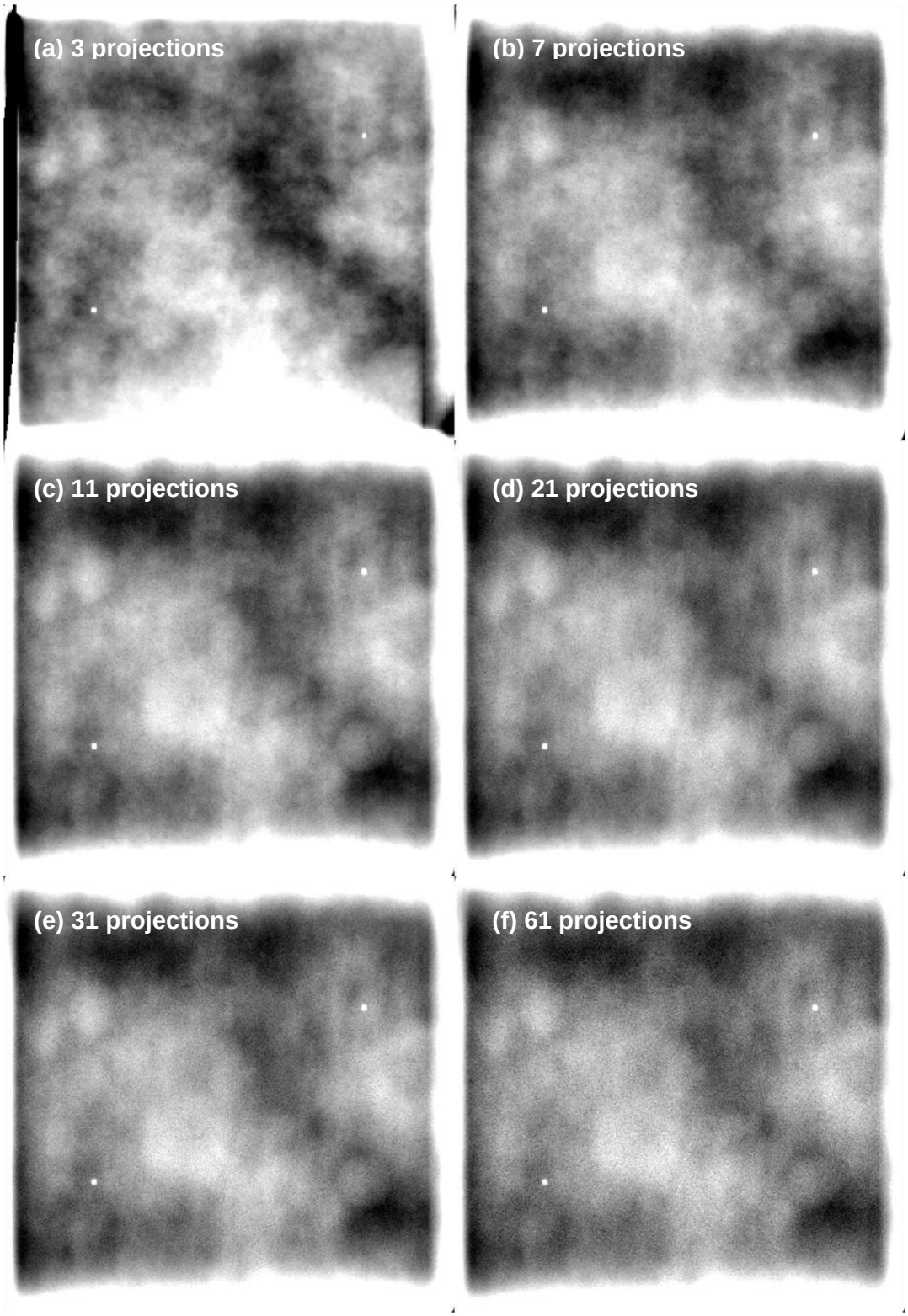

Figure 7.8 Central slice of the reconstructed volume for six different projection sets, all with an angular range of ±30º. The presence of tissue superposition in (a) and (b) can be seen, while the increase in magnitude of noise in (e) and (f) is apparent.

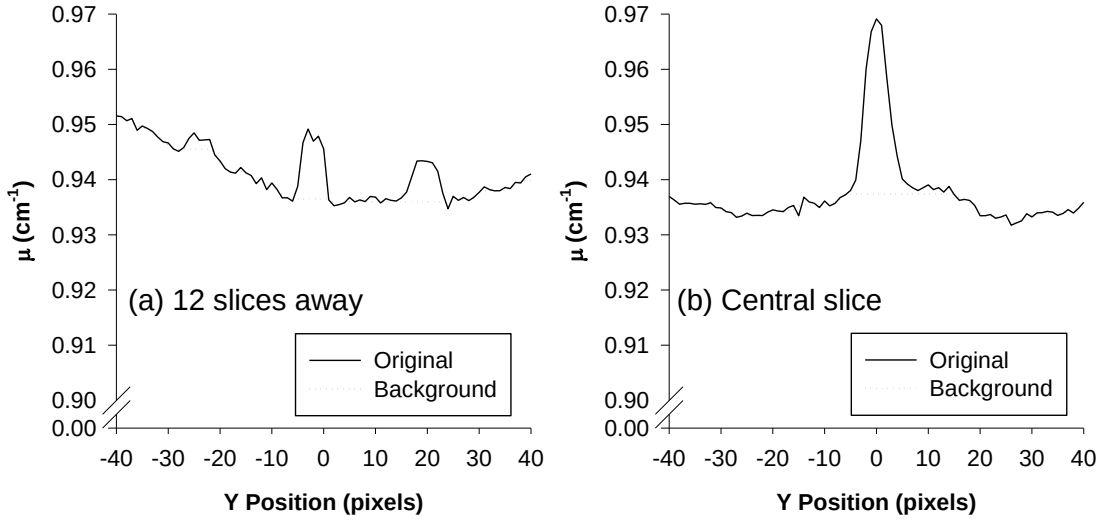

Figure 7.9 Profiles of the microcalcification signal in (a) 12 slices away from the central slice, and (b) the central slice, showing the result of the morphological opening to separate the background from the signal.

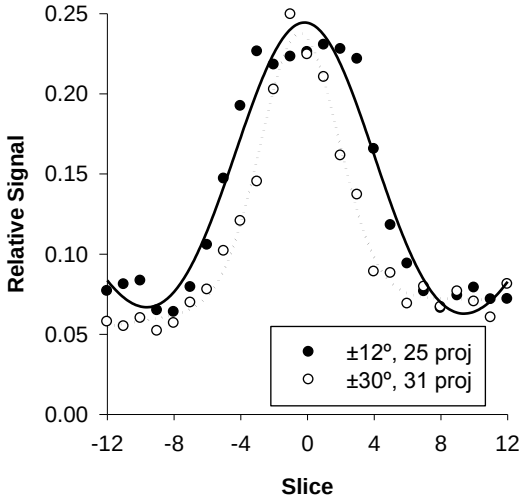

Figure 7.10 Vertical profile of the microcalcification signal for two different reconstructions. The better vertical resolution in the projection set with wider angular range is reflected in the narrower Gaussian fit, yielding a lower FWHM.

Table 7.1 Quantitative results of the acquisition geometry optimization study.

Rank	Angular Range	Number of Projections	CNR	AVW	Normalized CNR	Normalized AVW	Quality Factor
1	±24	17	1.342	5.555	0.993	0.906	0.900
2	±30	21	1.278	5.555	0.946	0.906	0.857
3	±30	31	1.132	5.033	0.838	1.000	0.838
4	±30	61	1.127	5.037	0.834	0.999	0.834
5	±20	9	1.191	5.430	0.882	0.927	0.817
6	±24	25	1.184	5.866	0.877	0.858	0.753
7	±20	21	1.214	6.318	0.899	0.797	0.716
8	±24	49	1.084	5.741	0.803	0.877	0.704
9	±20	41	1.170	6.408	0.867	0.785	0.681
10	±16	9	1.292	8.072	0.957	0.623	0.597
11	±16	17	1.177	7.518	0.871	0.669	0.583
12	±20	11	1.134	7.822	0.839	0.643	0.540
13	±12	13	1.350	9.479	1.000	0.531	0.531
14	±16	33	1.134	8.064	0.839	0.624	0.524
15	±12	25	1.175	9.442	0.870	0.533	0.464
16	±12	9	1.213	10.306	0.898	0.488	0.439
17	±8	17	1.218	15.074	0.902	0.334	0.301
18	±8	9	1.276	16.489	0.945	0.305	0.289

Figure 7.10 shows the Gaussian fit for two different reconstructions. The variation in vertical resolution with wider angular range is clear, yielding a lower AVW, which represents increased vertical resolution.

Table 7.1 shows the results of the quantitative analysis performed in the 18 reconstructions remaining after the qualitative elimination process, sorted by QF. The two reconstructions with the highest QF are shown in Figure 7.11.

Discussion

The visibility of all the inserted lesions except the bottom spiculation in Figure 7.8(c)-(f) shows the effectiveness of tomosynthesis imaging, compared to the lack of visibility of the soft tissue lesions in the projection image shown in Figure 7.7(b). This is

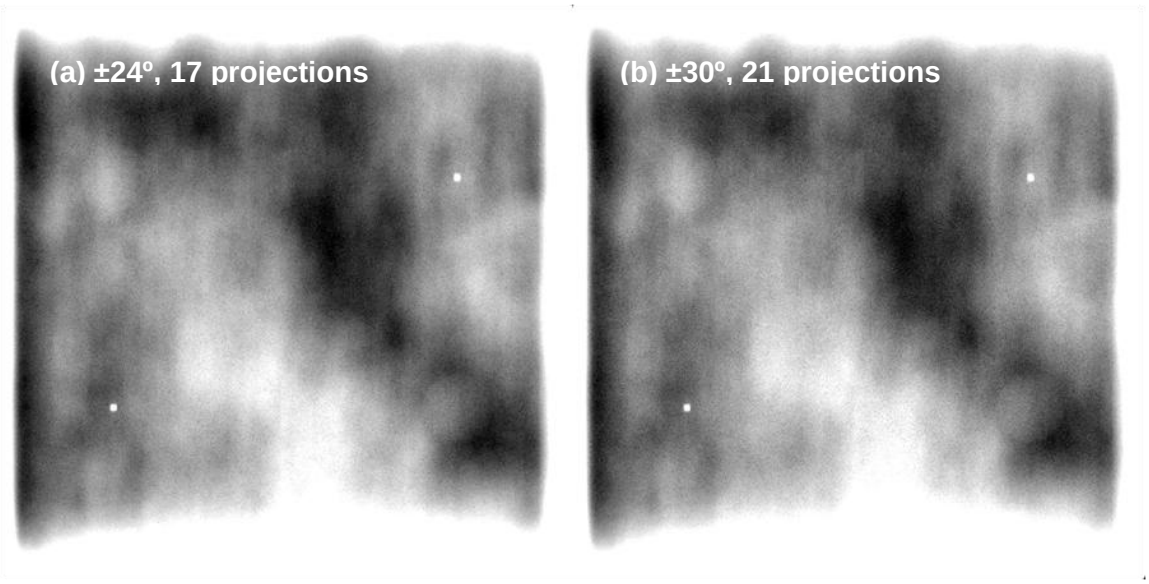

Figure 7.11 Central slice of the two reconstructions with the highest QF.

especially true if the tomosynthesis reconstruction images are compared to Figure 7.7(a), which include neither x-ray scatter nor system resolution and noise characteristics.

Of the 38 projection sets studied, only 18 yielded reconstructions which presented enough vertical resolution to be analyzed quantitatively. This was expected due to the inclusion of extreme cases where very few projections were acquired per set or where the angular range covered was very narrow. Of these 18 projection sets, the expected trend of increased vertical resolution with increased angular range was observed. In terms of the number of projections per set, it appears that past a certain threshold in number of projections included in the set, the increase in vertical resolution diminishes. The in-plane visibility, measured in this study by the CNR, shows a clear inverse proportionality with the number of projections included in the set. This trend is expected given the necessity to decrease the exposure used per projection to maintain the dose to the breast constant. The effect of “diminishing returns” found in the vertical resolution, coupled with the clear trend of decreasing in-plane visibility with increasing

number of projections leads to the conclusion that there is an optimum balance between number of projections and reconstruction quality. This balance seems to be achieved when the number of projections is approximately between 15 and 30, depending on the angular range, with the three best reconstructions found to be the ones that cover an angular range of ±24º and ±30º and have a projection angle step of 2º to 3º, yielding 17 to 31 projections per set. It must be noted that the projection set that was found to result in the second highest QF is the one used in one of the prototype breast tomosynthesis imaging systems (Eberhard et al 2006).

The use of the power law distribution for the modeling of breast tissue without any phase information limits the quality of the simulation of anatomic noise. This limitation, however, is minimized by the fact that the optimization is conducted by comparing the relative quality of the reconstructions using the same breast tissue for all the projection sets, and not by comparing the absolute quality against other models. Therefore, the need of generating accurate models of the normal breast tissue is somewhat relaxed. Other assumptions made in this study are the uniformity of the x-ray field incident on the breast, which ignores the heel effect, and the uniformity of the detector response within each projection, which disregards the variation in resolution due to the difference in incidence angle of the x-rays at different points in the detector. These effects were minimized by performing the study using a small breast volume, therefore using only a small area of the x-ray field and detector, minimizing the mentioned variations.

Conclusion

A simulation of a tomosynthesis imaging system with multi-threading capabilities was implemented. The simulation is capable of using different acquisition geometries

and incorporates the resolution and noise limitations present in a clinical mammography system, as described by the mathematical model derived in the previous chapter. In addition, the simulation accepts as input the glandular dose to be delivered to the imaged breast, which, using the results from Chapter 2, sets the exposure available per projection acquisition, resulting in the appropriate amount of noise being added to the images. Furthermore, the simulation computes the expected x-ray scatter present in the tomosynthesis projections from the results found in Chapter 5 is computed and incorporated to the simulated images.

A reconstruction program based on a modified version of the MLEM reconstruction method was also implemented. The modification to the MLEM algorithm involved taking the presence of x-ray scatter in the projection images into account. This is especially important in tomosynthesis imaging, given the challenges involved in using a traditional anti-scatter grid.

These two implementations, coupled with a methodology to analyze tomosynthesis reconstructions, were used to investigate the effect of angular range and number of projections on the quality of tomosynthesis reconstructions. As expected, it was found that a minimum number of projections and a minimum angular range must be used to successfully perform tomosynthesis imaging. In addition, it was found that beyond a certain threshold, an increase in the number of projections used per set does not increase the vertical resolution substantially and decreases the quality of the in-plane visibility, resulting in a decrease in the overall quality of the reconstruction.

CHAPTER 8

CONCLUSIONS

The objective of this work was to develop, implement and utilize a computational framework to study and address major pending issues in digital tomosynthesis imaging of the breast so as to accelerate its introduction into routine clinical use. To achieve this, advanced computer platforms were designed and implemented taking advantage of established theoretical methods like Monte Carlo simulations and serial cascaded modeling, among others. The issues studied with these tools included the radiation dose involved in tomosynthesis imaging, the presence of scattered x-rays in the projection images, the imaging system's performance under tomosynthesis conditions, and the impact of acquisition geometry in image quality.

From the dosimetric Monte Carlo simulations, it was found that it is possible to maintain exposure levels similar to those presently used in planar mammography for a complete tomosynthesis projection set without resulting in an increase in glandular dose to the breast. Furthermore, it was found that in some cases the same exposure level in tomosynthesis results in a lower glandular dose than that in planar mammography. The equations and coefficients found in this section can be used to obtain accurate estimates of the glandular dose during tomosynthesis imaging covering a wide range of conditions.

More sophisticated geometrical simulations were used in conjunction with Monte Carlo methods to compute the dose to most of the radiosensitive organs in the body from all three breast imaging methods in clinical use or in the investigational stage. The results from these studies not only serve the purpose of computing the effective dose from breast imaging, but give epidemiologists and other scientists the tools necessary to perform advanced studies in the consequences of radiation dose and its effect on the

prevalence of different diseases. Of more direct consequence, concrete evidence was found on the relative safety of the use of radiographic breast imaging techniques in patients who present early pregnancies.

Using a modified version of the Monte Carlo platform used for the breast dosimetry studies, a comprehensive understanding of the scattered x-ray behavior in tomosynthesis imaging conditions was obtained. The variation or lack thereof of the x-ray scatter content in the projection images with projection angle, breast composition and size, and x-ray spectrum was characterized. The discovery of the importance of the presence of the breast support plate and detector cover plate in the content of x-ray scatter in the projection images is applicable to all forms of radiographic breast imaging, not only tomosynthesis. The scatter PSF and SPR map characterization, as well as the equations for SPR at the center of mass of the breast projection can be used to either correct for this effect in projection space or to incorporate this effect into the reconstruction algorithm. The latter option was used in this work, using the SPR at the center of mass information in the implementation of the iterative MLEM reconstruction algorithm used later.

The dosimetry studies, in terms of glandular dose to the imaged breast, dose distribution in the other tissues, and resultant whole body dose characterize the limiting factors around which all other design decisions must be addressed. The resulting glandular dose from tomosynthesis projections imposes the exposure conditions that can be used during projection acquisition. These conditions, along with the imaging task, determine the detector specifications required. How these conditions affect the detector performance was studied using a mathematical model derived and implemented using a well established analytical methodology. The resultant signal and noise transfer characteristics of the modeled imaging system were also used to implement a simulation of a complete tomosynthesis imaging system which was used to study the effect that

acquisition geometry has on the final reconstruction quality. This study not only confirmed the benefit of a wider angular range for an enhanced vertical resolution, but also gave insight into the variation of the reconstruction quality with varying number of projections per set, pointing to the conditions necessary for the design of an acquisition geometry that maximizes reconstruction quality.

The simulation of a complete tomosynthesis system, which includes all the relevant stages beginning with the creation of the simulated three dimensional volume to be imaged, may be used in the future for other studies, including the impact of improved detector technologies or image processing techniques. The ability to simulate all stages of a tomosynthesis imaging system allows for extensive developmental work to be performed without the limitation of having to minimize the number of parameters and parameter values to be studied, which is the case when the studies are performed using patients and physical systems.

APPENDIX A

DESIGN OF MONTE CARLO PROGRAMS

General Algorithm

The Geant4 toolkit provides the libraries of functions necessary to define the geometrical description in the simulation, the properties of the particle generator, and the physical processes relevant to the conditions being simulated. Using these libraries, C++ programs were implemented to perform the simulations described in the previous chapters. Although the C++ programs were implemented to perform different simulations, they all follow the same general algorithm, diagramed in Figure A.1. The generator functions are used to simulate the emission of x-rays, which, following the appropriate physical models, travel through the defined geometry, interacting with both regular volumes and volumes that were defined to be active detectors. These detectors tally information according to their implemented properties, and integrate these

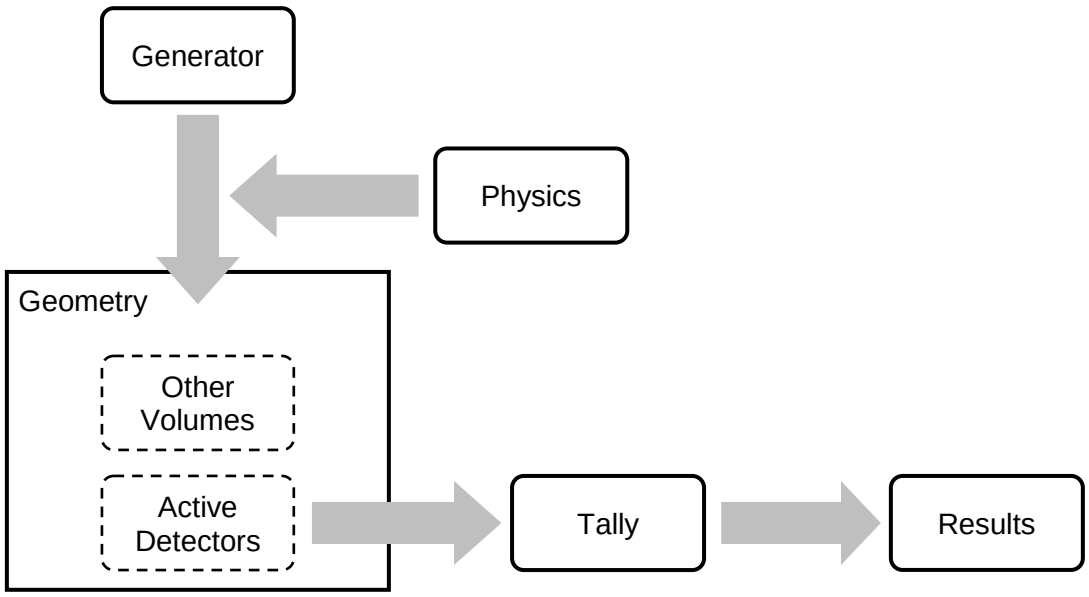

Figure A.1 Diagram of the basic flow of the Monte Carlo programs.

measurements over the length of the run, defined by the number of x-rays to be simulated. After the last x-ray has been tracked, the tallies are processed, yielding the final simulation results.

Implementation Details

Generator

The Geant4 generator, denoted the primary generator, is capable of emitting many different types of particles with a wide variety of properties. In these implementations, the primary generator is used to emit x-rays of constant energy, which is varied with every run. The results from the different runs are combined to obtain spectral results, as described earlier. The primary generator requires the specification of the initial position of the emitted particle, and its initial momentum direction. The initial position of the x-rays was defined as the position of the x-ray focal spot, according to the source-to-imager distance, the projection angle, etc. The initial momentum direction was implemented as the result of two random number generations, one for the x direction and the other for the y direction, constrained in their magnitude so that the x-ray, if unencumbered, reached the top surface of the detector. The random number generators (RNG) used yield pseudo-random floating point numbers ranging from 0.0 to 1.0 according to user-selectable distributions. For the simulations where the x-ray field was uniform over the detector, a RNG that follows a uniform probability distribution was used. Where the simulations included the effects of the heel effect, a RNG which allows for the description of the probability distribution was used. The variations in relative magnitude of the x-ray fluence over the detector due to the heel effect were used as input to describe the probability distribution function of the RNG. For the x-coordinate of the initial momentum direction the random number generated from 0.0 to 1.0 was scaled by

the size of the detector in this direction. For the y-coordinate, 0.5 was subtracted from the random number to yield a value from -0.5 to 0.5 and this number was scaled by the relative size of the detector. This relative size is defined as the width of the perpendicular projection of the detector presented to the x-ray source, given that the surface of the detector is not normal to the central ray when the projection angle is non-zero. This guarantees that the x-ray's initial momentum direction will be towards the top surface of the detector.

Physics

The Geant4 toolkit includes a vast range of physics models, and it is the programmer's responsibility to define the ones that are appropriate for each simulation. For all the simulations implemented in this work the physics models used were:

- Photons:
    - Photoelectric effect (Low Energy Library)
    - Compton scattering (Low Energy Library)
    - Rayleigh scattering (Low Energy Library)
- Electrons:
    - Bremsstrahlung (Low Energy Library)
    - Ionization (Low Energy Library)
    - Multiple Scattering (Standard Library)
- Positrons:
    - Bremsstrahlung (Standard Library)
    - Ionization (Standard Library)
    - Multiple Scattering (Standard Library)
    - Annihilation (Standard Library)

The physics models of the Low Energy Library, although slower than the Standard Library, are specifically implemented for use in the energy ranges used in this work, and therefore were used when available. Although positrons were not relevant to these simulations, their inclusion was necessary due to a requirement of the Geant4 implementation when electrons are defined.

The Auger electrons and fluorescent photons options of the photoelectric effect and the electron ionization models was activated, with a threshold energy for production of these secondaries of 5 keV. If the simulation required the production of one of these secondaries with energy below this threshold the particle was assumed to be absorbed locally and was not created. This setting allows for an important reduction in processing time avoiding the creation of particles with extremely short range, which can be approximated to be negligible.

Geometry

Although the geometries implemented in the different Monte Carlo simulations vary, the general algorithm behind the implementation is similar. All the volumes included in the simulation consisted of one or more geometrical shapes (boxes, spheres, ellipsoids, etc.) defined using the functions provided by Geant4 for geometry description. In the cases where more than one shape was needed to define a volume (e.g. the compressed breast in MLO or the gall bladder) these shapes were fused together using Geant4's Boolean functions.

In the description of the compressed breast, all the parameters needed to define the volumes representing the breast tissue, breast skin, and pectoralis muscle where defined using variables, whose value varied according to the inputted chest wall to nipple distance and breast thickness. In this way the breast could be defined using these

two parameters, and all the relevant volumes were re-defined automatically to conform to the new dimensions.

This same algorithm was used for the organs of the human body implemented for the whole body dosimetry studies. All the dimensions of the volumes representing the various tissues were based on variables, which allow for the variation of the size of the organs according to the age of the phantom, as inputted by the user. Although in this work only the “15-AF” female phantom was used, the implementation allows for the use of anthropomorphic phantoms of six ages ranging from newborn to adult.

The chemical composition of each volume defined in the simulation must be specified. In these simulations, the library of elements defined by the NIST that is provided in Geant4, which includes the naturally occurring relative abundance of the isotopes of each element, was used. To be able to define the breast tissue as composed of a homogeneous mixture of adipose and glandular tissue for any value of glandular fraction, the weight fractions of the different elements that compose adipose and glandular tissue were fitted to linear equations, and the resulting slopes and offsets were used to obtain the correct weight fraction of each element to represent the homogeneous mixture.

The actual measurement of what is required of the Monte Carlo simulation is performed by defining any of the volumes present in the geometry as an active detector. Which of the volumes is defined as an active detector depends on what the simulation is measuring. For example, for the breast dosimetry studies, the breast tissue was defined as an active detector. For the x-ray scatter studies, the box volume representing the imager was defined as the active detector. For the whole body dosimetry studies, all the volumes representing tissues in the body were defined as separate active detectors. What the active detectors measure was custom defined, the libraries provided by Geant4 for this task were not used. During the simulation, when a particle interacts

inside a volume defined as an active detector, the function related to this detector is called. This function defines what is measured and where this information is stored. In the case of the breast dosimetry studies, the energy deposited by the interaction was multiplied by the G factor, as defined by Boone (Boone 1999), using fitted values for the mass-energy absorption coefficients for adipose and glandular tissues for the energy of the incident photon. If the energy deposition was due to an ionization event from an electron, the energy of the photon that produced that electron was used as input for the computation of the G factor. The result of this product was then added to the tally that persists throughout the simulation to produce the final total glandular dose. A similar algorithm was used for the volumes representing bones in the whole body dosimetry studies, although instead of the G factor, the deposited energy was multiplied by the appropriate coefficient given by the three-factor mass–energy absorption coefficient method, as described previously. For the other tissues where the radiation dose was sought, the energy deposited by each interaction was directly added to the tally that persisted throughout the simulation.

In the Monte Carlo simulations that characterized the x-ray scatter present in the tomosynthesis projections, the simulated imager, which was the only volume defined as an active detector had to be implemented so as to discriminate between primary (non-scattered) x-rays and scattered x-rays. Since Geant4 does not flag any particle as having undergone previous interactions, two tests were implemented in the detection algorithm to perform this discrimination. In the first place, the “ParentID” of the photon is tested to be zero, which means that the photon was emitted by the primary generator, and, if this test is passed, the momentum direction upon entering the imager volume is compared to the original momentum direction the photon had when emitted. If these momentum directions are equal, then the photon is determined to be a primary photon. The pixel to which to assign the energy of the incident photon is determined by dividing

the distance from the detector edges by the desired horizontal and vertical resolutions. In these simulations the tallied results consisted of two arrays, one representing the primary image, and one representing the scatter image.

Results

At the end of a simulation, the tallies containing the measured results are processed depending on the requirements of the simulation and the results saved to text files. For the dosimetry studies, the tallies consisting of the total energy deposited in each volume are divided by the corresponding volume mass to obtain the dose deposited in each volume. To obtain the normalized glandular dose values in the breast dosimetry studies, the computed doses are divided by the exposure at the reference point computed using the definition of the Roentgen, and the results saved to disk. For the x-ray scatter studies, the tallies representing the primary and scatter images are saved directly, with no further processing.

REFERENCES

Agostinelli, S., Allison, J., Amako, K., et al. (2003). Geant4 - A simulation toolkit. *Nuclear Instruments and Methods in Physics Research Section A: Accelerators, Spectrometers, Detectors and Associated Equipment* **506**(3): 250-303.

Allison, J., Amako, K., Apostolakis, J., et al. (2006). Geant4 Developments and Applications. *IEEE Transactions on Nuclear Science* **53**(1): 270-278.

American Cancer Society (2007). Cancer Facts & Figures 2007. Atlanta, GA, American Cancer Society.

Barnes, G. T. and Brezovich, I. A. (1978). The intensity of scattered radiation in mammography. *Radiology* **126**(1): 243-247.

Barrett, H. H. and Swindell, W. (1981). Radiological imaging: The theory of image formation, detection, and processing. New York, Academic Press.

Baydush, A. H. and Floyd, C. E., Jr. (2000). Improved image quality in digital mammography with image processing. *Medical Physics* **27**(7): 1503-1508.

Berger, M. J., Hubbell, J. H., Seltzer, S. M., et al. (2005). XCOM: Photon Cross Sections Database. NIST Standard Reference Database 8 (XGAM)

Bissonnette, J. P., Cunningham, I. A., Jaffray, D. A., Fenster, A. and Munro, P. (1997). A quantum accounting and detective quantum efficiency analysis for video-based portal imaging. *Medical Physics* **24**(6): 815-826.

Blume, H., Colditz, J., Eckenbach, W., et al. (1995). Image intensifier and X-ray Exposure Control Systems. *RSNA categorical course in Physics*: 87-103.

Boone, J. M. (1999). Glandular breast dose for monoenergetic and high-energy X-ray beams: Monte Carlo assessment. *Radiology* **213**(1): 23-37.

Boone, J. M. (2002). Normalized glandular dose (DgN) coefficients for arbitrary X-ray spectra in mammography: Computer-fit values of Monte Carlo derived data. *Medical Physics* **29**(5): 869-875.

Boone, J. M. (2004). Breast CT: Its prospect for breast cancer screening and diagnosis. Advances in breast imaging: Physics, Technology and Clinical Applications, Categorical course in diagnostic radiology physics. Karellas, A. and Giger, M. L. Oak Brook, IL, Radiological Society of North America (RSNA).

Boone, J. M. and Cooper, V. N., 3rd (2000a). Scatter/primary in mammography: Monte Carlo validation. *Medical Physics* **27**(8): 1818-1831.

Boone, J. M., Fewell, T. R. and Jennings, R. J. (1997). Molybdenum, rhodium, and tungsten anode spectral models using interpolating polynomials with application to mammography. *Medical Physics* **24**(12): 1863-1874.

Boone, J. M., Kwan, A. L. C., Seibert, J. A., et al. (2005). Technique factors and their relationship to radiation dose in pendant geometry breast CT. *Medical Physics* **32**(12): 3767-3776.

Boone, J. M., Kwan, A. L. C., Yang, K., et al. (2006). Computed Tomography for Imaging the Breast. *Journal of Mammary Gland Biology and Neoplasia*: 103-111.

Boone, J. M., Lindfors, K. K., Cooper, V. N., 3rd and Seibert, J. A. (2000b). Scatter/primary in mammography: Comprehensive results. *Medical Physics* **27**(10): 2408-2416.

Boone, J. M., Nelson, T. R., Lindfors, K. K. and Seibert, J. A. (2001). Dedicated breast CT: Radiation dose and image quality evaluation. *Radiology* **221**(3): 657-667.

Boone, J. M., Shah, N. and Nelson, T. R. (2004). A comprehensive analysis of DgN(CT) coefficients for pendant-geometry cone-beam breast computed tomography. *Medical Physics* **31**(2): 226-235.

Browne, J. A. and Holmes, T. J. (1992). Developments with maximum likelihood X-ray computed tomography. *IEEE Transactions on Medical Imaging* **11**(1): 40-52.

Burgess, A. E., Jacobson, F. L. and Judy, P. F. (2001). Human observer detection experiments with mammograms and power-law noise. *Medical Physics* **28**(4): 419-437.

Castellano, I. A., Dance, D. R. and Evans, P. M. (2005). CT dosimetry: getting the best from the adult Cristy phantom. *Radiation Protection Dosimetry* **114**(1-3): 321-325.

Chen, B. and Ning, R. (2002). Cone-beam volume CT breast imaging: feasibility study. *Medical Physics* **29**(5): 755-770.

Chen, S. C., Carton, A. K., Albert, M., et al. (2007). Initial Clinical Experience With Contrast-Enhanced Digital Breast Tomosynthesis. *Academic Radiology* **14**(2): 229-238.

Chen, Z. and Ning, R. (2003). Why should breast tumour detection go three dimensional? *Physics in Medicine and Biology* **48**(14): 2217-2228.

Cooper, V. N., 3rd, Boone, J. M., Seibert, J. A. and Pellot-Barakat, C. J. (2000). An edge spread technique for measurement of the scatter-to-primary ratio in mammography. *Medical Physics* **27**(5): 845-853.

Cranley, K., Gilmore, B. J., Fogarty, G. W. A. and Desponds, L. (1997). Catalogue of diagnostic x-ray spectra and other data, Institute of Physics and Engineering in Medicine.

Cristy, M. (1980). Mathematical phantoms representing children of various ages for use in estimates of internal dose. ORNL/NUREG/TM-367. Oak Ridge, Tennessee, Oak Ridge National Laboratory.

Cristy, M. and Eckerman, K. (1987). Specific absorbed fractions of energy at various ages from internal photon sources. I. Methods. Report ORNL/TM-8381/V1. Oak Ridge, TN, Oak Ridge National Laboratory.

Cunningham, I. A. (1998). Linear-systems modeling of parallel cascaded stochastic processes: the NPS of radiographic screens with reabsorption of characteristic x-radiation. *Proceedings of SPIE* **3336**: 220-230.

Cunningham, I. A. (2000). Applied linear-systems theory. Handbook of medical imaging. Beutel, J., Kundel, H. L. and Van Metter, R. Bellingham, Wash., SPIE Press. 1. Physics and psychophysics**:** 79-160.

Cunningham, I. A., Moschandreou, T. and Subotic, V. (2001). Detective quantum efficiency of fluoroscopic systems: the case for a spatial-temporal approach (or, does the ideal observer have infinite patience?). *Proceedings of SPIE* **4320**: 479-488.

Cunningham, I. A., Westmore, M. S. and Fenster, A. (1994). A spatial-frequency dependent quantum accounting diagram and detective quantum efficiency model

of signal and noise propagation in cascaded imaging systems. *Medical Physics* **21**(3): 417-427.

Cunningham, I. A., Yao, J. and Subotic, V. (2002). Cascaded models and the DQE of flat-panel imagers: noise aliasing, secondary quantum noise, and reabsorption. *Proceedings of SPIE* **4682**: 61-72.

Dainty, J. C. and Shaw, R. (1974). Image science : principles, analysis and evaluation of photographic-type imaging processes. London ; New York, Academic Press.

Dance, D. R. (1980). The Monte Carlo calculation of integral radiation dose in xeromammography. *Physics in Medicine and Biology* **25**(1): 25-37.

Dance, D. R. (1990). Monte Carlo calculation of conversion factors for the estimation of mean glandular breast dose. *Physics in Medicine and Biology* **35**(9): 1211-1219.

Dance, D. R. and Day, G. J. (1984). The computation of scatter in mammography by Monte Carlo methods. *Physics in Medicine and Biology* **29**(3): 237-247.

Darambara, D. G., Taibi, A. and Speller, R. D. (2002). Image-quality performance of an a-Si:H-based X-ray imaging system for digital mammography. *Nuclear Instruments and Methods in Physics Research Section A: Accelerators, Spectrometers, Detectors and Associated Equipment* **477**: 521-526.

Dobbins, J. T., 3rd and Godfrey, D. J. (2003). Digital x-ray tomosynthesis: current state of the art and clinical potential. *Physics in Medicine and Biology* **48**(19): R65-R106.

Doi, K. and Chan, H. P. (1980). Evaluation of absorbed dose in mammography: monte carlo simulation studies. *Radiology* **135**(1): 199-208.

Eberhard, J. W., Staudinger, P., Smolenski, J., et al. (2006). High-speed large-angle mammography tomosynthesis system. *Proceedings of SPIE* **6142**: 61420C-61411.

Elmore, J. G., Barton, M. B., Moceri, V. M., et al. (1998). Ten-year risk of false positive screening mammograms and clinical breast examinations. *New England Journal of Medicine* **338**(16): 1089-1096.

Fandos-Morera, A., Prats-Esteve, M., Tura-Soteras, J. M. and Traveria-Cros, A. (1988). Breast tumors: composition of microcalcifications. *Radiology* **169**(2): 325-327.

Fritz, S. L., Chang, C. H. and Livingston, W. H. (1983). Scatter/primary ratios for x-ray spectra modified to enhance iodine contrast in screen-film mammography. *Medical Physics* **10**(6): 866-870.

Ganguly, A., Rudin, S., Bednarek, D. R. and Hoffmann, K. R. (2003). Micro-angiography for neuro-vascular imaging. II. Cascade model analysis. *Medical Physics* **30**(11): 3029-3039.

Glick, S. J., Thacker, S., Gong, X. and Liu, B. (2007). Evaluating the impact of X-ray spectral shape on image quality in flat-panel CT breast imaging. *Medical Physics* **34**(1): 5-24.

Glick, S. J., Vedantham, S. and Karellas, A. (2002). Investigation of optimal kVp settings for CT Mammography using a Flat-panel Imager. *Proceedings of SPIE* **4682**: 392-402.

Gong, X., Glick, S. J., Liu, B., Vedula, A. A. and Thacker, S. (2006). A computer simulation study comparing lesion detection accuracy with digital mammography, breast tomosynthesis, and cone-beam CT breast imaging. *Medical Physics* **33**(4): 1041-1052.

Gong, X., Vedula, A. A. and Glick, S. J. (2004). Microcalcification detection using cone-beam CT mammography with a flat-panel imager. *Physics in Medicine and Biology* **49**(11): 2183-2195.

Gonzalez, R. C. and Woods, R. E. (2002). Digital image processing. Upper Saddle River, N.J., Prentice Hall.

Gonzalez Trotter, D. E., Tkaczyk, J. E., Kaufhold, J., Claus, B. E. H. and Eberhard, J. W. (2002). Thickness-dependent scatter correction algorithm for digital mammography. *Proceedings of SPIE* **4682**: 469-478.

Grabski, V., Brandan, M. E., Ruiz-Trejo, C. and Villasenor, Y. (2005). SU-FF-I-34: PSF and S/P in Mammography: A Validation of Simulations Using the GEANT4 Code. *Medical Physics* **32**(6): 1911.

Gray, H. and Goss, C. M. (1973). Anatomy of the human body. Philadelphia, PA, Lea & Febiger.

Hammersley, J. M. and Handscomb, D. C. (1964). Monte Carlo methods. London, New York, Methuen; Wiley.

Hammerstein, G. R., Miller, D. W., White, D. R., et al. (1979). Absorbed radiation dose in mammography. *Radiology* **130**(2): 485-491.

Hatziioannou, K. A., Psarrakos, K., Molyvda-Athanasopoulou, E., et al. (2000). Dosimetric considerations in mammography. *European Radiology* **10**(7): 1193-1196.

Hebert, T. and Leahy, R. (1989). A generalized EM algorithm for 3-D Bayesian reconstruction from Poisson data using Gibbs priors. *IEEE Transactions on Medical Imaging* **8**(2): 194-202.

Hendrick, R. E., Bassett, L., Botsco, M. A., et al. (1999). Mammography Quality Control Manual. Reston, VA, American College of Radiology.

Huang, S., Yang, K., Kwan, A. and Boone, J. (2006). TH-E-330A-01: Computational Evaluation of Breast Geometry From Breast CT. *Medical Physics* **33**(6): 2287-2287.

Huda, W., Scalzetti, E. M. and Roskopf, M. (2000). Effective doses to patients undergoing thoracic computed tomography examinations. *Medical Physics* **27**(5): 838-844.

Humphrey, L. L., Helfand, M., Chan, B. K. and Woolf, S. H. (2002). Breast cancer screening: a summary of the evidence for the U.S. Preventive Services Task Force. *Annals of Internal Medicine* **137**(5 Part 1): 347-360.

International Commission on Radiation Units and Measurements (1989). ICRU Report 44: Tissue substitutes in radiation dosimetry and measurement. Bethesda, MD, International Commission on Radiation Units and Measurements.

International Commission on Radiation Units and Measurements (1992). ICRU Report 46: Photon, electron, proton, and neutron interaction data for body tissues. Bethesda, MD, International Comission on Radiation Units and Measurements.

International Commission on Radiological Protection (1982). ICRP Publication 34: Protection of the patient in diagnostic radiology: A report of Committee 3 of the International Commission on Radiological Protection. Oxford; New York, Published for The Commission by Pergamon Press.

International Commission on Radiological Protection (1991). ICRP Publication 60: 1990 recommendations of the International Commission on Radiological Protection.

Oxford; New York, Published for the International Commission on Radiological Protection by Pergamon Press.

International Commission on Radiological Protection (2002). ICRP Publication 89: Basic anatomical and physiological data for use in radiological protection: Reference values. Oxford; New York, Published for the International Commission on Radiological Protection by Pergamon Press.

International Commission on Radiological Protection (2007). Draft Recommendations of the International Commission on Radiological Protection. http://www.icrp.org/docs/ICRP_Draft_Recommendations_12_January_2007.pdf.Accessed February 2, 2007.

Jamal, N., Ng, K. H. and Mclean, D. (2003). A study of mean glandular dose during diagnostic mammography in Malaysia and some of the factors affecting it. *British Journal of Radiology* **76**(904): 238-245.

Jee, K.-W., Antonuk, L. E., El-Mohri, Y. and Zhao, Q. (2003). System performance of a prototype flat-panel imager operated under mammographic conditions. *Medical Physics* **30**(7): 1874-1890.

Johns, H. E. and Cunningham, J. R. (1983). The Physics of Radiology. Springfield, Ill., U.S.A., Charles C. Thomas.

Joseph, T. R. and Michael, J. D. (2006). A comparison of reconstruction algorithms for C-arm mammography tomosynthesis. *Medical Physics* **33**(8): 3018-3032.

Karellas, A. (2006). Digital Mammography Image Acquisition Technology. Radiological Society of North America scientific assembly and annual meeting program. Oak Brook, Ill, Radiological Society of North America**:** 148.

Kaufhold, J., Thomas, J. A., Eberhard, J. W., Galbo, C. E. and Trotter, D. E. G. (2002). A calibration approach to glandular tissue composition estimation in digital mammography. *Medical Physics* **29**(8): 1867-1880.

Kerlikowske, K., Grady, D., Barclay, J., Sickles, E. A. and Ernster, V. (1996). Effect of age, breast density, and family history on the sensitivity of first screening mammography. *JAMA* **276**(1): 33-38.

King, S. D. and Spiers, F. W. (1985). Photoelectron enhancement of the absorbed dose from X rays to human bone marrow: experimental and theoretical studies. *British Journal of Radiology* **58**(688): 345-356.

Klein, D. J., Chan, H. P., Muntz, E. P., et al. (1983). Experimental and theoretical energy and angular dependencies of scattered radiation in the mammography energy range. *Medical Physics* **10**(5): 664-668.

Kolb, T. M., Lichy, J. and Newhouse, J. H. (1998). Occult cancer in women with dense breasts: detection with screening US--diagnostic yield and tumor characteristics. *Radiology* **207**(1): 191-199.

Kolb, T. M., Lichy, J. and Newhouse, J. H. (2002). Comparison of the performance of screening mammography, physical examination, and breast US and evaluation of factors that influence them: an analysis of 27,825 patient evaluations. *Radiology* **225**(1): 165-175.

Kolitsi, Z., Panayiotakis, G., Anastassopoulos, V., Scodras, A. and Pallikarakis, N. (1992). A multiple projection method for digital tomosynthesis. *Medical Physics* **19**(4): 1045-1050.

Kopans, D. B. (2002). Beyond randomized controlled trials: organized mammographic screening substantially reduces breast carcinoma mortality. *Cancer* **94**(2): 580-581; author reply 581-583.

Kramer, R. and Drexler, G. (1982). On the Calculation of the Effective Dose Equivalent. *Radiation Protection Dosimetry* **3**(1-2): 13-24.

Kramer, R., Khoury, H. J., Vieira, J. W., et al. (2004). All about FAX: a Female Adult voXel phantom for Monte Carlo calculation in radiation protection dosimetry. *Physics in Medicine and Biology* **49**(23): 5203-5216.

Kramer, R., Vieira, J. W., Khoury, H. J., Lima, F. R. A. and Fuelle, D. (2003). All about MAX: a male adult voxel phantom for Monte Carlo calculations in radiation protection dosimetry. *Physics in Medicine and Biology* **48**(10): 1239-1262.

Kwan, A. L. C., Boone, J. M. and Shah, N. (2005). Evaluation of x-ray scatter properties in a dedicated cone-beam breast CT scanner. *Medical Physics* **32**(9): 2967-2975.

Lam, K. L. and Chan, H. P. (1990). Effects of x-ray beam equalization on mammographic imaging. *Medical Physics* **17**(2): 242-249.

Lange, K. and Fessler, J. A. (1995). Globally convergent algorithms for maximum a posteriori transmission tomography. *IEEE Transactions on Image Processing* **4**(10): 1430-1438.

Lee, C., Lee, C., Shah, A. P. and Bolch, W. E. (2006). An assessment of bone marrow and bone endosteum dosimetry methods for photon sources. *Physics in Medicine and Biology* **51**(21): 5391-5407.

Levitan, E. and Herman, G. T. (1987). A Maximum a posteriori probability expectation maximization algorithm or image reconstruction in emission tomography. *IEEE Transactions on Medical Imaging* **MI-6**(3): 185-192.

Liu, B., Glick, S. and Gong, X. (2005). TU-EE-A3-05: Scatter Radiation in Digital Tomosynthesis. *Medical Physics* **32**(6): 2105.

Liu, B., Wu, T., Moore, R. H. and Kopans, D. B. (2006). Monte Carlo simulation of x-ray scatter based on patient model from digital breast tomosynthesis. *Proceedings of SPIE* **6142**: 61421N-61429.

Lubinsky, A. R., Zhao, W., Ristic, G. and Rowlands, J. A. (2006). Screen optics effects on detective quantum efficiency in digital radiography: Zero-frequency effects. *Medical Physics* **33**(5): 1499-1509.

Mainprize, J. G., Bloomquist, A. K., Kempston, M. P. and Yaffe, M. J. (2006). Resolution at oblique incidence angles of a flat panel imager for breast tomosynthesis. *Medical Physics* **33**(9): 3159-3164.

Manglos, S. H., Gagne, G. M., Krol, A., Thomas, F. D. and Narayanaswamy, R. (1995). Transmission maximum-likelihood reconstruction with ordered subsets for cone beam CT. *Physics in Medicine and Biology* **40**(7): 1225-1241.

Mckinley, R. L., Samei, E., Brzymialkiewicz, C. N., Tornai, M. P. and Floyd, J. C. E. (2004). Measurements of an optimized beam for x-ray computed mammotomography. *Proceedings of SPIE* **5368**: 311-319.

Mckinley, R. L., Tornai, M. P., Samei, E. and Bradshaw, M. L. (2005). Initial study of quasi-monochromatic X-ray beam performance for X-ray computed mammotomography. *IEEE Transactions on Nuclear Science* **52**(5): 1243-1250.

Mcwilliams, A. and Lam, S. (2005). Lung cancer screening. *Current Opinion in Pulmonary Medicine* **11**(4): 272-277.

Metz, C. E. and Doi, K. (1979). Transfer function analysis of radiographic imaging systems. *Physics in Medicine and Biology* **24**(6): 1079-1106.

Niklason, L. T., Christian, B. T., Niklason, L. E., et al. (1997). Digital tomosynthesis in breast imaging. *Radiology* **205**(2): 399-406.

Ning, R., Conover, D. L., Chen, B., et al. (2002). Flat-panel-detector-based cone-beam volume CT breast imaging: phantom and specimen study. *Proceedings of SPIE* **4682**: 218-227.

Ning, R., Yu, Y., Conover, D. L., et al. (2004). Preliminary system characterization of flat-panel-detector-based cone-beam CT for breast imaging. *Proceedings of SPIE* **5368**: 292-303.

Nykanen, K. and Siltanen, S. (2003). X-ray scattering in full-field digital mammography. *Medical Physics* **30**(7): 1864-1873.

ORNL Center for Biokinetic and Dosimetric Research (2005). Description of the Mathematical Phantom. http://ordose.ornl.gov/resources/phantom.html. Accessed October 10, 2006.

Pan, T.-S., Tsui, B. M. W. and Byrne, C. L. (1997). Choice of initial conditions in the ML reconstruction of fan-beam transmission with truncated projection data. *IEEE Transactions on Medical Imaging* **16**(4): 426-438.

Preston-Martin, S. and Pogoda, J. M. (2003). Estimation of radiographic doses in a case-control study of acute myelogenous leukemia. *Health Physics* **84**(2): 245-259.

Que, W. and Rowlands, J. A. (1995). X-ray imaging using amorphous selenium: Inherent spatial resolution. *Medical Physics* **22**(4): 365-374.

Rabbani, M., Shaw, R. and Van Metter, R. (1987). Detective quantum efficiency of imaging systems with amplifying and scattering mechanisms. *Journal of the Optical Society of America A. Optics and Image Science* **4**(5): 895-901.

Rabbani, M. and Van Metter, R. (1989). Analysis of signal and noise propagation for several imaging mechanisms. *Journal of the Optical Society of America A. Optics and Image Science* **6**(8): 1156-1164.

Ren, B., Ruth, C., Stein, J., et al. (2005). Design and performance of the prototype full field breast tomosynthesis system with selenium based flat panel detector. *Proceedings of SPIE* **5745**: 550-561.

Rezentes, P. S., De Almeida, A. and Barnes, G. T. (1999). Mammography Grid Performance. *Radiology* **210**(1): 227-232.

Rockmore, A. J. and Macovski, A. (1977). A maximum likelihood approach to transmission image reconstruction from projections. *IEEE Transactions on Nuclear Science* **24**: 1929-1935.

Rosenberg, R. D., Hunt, W. C., Williamson, M. R., et al. (1998). Effects of age, breast density, ethnicity, and estrogen replacement therapy on screening mammographic sensitivity and cancer stage at diagnosis: review of 183,134 screening mammograms in Albuquerque, New Mexico. *Radiology* **209**(2): 511-518.

Rosenberg, R. D., Lando, J. F., Hunt, W. C., et al. (1996). The New Mexico Mammography Project: Screening Mammography Performance in Albuquerque New Mexico, 1991 to 1993. *Cancer* **78**: 1731-1739.

Rosenstein, M. (1976). Handbook of selected organ doses for projections common in diagnostic radiology. Rockville, MD, Food and Drug Administration (FDA) Publication.

Rowlands, J. A. and Yorkston, J. (2000). Flat Panel Detectors for Digital Radiography. Handbook of medical imaging. Volume 1. Physics and Psychophysics. Beutel, J., Kundel, H. L. and Van Metter, R. Bellingham, Wash., SPIE**:** 223-328.

Saunders, R. S., Jr. and Samei, E. (2003). A method for modifying the image quality parameters of digital radiographic images. *Medical Physics* **30**(11): 3006-3017.

Sechopoulos, I., Suryanarayanan, S., Vedantham, S. and Karellas, A. (2005). SU-FF-I-35: Scatter Correction For Digital Tomosynthesis. *Medical Physics* **32**(6): 1911-1912.

Sechopoulos, I., Vedantham, S., Suryanarayanan, S. and Karellas, A. (2006). SU-FF-I-12: Validation of Geant4's Predictions On X-Ray Scatter and Glandular Dose in Pendant-Geometry Cone-Beam Breast CT. *Medical Physics* **33**(6): 1999-1999.

Seibert, J. A. and Boone, J. M. (1988). X-ray scatter removal by deconvolution. *Medical Physics* **15**(4): 567-575.

Shen, S. Z., Bloomquist, A. K., Mawdsley, G. E., Yaffe, M. J. and Elbakri, I. (2006). Effect of scatter and an antiscatter grid on the performance of a slot-scanning digital mammography system. *Medical Physics* **33**(4): 1108-1115.

Shepp, L. A. and Vardi, Y. (1982). Maximum likelihood reconstruction for Emission Tomography. *IEEE Transactions on Medical Imaging* **MI-1**: 113-122.

Siddon, R. L. (1985). Fast calculation of the exact radiological path for a three-dimensional CT array. *Medical Physics* **12**(2): 252-255.

Siewerdsen, J. H. (1998). Signal, Noise, and Detective Quantum Efficiency of a-Si:H Flat-panel Imagers. Ann Arbor, MI., University of Michigan.

Siewerdsen, J. H., Antonuk, L. E., El-Mohri, Y., et al. (1997). Empirical and theoretical investigation of the noise performance of indirect detection, active matrix flat-panel imagers (AMFPIs) for diagnostic radiology. *Medical Physics* **24**(1): 71-89.

Siewerdsen, J. H., Antonuk, L. E., El-Mohri, Y., et al. (1998). Signal, noise power spectrum, and detective quantum efficiency of indirect-detection flat-panel imagers for diagnostic radiology. *Medical Physics* **25**(5): 614-628.

Spekowius, G., Boerner, H., Eckenbach, W., Quadflieg, P. and Laurenssen, G. J. (1995). Simulation of the imaging performance of x-ray image intensifier/TV camera chains. *Proceedings of SPIE* **2432**: 12-23.

Suryanarayanan, S., Karellas, A. and Vedantham, S. (2004). Physical characteristics of a full-field digital mammography system. *Nuclear Instruments and Methods in Physics Research Section A: Accelerators, Spectrometers, Detectors and Associated Equipment* **533**(3): 560-570.

Suryanarayanan, S., Karellas, A., Vedantham, S., et al. (2001). Evaluation of linear and nonlinear tomosynthetic reconstruction methods in digital mammography. *Academic Radiology* **8**(3): 219-224.

Suryanarayanan, S., Karellas, A., Vedantham, S., et al. (2000). Comparison of tomosynthesis methods used with digital mammography. *Academic Radiology* **7**(12): 1085-1097.

Suryanarayanan, S., Karellas, A., Vedantham, S. and Sechopoulos, I. (2006). Theoretical analysis of high-resolution digital mammography. *Physics in Medicine and Biology* **51**(12): 3041-3055.

Tabar, L., Fagerberg, G., Chen, H. H., et al. (1995). Efficacy of breast cancer screening by age. New results from the Swedish Two-County Trial. *Cancer* **75**(10): 2507-2517.

Thacker, S. C. and Glick, S. J. (2004). Normalized glandular dose (DgN) coefficients for flat-panel CT breast imaging. *Physics in Medicine and Biology* **49**(24): 5433-5444.

Tkaczyk, E. J., Le Blanc, J. W., Nevin, R. L., et al. (2001). Modeling the X-ray Energy Characteristics of DQE for Full-Field Digital Mammography. *Proceedings of SPIE* **4320**: 570-581.

Vedantham, S., Karellas, A. and Suryanarayanan, S. (2004a). Solid-state fluoroscopic imager for high-resolution angiography: parallel-cascaded linear systems analysis. *Medical Physics* **31**(5): 1258-1268.

Vedantham, S., Karellas, A., Suryanarayanan, S., et al. (2000). Full breast digital mammography with an amorphous silicon-based flat panel detector: physical characteristics of a clinical prototype. *Medical Physics* **27**(3): 558-567.

Vedantham, S., Karellas, A., Suryanarayanan, S. and Onishi, S. K. (2004b). Solid-state fluoroscopic imager for high-resolution angiography: physical characteristics of an 8 cm x 8 cm experimental prototype. *Medical Physics* **31**(6): 1462-1472.

Wagner, L. K., Lester, R. G. and Saldana, L. R. (1997). Exposure of the pregnant patient to diagnostic radiations: A guide to medical management. Madison, Wis., Medical Physics Pub.

Wilkinson, L. and Heggie, J. C. P. (2001). Glandular Breast Dose: Potential Errors. *Radiology* **213**: 1.

Williams, M. B., Simoni, P. U., Smilowitz, L., et al. (1999). Analysis of the detective quantum efficiency of a developmental detector for digital mammography. *Medical Physics* **26**(11): 2273-2285.

Winer-Muram, H. T., Boone, J. M., Brown, H. L., et al. (2002). Pulmonary embolism in pregnant patients: fetal radiation dose with helical CT. *Radiology* **224**(2): 487-492.

Wu, T. (2002). Three-Dimensional Mammography Reconstruction using Low Dose Projection Images. Department of Physics. Waltham, MA, Brandeis University.

Wu, T., Moore, R. H., Rafferty, E. A. and Kopans, D. B. (2004a). A comparison of reconstruction algorithms for breast tomosynthesis. *Medical Physics* **31**(9): 2636-2647.

Wu, T., Stewart, A., Stanton, M., et al. (2003). Tomographic mammography using a limited number of low-dose cone-beam projection images. *Medical Physics* **30**(3): 365-380.

Wu, T., Zhang, J., Moore, R., et al. (2004b). Digital tomosynthesis mammography using a parallel maximum-likelihood reconstruction method. *Proceedings of SPIE* **5368**: 1-11.

Wu, X., Barnes, G. T. and Tucker, D. M. (1991). Spectral dependence of glandular tissue dose in screen-film mammography. *Radiology* **179**(1): 143-148.

Wu, X., Gingold, E. L., Barnes, G. T. and Tucker, D. M. (1994). Normalized average glandular dose in molybdenum target-rhodium filter and rhodium target-rhodium filter mammography. *Radiology* **193**(1): 83-89.

Yao, J. and Cunningham, I. A. (2001). Parallel cascades: New ways to describe noise transfer in medical imaging systems. *Medical Physics* **28**(10): 2020-2038.

Young, K. C. and Burch, A. (2000). Radiation doses received in the UK Breast Screening Programme in 1997 and 1998. *British Journal of Radiology* **73**(867): 278-287.

Zankl, M. and Wittmann, A. (2001). The adult male voxel model "Golem" segmented from whole-body CT patient data. *Radiation and Environmental Biophysics* **40**(2): 153-162.

Zeng, K., Yu, H., Fajardo, L. L. and Wang, G. (2006). Cone-beam mammo-computed tomography from data along two tilting arcs. *Medical Physics* **33**(10): 3621-3633.

Zhao, W. and Rowlands, J. A. (1997). Digital radiology using active matrix readout of amorphous selenium: Theoretical analysis of detective quantum efficiency. *Medical Physics* **24**(12): 1819-1833.